University of Trento
University of Brescia
University of Padova
University of Trieste
University of Udine
University IUAV of Venezia

Luca Nicolini (Ph.D. Student)

EQUIVALENT VISCOUS DAMPING AND INELASTIC DISPLACEMENT FOR STRENGTHENED AND REINFORCED MASONRY WALLS

Prof. Claudio Modena (Tutor)
Ass. Prof. Francesca da Porto (Co-Tutor)

2012/05

UNIVERSITY OF TRENTO
Engineering of Civil and Mechanical Structural Systems – XXIV Cycle

Davide Bigoni (Ph.D. Head's)

Final Examination 05/04/2012

Board of Examiners
Prof. Riccardo Zandonini (Università degli Studi di Trento)
Prof. Enrico Radi (Università degli Studi di Modena e Reggio Emilia)
Prof. Guido Magenes (Università degli Studi di Pavia)
Prof. Jan-Willem G. van de Kuilen (Technische Universität München)

SUMMARY

The masonry still one of the widespread construction system for low-rise residential buildings even for countries prone to seismic risk. Despite seismic design methods yet in use are force-based, in the last decades was highlighted as the differences in strength between two levels of damage is low, and therefore as the damage is better correlated to the displacement. Also, in recent years, has arose a widespread expectation for being able to control the damage based on the probability of occurrence of an earthquake or being able to base the design on different performance levels ("performance-based design").
In this context, considerable interest is growing regarding the application of these methods to the design of masonry structures. Many questions are still open and need to be studied more in detail. From the experimental results obtained by cyclic shear-compression tests on different types of masonry panels, an analytical model has been developed, that allows to reproduce the in-plane behavior of both the tested types: one is modern reinforced masonry and the other is traditional multi-leaf stone masonry. The developed model has been used to perform a wide number of dynamic analysis with the aim of studying the inelastic characteristics of the described types of masonry. The results of the analysis made it possible to define simple and reliable formulations for the application of displacement-based method to masonry structures. Finally, we studied the dynamic behavior of a large structure, through the finite element analysis, using a damage model that has been shown to be able to reproduce the response obtained from shaking table tests. This phase has the aims of validate the results obtained for stone masonry walls, and giving useful indication for the application of displacement-based method on multi-degree of freedom structures.

Tutor
Prof. Claudio Modena

Co-Tutor
Ass. Prof. Francesca da Porto

Ph.D. Head’s
Prof. Davide Bigoni

SOMMARIO

La muratura rimane uno dei sistemi costruttivi più diffusi per edifici di modesta elevazione anche nei paesi inclini al rischio sismico. Sebbene i metodi di progettazione anti-sismica finora in uso siano basati sulle forze, negli ultimi decenni è stato tuttavia evidenziato come la differenza in termini di forze fra due livelli di danno sia minima e come dunque il danno sia meglio correlato allo spostamento. Inoltre, negli ultimi anni, si è venuta a creare una diffusa aspettativa di poter riuscire a controllare il danno in funzione della probabilità di accadimento di un terremoto; ovvero riuscire a basare la progettazione su diversi livelli prestazionali ("performance-based design").

In questo contesto, sta crescendo un notevole interesse riguardo all'applicazione di tali metodi di progetto alle strutture in muratura. Molte sono le questioni ancora aperte e che necessitano di essere studiate più approfonditamente. A partire dai risultati sperimentali ottenuti da prove cicliche di compressione e taglio su tipologie diverse di pannelli in muratura, è stato sviluppato un modello analitico che permette di riprodurre il comportamento nel piano di entrambe le tipologie testate. Sono stati considerati due sistemi di muratura, uno moderno e armato e l'altro di tipo tradizionale, a più paramenti di pietra.

Il modello sviluppato è stato usato per eseguire analisi dinamiche, considerando diversi suoli, con lo scopo di studiare le caratteristiche inelastiche delle tipologie di muratura descritte. I risultati delle analisi hanno permesso di definire formulazioni semplici ed allo stesso tempo affidabili per l'applicazione del metodo agli spostamenti a strutture in muratura.

Infine è stato studiato il comportamento dinamico di una struttura di grandi dimensioni, attraverso l'analisi agli elementi finiti, utilizzando un modello di danno che ha dimostrato di essere in grado di riprodurre la risposta ottenuta da prove su tavola vibrante. Questa fase ha il duplice obiettivo di validare i risultati ottenuti per la muratura in pietra e fornire utili indicazioni per l'applicazione del metodo agli spostamenti per strutture a più gradi di libertà.

DEDICATION

Ai miei genitori,
Walter e Paola

ACKNOWLEDGEMENTS

First of all, I would like to acknowledge Ass. Prof. Francesca da Porto, who has always supported my activity during these years of studies and without whom this thesis would not have been written, and Prof. Claudio Modena.

Thanks also to Prof. João Miranda Guedes, Faculty of Engineering of Porto University, for being willing to review the draft of the thesis and for his precious suggestions.

Thanks to Ph.D Giovanni Guidi for his valuable help, especially in the phase of numerical analyses, and the generosity with which he gave me many useful hints in the writing of this thesis. Thanks also to Bruno Luís Quelhas da Silva for his fundamental help in the finite element analyses and for being a living example of take-it-easy life style!

I cannot but express my sincere gratitude to all my colleagues of research group for their help throughout all the phases of the research. In particular, my office colleagues Matteo Panizza and Nicola Mazzon, who not only have always supported me during these years, but were always available to help me solve my frequent computer problems!

Thanks also to all my friends, because if it is true that everyone has the friends that he deserves, I am not sure to deserve such a lot…

I would like to acknowledge my family, in particular my parents and my brothers. Finally, a deep thanks to my Silvia for all her love, support and endless patience!

CONTENTS

LIST OF FIGURES

LIST OF TABLES

1 INTRODUCTION

1.1 Background

In Italy, as in the rest of Europe, masonry constructions constitute a great portion of the existing buildings stock. In addition, they represent a non-negligible quota of the new constructions. The success of this building material is related to its good characteristics of durability, thermal and acoustic insulation, fire resistance, sustainability, and the relative simplicity of realization and cost. On the other hand, due to the long history of this structural system, for a long time masonry structures have been built without actual design and verification, but simply by adopting a number of requirements. For countries not prone to seismic risk, masonry may continue to be conceived without the need for effective design and verification. Conversely, in other countries, including Italy and almost all the countries facing the Mediterranean basin, there is a need to assess the safety of structures, including masonry structures, against of seismic action.

Despite the widespread opinion, among non-professionals, that masonry structures are not capable of resisting seismic actions, it is evident that many structures of this kind have survived to earthquakes, very often without suffering serious damage. Experience teaches that masonry structures, when built in compliance with the rules of art, can withstand earthquakes also of a certain intensity. Of course, it is necessary that the safety of buildings is assessed objectively and according to specific structural standards.

Modern regulations are based on the concept of limit states, which allow to connect the structural performance to the probability of occurrence of a seismic event, through design spectra. Each spectrum is obtained starting from the elastic one, scaling it appropriately with the behaviour factor q, which allows to perform simple linear analyses and, at the same time, to take into account, in a simplified way, the capacity of inelastic deformation and energy dissipation of the structure. In fact, the concept of behaviour factor is implicitly linked to that of ductility.

Values of q-factor to be used in linear analysis are provided by the code. In general, these values are conservative, as they have to ensure a sufficient safety margin for different situations (Magenes, 2010). Therefore, it may occur that safety verifications required for buildings designed according to the rules of the art are not satisfied. The reason of inconsistency between calculation and experimental

evidence mainly lies in the linear model of computation that fails to recognize the inelastic properties of the structure.

The limits of elastic analysis, at the ultimate limit state, are highlighted by comparison with the results of non-linear analysis. For this reason, masonry buildings were the firsts for which, at a code level, a simplified non-linear approach has been felt necessary in real applications (Tomaževič, 1978). In the last decades the non-linear modelling has made large advances, especially in the field of finite element method (Calderini & Lagomarsino, 2008; Lourenço et al., 2007). The non-linear models, especially as regards the dynamic analysis, are not yet suitable instruments for the practical application, due to their complexity and the difficulty to extend their validity in general cases (Magenes, 2006; Magenes, 2010).

The basic requirements that are required for a method of calculation and verification in order to be implemented in the code are reliability and relative simplicity. For this reason, design method based on simplified non-linear procedure have been developed. These methods assume deformation as the input parameter, and not as final parameter to be checked at the end of the process, recognizing that damage is directly connected to deformation, rather than to strength. Hence, those methods are called Performance-Based Design, among which we can mention the Capacity Spectrum Method by (Freeman, 1998), N2 Method by (Fajfar, 2000), Yield Point Spectra by (Aschheim & Black, 2000), the Direct Displacement Based Design (DDBD) by (Priestley & Kowalsky, 2000), DDBD with inelastic displacement spectra (Chopra & Goel, 2001) and the method proposed by (Panagiotakos & Fardis, 2001).

Among these methods, the DDBD certainly represents a good compromise between reliability of results and ease of application (Sullivan et al., 2003). Indeed, provided that we are able to estimate with sufficient accuracy some characteristics of the non-linear structure, such as displacements shape and energy dissipation capacity, DDBD allows designing in function of a given level of damage, to be considered acceptable for a given seismic event, without resorting to complex analysis. Initially developed for reinforced concrete frames and bridges, in recent years it has found application also for other structural types, such as RC walls, steel, timber and masonry buildings.

For what concern masonry buildings, DDBD method still suffers from shortcomings (Calvi & Sullivan, 2009a), mainly because of the wide heterogeneity of existing typologies. In particular, a method for defining yielding has not yet been clarified, hence the concept of ductility is difficult to be applied. So, there is still no formulation for estimating the ability to dissipate energy, as in DDBD method this is directly related to ductility, through the definition of equivalent viscous damping. Furthermore, the latter parameter is used to estimate the capacity of inelastic deformation. The aim of the study described in this thesis is therefore to provide

new information for estimating damping and inelastic capacity for masonry structures in seismic area. Two masonry typologies are taken into account, one is modern reinforced masonry, and the other one is historical stone masonry strengthened by hydraulic lime-based grout injections. Both of them have been subjected to experimental tests at the University of Padova, in the framework of two European Research Projects, DISWall (2006-2008) and Niker (2010-2012).

1.2 Aim and Methods

The main aim of this thesis is that of contributing to the knowledge of parameters typical of non-linear cyclic behaviour of masonry systems subjected to combined vertical and horizontal loads. In particular, energy dissipation is considered through the definition of equivalent viscous damping, in the perspective of displacement-based design.

To this aim, recent results of experimental tests performed at the University of Padova on different masonry systems, have been analysed. These include an innovative type of reinforced masonry construction system, characterized by the use of both horizontal and vertical perforated units and bars or prefabricated truss as horizontal reinforcement, and a multi-leaf stone masonry, strengthened by hydraulic lime-based grout injections.

Experimental results were used to develop and calibrate a new hysteretic model, starting from that proposed by (Tomaževič & Lutman, 1996). The model has proven the capability of reproducing the in-plane behaviour of both the studied masonry types. Hence, it has been implemented in Matlab environment, in order to carry out dynamic analyses. These analyses have been used within a procedure with the aim of evaluating the equivalent hysteretic damping in function of the deformation level of the walls. On the basis of the results, simple formulation for evaluating damping, related to different soil types and failure modes, has been calibrated. The results of dynamic analyses allowed evaluating the ratio between elastic and inelastic displacements, and also the relationship between this ratio and equivalent damping.

Lastly, using a finite element model, that has been calibrated on the basis of experimental results of shear-compression tests as a part of other thesis, the procedure has been applied on multi-degree of freedom (MDOF) structure, in order to validate the results obtained for single-degree of freedom (SDOF) systems.

1.3 Thesis Organization

The thesis is divided into 8 chapters. The characteristics of seismic behaviour of masonry buildings are briefly presented in Chapter 2. The motivations of performance-based approaches and the basics of Displacement-Based Design are also summarized, together with a short description of existing models for modelling of cyclic behaviour of masonry walls. Chapter 3 presents the experimental programs, the main data and results of the in-plane tests carried out on systems object of the research, i.e. reinforced masonry and historical stone masonry. The tests were carried out as part of other thesis, and the author took part in both test execution and data analysis.

Chapter 4 present the development of an hysteretic model, starting from one already available in literature and described in Chapter 2. The model is thus applied to both the studied masonry types, and a simulation of in-plane shear tests is performed. In addition, the model is implemented in a numerical code, in order to carry out dynamic analyses of SDOF systems.

A procedure for the determination of equivalent viscous damping is presented in Chapter 5, together with the obtained results. The complete analysis and discussion of results is described in Chapter 6, also in relation with practical design procedure. In Chapter 7 the proposed procedure is applied to a MDOF structure, using a finite element model, to complement the analyses on SDOF system described so far, and the results are presented and discussed. Lastly, Chapter 8 gives the main conclusion of the work.

2 LITERATURE REVIEW

2.1 Introduction

The purpose of this chapter is to give a critical overview of the topics that are object of study in this work. First, a brief description of the state of art for what concern the in-plane behaviour of masonry walls is given. Then it will be described the basics of Displacement Based Design. It is briefly described the application of this method both to single and multi-degree of freedom structures, with particular attention to previous research on the evaluation of equivalent damping and application of the method to masonry structures.

To estimate equivalent damping for masonry structure, it is necessary to use hysteretic models to carry out dynamic analyses. So the models available in literature are discussed and compared.

2.2 Structural Behaviour of Masonry Wall Under Seismic Actions

Modern buildings are designed for earthquake resistance following the basic principles of box-type of behaviour. This assumption implies the presence of rigid diaphragms, in their own plane, able to distribute the horizontal loads to the shear walls (Shing et al., 1990). As a consequence, the main seismic resistance mechanism of the building is related to the in-plane behaviour of the walls (shear walls), whereas the out-of-plane behaviour represents a local mechanism. In fact, the walls perpendicular to the horizontal actions are supported by floors and roofs, which transfer also these horizontal loads to the shear walls. The connections between the walls and with the floors are fundamental to guarantee the development of the box-type behaviour (Fig. 2.1).

Masonry shear walls, according to the type of construction and their configuration, solid or pierced by windows and doors openings, lead to various seismic behaviour and failure mechanism. Three main categories of shear walls are classified (Paulay & Priestley, 1992; Tomaževič, 1999): cantilever walls linked by flexible floor slabs, coupled shear walls with weak piers and coupled shear walls

with weak spandrels (Fig. 2.2). The former resistant model (Fig. 2.2 left) is characterized by floor slabs rigid in their plane, but flexible in the orthogonal direction, therefore they do not transfer any moment between the shear walls. The shear walls are in this case cantilevers fixed on the bottom and free at the top of the building. The critical condition is at the base storey, where large bending moment is developed. In terms of seismic response, the cantilever walls represent a suitable structural behaviour, since it is dominated by flexure, and it guarantees high ductility and energy dissipation, if carefully detailing is provided.

Usually, masonry buildings are made by shear walls (so called since they resist to the lateral shear loads with their in-plane shear capacity (Drysdale & Hamid, 2008)) pierced by window and door openings, in which the spandrels connect the shear walls and transfer the horizontal loads and also bending moments. In this case two main resistant elements are identified: the spandrels, which are the portion of masonry between two overlying openings, and the piers between two next openings. Depending on the proportion of the openings, the weakest elements are the piers (Fig. 2.2 middle) or the spandrels (Fig. 2.2 right).

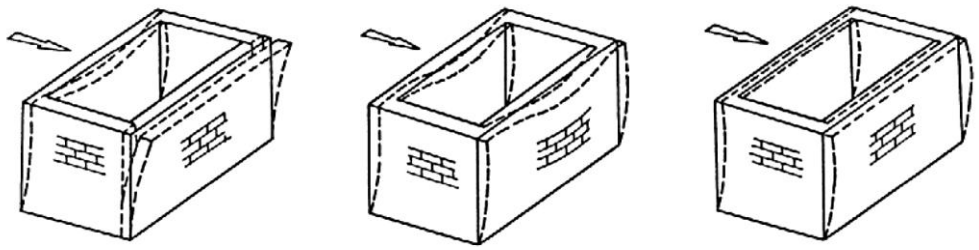

Fig. 2.1 Response of simple masonry building to horizontal actions: building with deformable floors without ties (left), building with deformable floors and tied walls (middle) and building with rigid floors and tie-beams (right) (from Macchi and Magenes, 2002).

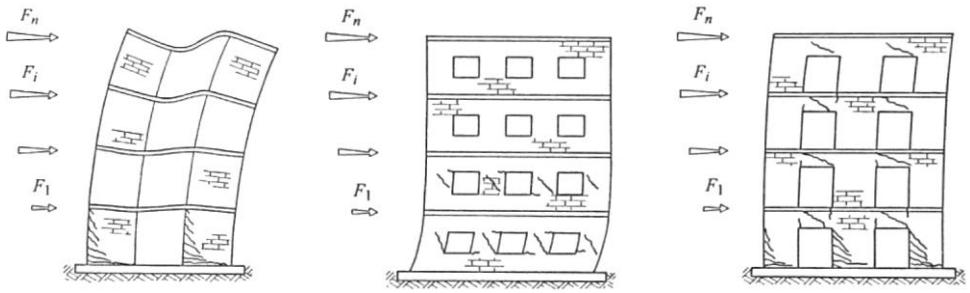

Fig. 2.2 Cantilever walls linked by flexible floor slabs (left), coupled shear walls with weak piers (middle) and coupled shear walls with weak spandrels (right) (from Tomaževič, 1999).

In the case of spandrels reaching failure, they keep transferring the horizontal loads but they transfer only residual part of bending moments. Hence, the global behaviour leads towards to the structural response of cantilever walls linked by flexible floor slabs.

When piers are weaker than spandrels, which is usually the case of traditional unreinforced masonry (URM) construction (Tomaževič, 1999), damage will first involves the piers (Fig. 2.3). Piers will fail in shear or with rocking mechanism according to geometry, materials and vertical loads.

The last failure mechanism is the most sensitive one, because piers withstand vertical loads and shear failure is characterized by low energy dissipation capacity and ductility. Improvement can be provided with adequately distributed reinforcement.

In the case of reinforced masonry (RM) buildings, spandrels and piers can be provided with adequate vertical and horizontal reinforcement, qualitatively showed in Fig. 2.4, in order to obtain predominant flexural behaviour. As a results of capacity design, the lateral resistance, energy dissipation capacity and ductility of the structure are increased. Moreover the hinging of the spandrels, which couple the shear walls, leads to a reduction of bending moment at the base, and energy dissipation capacity is distributed over the entire height of the shear walls. Therefore this mechanism is the most desirable among the three identified mechanisms (Tomaževič, 1999).

Fig. 2.3 Typical shear cracks in window piers of brick masonry building, Budva, Montenegro, 1979 (from Tomaževič, 1999).

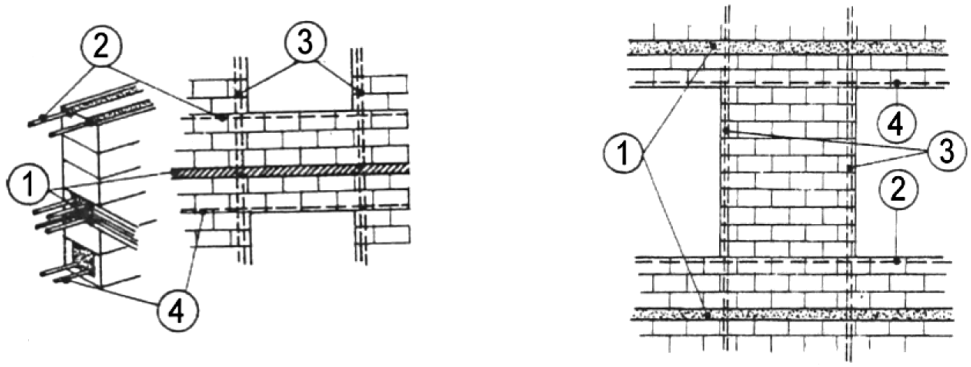

Fig. 2.4 Reinforcement of the spandrel between two overlying openings (left) and reinforcement or window pier (right); 1. Tie-beams, 2. Reinforcement of threshold, 3. Vertical reinforcement, 4. Lintel reinforcement (from Giuffrè, 1980).

In any case, there are some reasons to considerate the cantilever walls system as the best, rather than coupled walls with spandrels hinging, since high ductility demand is concentrated in the coupling spandrels, and they suffer rapid strength and stiffness degradation. This leads to an uncoupling of the shear walls and results in an increase in bending moments for shear walls, which are not able to resist, if they are designed as coupled walls (Paulay & Priestley, 1992).

In most cases, load bearing masonry walls are used for residential buildings, whose configuration varies from single occupancy house, one or two storey high, to the multiple-occupancy residential buildings, which are commonly constituted by two or three-storey when they are built of URM, but can reach relevant height (five-storey or more) when they are built with RM. Intermediate types of buildings include two-storey, semi-detached two-family houses or attached row houses. In these buildings, the masonry walls carry the gravity loads and they usually support concrete floor slabs and roofs, which are characterized by adequate in-plane stiffness. The inter-storey height is generally low, around 3 m.

In these structures, the seismic resistance mechanism, and in general the resistance to horizontal actions, is provided by coupled shear walls, as above discussed. It must be also reminded that, in certain cases, in particular for low-rise residential buildings such as single occupancy houses or two-family houses, the roof structures can be made of wooden beams and can be deformable, even in new buildings. In these cases, or in the upper storey of multi-storey (multiple-occupancy) residential buildings and for one-storey industrial or commercial buildings with deformable roofs and no bracing walls, wall designs can be governed by resistance to out-of-plane forces (Mosele, 2009).

2.2.1 Failure modes of masonry walls

Some systematic studies aimed at the definition of the complete failure envelope of masonry, were developed for the entire range of combinations of ideal biaxial stress state. The first investigations were experimentally carried out with the test on square masonry panels tested under different combination of tension and compression and different orientation of loading with respect to the head and bed joints. They allowed defining the experimental failure criteria for brick masonry (Page, 1980; Page, 1981; Page, 1983; Samarasinghe & Hendry, 1980), for concrete block masonry (Hamid & Drysdale, 1980; Hamid & Drysdale, 1981; Hegermeir et al., 1978) and for masonry made of perforated clay blocks (Ganz & Thürlimann, 1984). Fig. 2.5 left shows the failure envelope found for brick masonry by (Page, 1982), where the anisotropic behaviour of masonry is evidenced by the different shapes obtaining varying the loading angle and by the corresponding observed failure modes, Fig. 2.5 right.

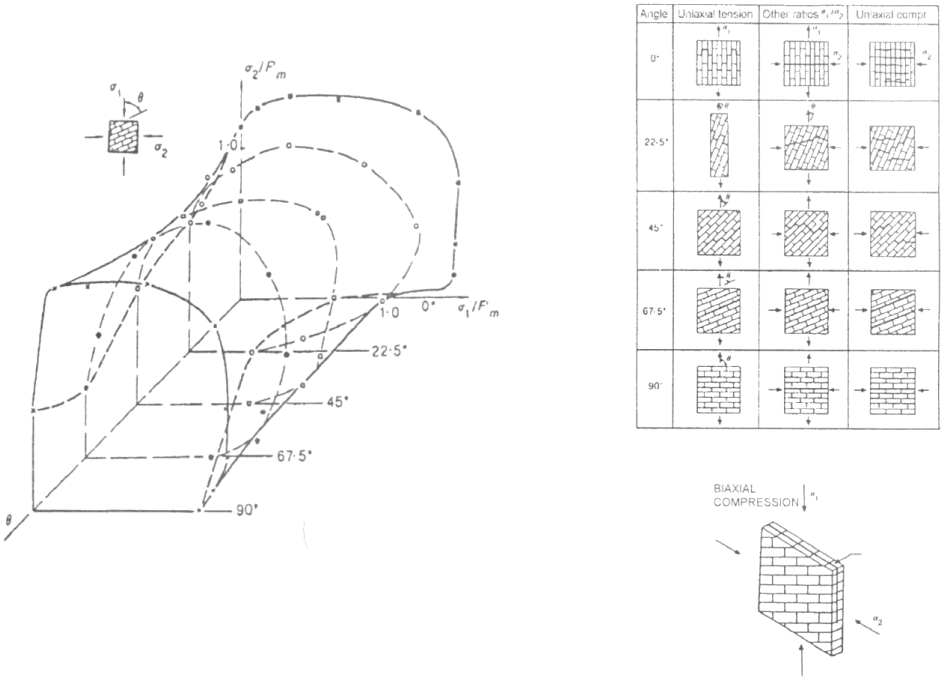

Fig. 2.5 Experimental failure criteria for brick masonry walls under biaxial compression (left) and failure modes (right) for brick masonry walls under uniaxial and biaxial stress state (from Page, 1982).

A typical case of biaxial stress state is masonry pier under combined vertical and horizontal load (Fig. 2.6). The homogeneous stress states found e.g. by (Page,

1982) interest only a part of shear walls which are rather subjected to homogeneous stress states. Considering that the appearance of one failure mechanism depends on parameters such as the geometry of the masonry walls and the ratio of vertical to horizontal load (Tomaževič, 1999), that failure characterizes the behaviour of a masonry wall in a structure, rather than the simple material behaviour.

First appearance of failure usually involves the centre of shear wall or stretched corner (A and B zones in Fig. 2.6) or in the more compressed corner of pier (C zone in Fig. 2.6). It was experimentally verified from above mentioned researchers that the main failure modes relevant for masonry walls are:

- Flexural failure;
- Diagonal shear cracking;
- Sliding on bed joints;

These failure modes are schematically represented in Fig. 2.7. The first mechanism is ruled by compressive strength of masonry, and is characterized by the early appearance of crack in joint under tension stress state (B zone in Fig. 2.6), followed by a second limit state characterized by crushing of compressed toe of pier (C zone in Fig. 2.6).

Shear failure, on the contrary, can involve different failure mechanisms, in particular: failure can involve the horizontal and vertical joints causing a stepped-crack; or failure can involve also the blocks (or bricks) giving a diagonal cracking which pass throughout masonry units and joints. The third shear failure mechanism is the sliding along bed joints with an almost horizontal crack progress. This mechanism is less frequent an can be mainly imputed to poor quality of mortar and/or low vertical stress. In general, this failure mechanism do not appear for both new URM and RM made with perforated clay units (da Porto et al., 2005; Mosele, 2009).

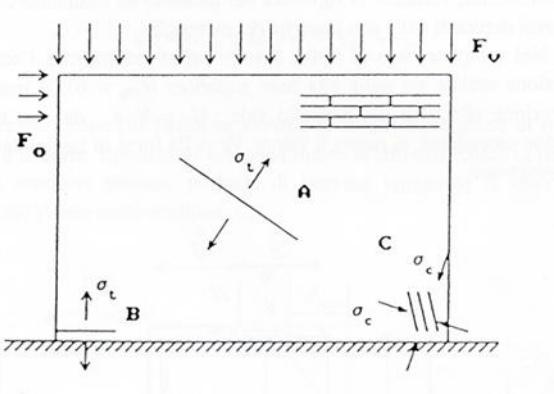

Fig. 2.6 Failure mechanisms of wall portion subjected to vertical and horizontal actions (from Andreaus, 1996).

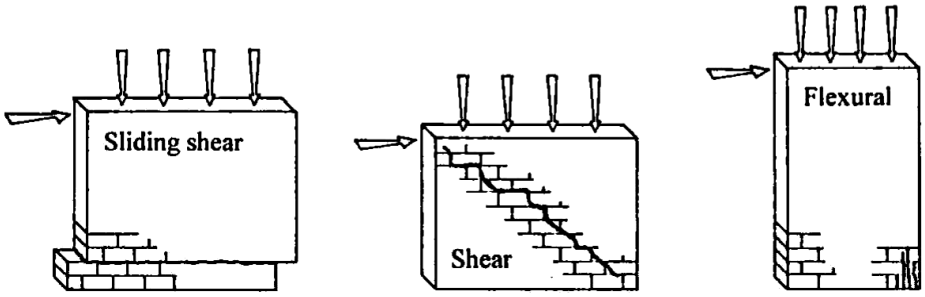

Fig. 2.7 Main failure modes of masonry walls, subjected to in-plane seismic load (from Tomaževič, 1999).

2.2.2 Flexural failure

In the case of URM pier under combined vertical and horizontal loads, the maximum horizontal load, associated to flexural failure, may be approximated introducing a proper stress distribution for the masonry in compression and neglecting the tensile stress of bed joints. Simple equilibrium equations lead to the following expression:

$$V_{fl} = \frac{D^2 t}{H_0}\frac{p}{2}\left(1 - \frac{p}{k f_u}\right) \qquad \textit{(Eq. 2.1)}$$

where D is the pier length, H_0 is the effective pier height, t is the pier thickness, p is the mean vertical stress, f_u is the compressive strength of masonry and k is a coefficient which takes into account the vertical stress distribution at the compressed toe (Fig. 2.8). This is the approach adopted in the Italian Technical Code, NTC 2008 (DM 14/01/2008, 2008), taking k = 0.85. The effective height is defined as the height of zero moment from the bottom, so it is determined by the boundary conditions of the wall and is related to shear ratio α_v, which is expressed by

$$\alpha_v = \frac{M}{VD} = \frac{H_0}{D} \qquad \textit{(Eq. 2.2)}$$

It can be seen that (Eq. 2.1) has a low sensitivity to the parameters k and f_u, in the range of low mean vertical stresses, while is strongly affected by the parameter α_v.

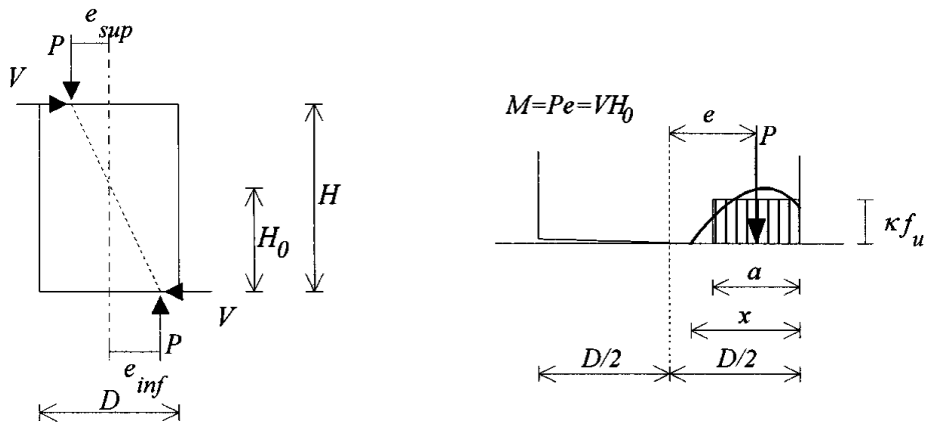

Fig. 2.8 Assumption for flexural strength evaluation of a wall failing with crushing at the base corner (from Magenes & Calvi, 1997).

In the case of RM, the flexural failure mode is related to yielding of vertical reinforcement at the tensioned side of the base, and crushing of masonry at compressed toe side. Furthermore, buckling of compression reinforcement accompanies crushing of masonry units. Under the usual hypothesis for flexure theory, such as plain sections remain plain and linear strain distribution, and assuming yielding of tension and compression vertical reinforcements, which allow to direct calculation of the depth of stress block (a), the flexural capacity of the reinforced masonry wall's section can be evaluated by adding to (Eq. 2.1) the contribution of reinforcement. In the case of symmetrical vertical reinforcement at the ends of the wall, the following equation is thus obtained:

$$M_u = M_{u,w} + M_{u,rv} = \frac{ptl^2}{2}\left(1 - \frac{p}{kf_u}\right) + zA_{rv}f_y \qquad \textit{(Eq. 2.3)}$$

Where $M_{u,w}$ is the contribute of masonry and $M_{u,rv}$ is contribute of vertical reinforcement to the flexural capacity, z is the lever arm of the torque force moment of vertical reinforcement. This is the approach adopted both in NTC 2008 and Eurocode 6, EC6 (EN 1996-1-1, 2005), with the difference that in the latter the stress-strain relationship can be taken also to be linear, parabolic, or parabolic rectangular. In both the codes limits for compressive strain of masonry and tensile strain of reinforcement are provided.

2.2.3 Shear failure

The shear failure is, due to typical mechanical properties of masonry materials and the geometry of structural walls, the most common type of failure of a masonry wall subjected to seismic loads (Tomaževič, 1999). The two most common approaches developed and adopted by codes for the determination of shear strength are based on the Mohr-Coulomb formulation or by the definition of a reference tensile strength which is reached at the centre of the panel. The first, which is adopted in several codes (i.e. NTC 2008 and EC6) is expressed by (Eq. 2.4):

$$\tau_u = c + \mu\sigma_v \qquad \textit{(Eq. 2.4)}$$

where c is the material shear strength and μ is the friction coefficient. This coefficient have the meaning of global strength parameters and cannot be related to local material properties, since the real stress distribution is not uniform (Magenes & Calvi, 1997). σ_v is the mean vertical stress calculated on the effective resisting section, which is defined by the effective uncracked length l_c. If the tensile strength of bed joints is neglected and assuming a linear distribution of compressive stresses, the following expression (Eq. 2.5) for the determination of l_c is obtained:

$$l_c = 3\left(\frac{l}{2} - \frac{VH_0}{P}\right) \qquad \textit{(Eq. 2.5)}$$

The second criterion was proposed by (Turnšek & Čačovič, 1971), and assumes that diagonal cracks at shear failure are caused by the principal tensile stresses which develop in the wall when subjected to a combination of vertical and lateral load. By considering the masonry wall as an elastic, homogeneous and isotropic material, the principal tensile stresses develop in the middle section of the panel is expressed by (Eq. 2.6):

$$\sigma_t = \sqrt{\left(\frac{\sigma_0}{2}\right)^2 + (b\tau)^2} - \frac{\sigma_0}{2} \qquad \textit{(Eq. 2.6)}$$

where τ is the average shear stress and b is the shear distribution factor, which takes into account the distribution of shear stress. For a parabolic distribution, reasonable for high aspect ratios, b is equal to 1.5, whereas a constant distribution, more realistic for aspect ratio close to one, involves b equal to 1. (Benedetti & Tomaževič, 1984) proposed the consider b = 1 for H/D ≤ 1, b = H/D for

$1 < H/D < 1.5$ and $b = 1.5$ for $H/D \geq 1.5$. The shear strength of masonry can be taken as the average shear stress τ at the attainment of the referential tensile stress, i.e. $\sigma_t = f_t$, which leads to (Eq. 2.7), that is adopted in NTC 2008 in the case of existing buildings with irregular masonry or for units with quite low compressive strength (Circolare 2/02/2009 n. 617 C.S.LL.PP., 2009).

$$V_{sh} = \frac{f_t l t}{b}\sqrt{1 + \frac{\sigma_0}{f_t}} \qquad \textit{(Eq. 2.7)}$$

In the case of RM, normally the code considered the shear strength by adding to the computed masonry strength ($V_{sh,M}$) a term that takes into account the horizontal reinforcement contribution ($V_{sh,S}$). The latter is generally estimated as for stirrups for reinforced concrete members, giving (Eq. 2.8):

$$V_{sh} = V_{sh,M} + V_{sh,S} = \tau_u d t + C_{eff}\frac{d}{s}A_{rh}f_y \qquad \textit{(Eq. 2.8)}$$

Where A_{rh} is the area of horizontal reinforcement, s is the spacing of shear reinforcement and C_{eff} is the effectiveness of reinforcement factor, which takes into account the reduced effectiveness of shear reinforcement due to bond failure between mortar and steel. In NTC 2008 the value of C_{eff} is 0.6, this value has been experimentally confirmed by (Mosele, 2009), and d is the distance between compressed edge and the barycentre of tensioned reinforcement. (Tomaževič, 1999) considered C_{eff} = 0.9, but proposed to reduce the contribution of reinforcement by means a horizontal reinforcement reduction factor C_{rh}, that he suggested to consider equal to 0.3. Furthermore he proposed to consider the contribution due to dowel action of vertical reinforcement.

In NTC 2008 is also prescribed to verify the following condition:

$$V_{sh} < 0.3 f_u t d \qquad \textit{(Eq. 2.9)}$$

This can be seen as a verification of compressed strut, that is not considered in EC6, where, furthermore, the contribution $V_{sh,S}$ is computed taking into account the total area of horizontal reinforcement (A_{SW}) and C_{eff} = 0.9, giving:

$$V_{sh,S} = 0.9 A_{SW} f_y \qquad \textit{(Eq. 2.10)}$$

2.3 Modelling of the In-plane Behaviour of Masonry Walls

2.3.1 Construction of Idealized Envelope

The experimental results of tests carried out under combined vertical and horizontal in-plane cyclic loading on both URM and RM are generally approximated by means of envelope curves defined by the maximum load-displacement values reached in any cycle by the specimen. On the basis of the experimental envelopes, idealized bilinear force displacement relationships can be defined (Tomaževič, 1999), taking into account the equal energy dissipation capacity of the actual and the idealized masonry wall (Fig. 2.9). Also tri-linear shapes were proposed for the idealization of the resistance envelope curve of confined and reinforced masonry (Modena, 1992; Tomaževič, 1999), Fig. 2.10.

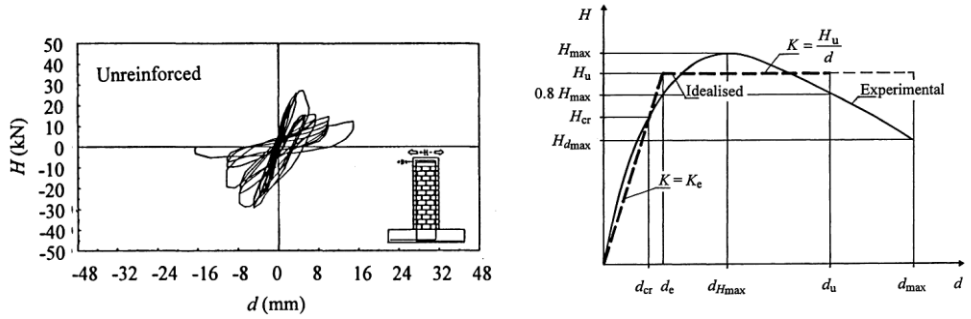

Fig. 2.9 Actual (left) and idealized elastic-perfectly plastic force-displacement relationship (right) for an URM specimen (from Tomaževič, 1999).

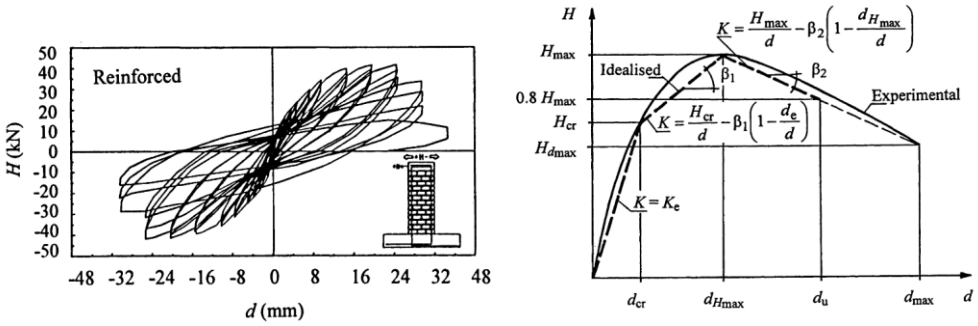

Fig. 2.10 Actual (left) and idealized tri-linear force-displacement relationship (right) for a RM specimen (from Tomaževič, 1999).

The construction of the idealized envelope curves can be also based on the observation, during the experimental testing, of three limit states (LSs) reached by

the masonry specimens. They are the shear cracking limit, characterized by the opening of the first significant shear crack in the specimen, the maximum resistance, characterized by the attainment of the maximum lateral strength, and the ultimate state, characterized by the attainment of the maximum displacement, before the specimen collapse. Also a fourth limit state, which occurs before the other three, can be observed. It consists in the opening of mortar joints in the lower part of the specimens, due to flexural effects. (Abrams, 2001) has proposed to systematically use these four limit states to idealize the masonry wall behaviour, relating them to performance levels of actual buildings. In these terms, the flexural limit can be designated as a “First Crack” level, and represent a damage limit state, whereas the appearance of the first diagonal crack is associated with the first signs of structural damage typically observed during the earthquakes, and can be related to the “Immediate Occupancy”. The attainment of the maximum resistance can be considered, in terms of performance level, as a “Life Safety” state and, finally, the ultimate state determined by the attainment of the maximum displacement can be designated as a “Collapse Prevention” state (Bosiljkov et al., 2003). Fig. 2.11 shows a schematization of the four limit states during the in-plane cyclic tests.

This type of simplified models is very useful to compare the performances of different types of masonry, in terms of initial stiffness, maximum resistance and ultimate ductility reached by the walls. The bilinear idealized force displacement relationships can be, furthermore, used for non-linear static (push-over) analysis procedure also adopted by the codes, (EN 1998-1, 2004) and (DM 14/01/2008, 2008).

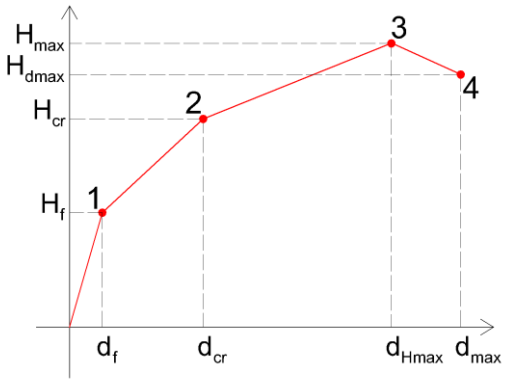

Fig. 2.11 Schematization of the four limit states.

However, these models are not able to represent the actual hysteretic behaviour of masonry walls, which gives information also on the energy dissipation capacity

and the stiffness and strength degradation of a wall subjected to sequence of lateral load reversal. With more sophisticated procedures, it is also possible to model the hysteretic behaviour of plain URM and RM walls.

Indeed, data on the hysteretic behaviour of the walls, such as strength and stiffness degradation and energy dissipation capacity, can be obtained only by experimental simulation of seismic behaviour of masonry walls as a whole (Tomaževič, 1999). Starting from experimental results, several researchers have proposed analytical models, able to reproduce the hysteretic behaviour of varies types of masonry walls.

Non-linear finite element modelling has been recognized as a general and efficient method for analysis of the load-bearing and displacement capacity of masonry systems, and can accurately describe the pre-peak and post-peak behaviour of masonry under different monotonic load combinations by adopting inelastic constitutive material models (Gambarotta & Lagomarsino, 1997a; Gambarotta & Lagomarsino, 1997b; Lourenço, 1996; Rots, 1997). Conversely, cyclic behaviour can better be described by damage-based material models (Calderini & Lagomarsino, 2008; Gambarotta & Lagomarsino, 1997a; Gambarotta & Lagomarsino, 1997b) than by those implementing plasticity concepts (Lourenço, 1996; Rots, 1997).

2.3.2 Analytical Modelling

(Modena, 1982) proposed, for URM, a model based on the experimental results of cyclic tests, in the non-dimensional variables H/H_{max} and δ/δ_s, defined by a symmetrical envelope curve on which the construction of the hysteresis loops is based Fig. 2.12. Each portion of the envelope curve is constituted by an initial linear branch, until the attainment of the displacement level λ equal to δ/δ_s, and by a subsequent non-linear branch, defined by (Eq. 2.11):

$$\frac{H}{H_{max}} = (1-\mu)\cdot\left[\frac{\frac{\delta}{\delta_s}-\lambda}{\mu-\lambda}\right]^{\frac{\mu-\lambda}{\mu-1}} + \frac{\delta}{\delta_s} \qquad \textit{(Eq. 2.11)}$$

Where δ_p is the displacement at the end of the linear branch, δ_s is the displacement at the idealized elastic limit, $\lambda = \delta_p/\delta_s$ and $\mu = \delta_{Hmax}/\delta_s$ is a ductility ratio at the attainment of the maximum resistance of the wall.

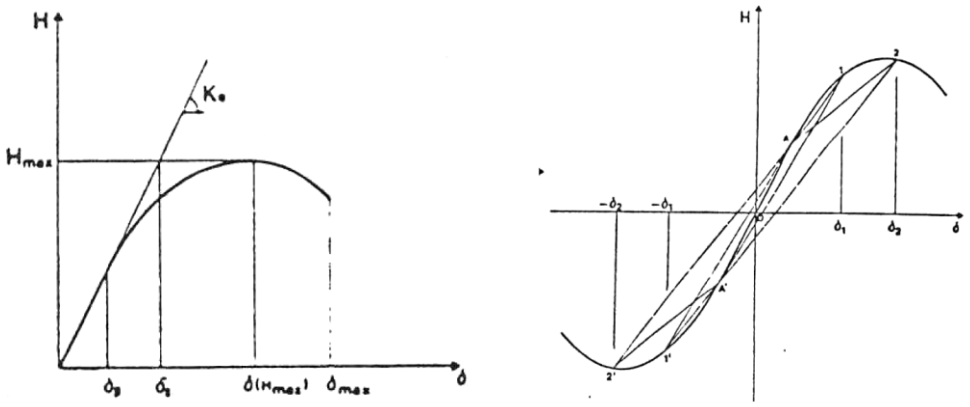

Fig. 2.12 Characteristic parameters of the load-displacement envelope curve (left) and hysteretic behaviour model of URM walls (from Modena, 1982).

This model is basically able to reproduce the small area of each cycle, related to the low dissipation capacity of URM, and the strength and stiffness sudden decrease after the maximum strength limit state. This was later on used by (da Porto et al., 2009) for estimating the load reduction factors of modern types of unreinforced clay masonry.

Later on, (Bernardini et al., 1984) and (Modena, 1992) modelled the behaviour of RM on the basis of a tri-linear envelope model, introducing five non-dimensional parameters, four describing the shape of the experimental envelope curve of cyclic tests and the major cycles and one, μ_a, defining the available ductility. Three out of the four shape parameters were based on the ratio between the horizontal loads and the displacements at relevant states, whereas the fourth (P4) was able to describe the stiffness degradation. Fig. 2.13 left shows the described model. Following, a procedure based on the use of the dissipated energy to lower the load-displacement curve obtained during a monotonic test and fit it to the envelope curve of the cyclic tests was developed (Modena, 1992). A similar procedure was also adopted to introduce another parameter that allows adapting an envelope curve obtained by means of a static test to the envelope curve of a test carried out with dynamic loading, Fig. 2.13 right (Modena & Barel, 1987). Based on these models, he carried out non-linear dynamic analyses for the definition of behaviour factors q.

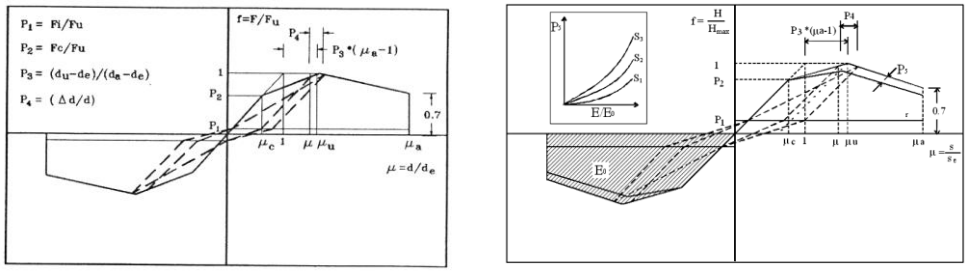

Fig. 2.13 Non-dimensional analytical model of the cyclic behaviour of RM walls, left (from Bernardini et al., 1984) and its development, right (from Modena and Barel, 1987).

Tomaževič (Tomaževič & Lutman, 1996) defined the envelope curve of cyclic tests starting from the experimental results of monotonic tests. To find this correlation, he introduced the parameter of fictitious input energy, where the value of lateral resisting force for the calculation of the input energy, corresponding to any given displacement of a cyclic time history, is taken from the equivalent monotonic curve. To model the hysteretic behaviour, he takes into account three parameters, two depending on the experimental stiffness degradation, which influences the slope and shape of hysteresis loops at unloading. The other one is the strength degradation, based on the amount of dissipated hysteretic energy during one cycle of loading. Furthermore, the model was further developed by (Bernardini et al., 1997), by relating the strength degradation on the amount of absorbed, instead of dissipated, energy. On these models was based the development of another model, which was used to estimate load reduction factors for reinforced masonry (da Porto et al., 2008; Mosele, 2009; Nicolini, 2008).

(Wakabayashi & Nakamura, 1984) combined arch and truss mechanisms in order to predict horizontal load-displacement monotonic curve in the case of shear failure of RM walls. For each mechanism, they considered four equations: two are compatibility conditions and two equilibrium equations. It is assumed that the total response of the wall is the sum of the behaviour of the two mechanisms. Furthermore, on the basis of the monotonic envelope abovementioned, the authors proposed a formulation of hysteresis loops as a sum of three basic loops: a degrading model, a slip model and a bi-linear-model. This sum is ruled by means three parameters, which have to be determined on the basis of experimental investigations. The model was compared with static cyclic tests and shaking table tests, giving very good results in the former case and reasonable accuracy in the latter.

Other models that can be quoted are those from (Tassios, 1988). Tassios developed a semi-empirical criteria, called “stereo-static model”, based on both experimental and of numerical results, where the envelope curve and the hysteretic

rules of RM are modelled by taking into account the local resisting mechanisms, such as dowel action and pull-out of reinforcement and friction mechanisms within the cracks.

(Kamil Tanrikulu et al., 1992) modelled the skeleton curves for the shear modulus G and its viscous counterpart G' by means of bilinear and tri-linear curves based on five experimentally determined parameters that he gave for masonry made of burned-clay bricks, stone units and adobe masonry walls. On the basis of the same parameters, he also explained the loading and unloading characteristics during an earthquake excitation, in order to model the hysteretic behaviour of studied plain masonry walls.

(Magenes et al., 1997) proposed again a hysteretic non-linear law, developed on the basis of previous models studied at the University of Pavia, calibrated on the basis of experiments on RM shear walls. This law was used to model the global inter-storey shear-displacement behaviour of a building by means of non-linear dynamic analyses. The model is based on five empirical relationships, which are used to linearize significant portion of the experimental hysteretic loops, where the strength and stiffness degradation and the other energetic and displacement parameters are mainly based on the cumulative input and dissipated energy.

2.3.2.1 Tomaževič Model

In this section, a more detailed description of the Tomaževič model is given. Indeed, this model can be considered as a good compromise between simplicity of modelling and accuracy of predicted response. The model is based on that proposed by (Park et al., 1987), and taking into account some experimental observations on actual non-linear behaviour of tested RM walls. The tests were performed on 32 equal RM walls subjected to different imposed lateral displacement patterns: monotonic and cyclic, static and dynamic, at two level of vertical load. A summary of experimental results can be found in (Tomaževič et al., 1996).

The skeleton curve is the symmetric, tri-linear idealized envelope defined by the observed three limit states, i.e. cracking point, maximum resistance and ultimate limit state. The general scheme of the model is shown in Fig. 2.14 left, and is based on the following rules:

- Loading path 0-1-A-2-B is following the hysteresis envelope until the change in sign of direction of loading.
- Unloading path B-3-C: stiffness degradation takes place immediately after the attainment of lateral displacement at cracking of the wall d_{cr}.
- Unloading path C-4-D is aimed at point D, defining the negative cracking LS.
- Negative loading path D-5-E-6-F is following the negative branch of hysteresis envelope until the change of sign of the direction of loading.
- Negative unloading path F-7-G: stiffness degradation parameter C_K defines the unloading stiffness of line F-7-G. Unloading stiffness shape parameter C_F defines point G: $H_G=C_F \cdot H_F$.

The stiffness degradation is modelled by the two scalar parameters C_K and C_F. The former defines the slope of the first unloading branch (B-3-C and F-7-G), and is calculated by (Eq. 2.12), where K_e is the elastic stiffness and K_u is the ultimate stiffness, i.e. secant stiffness's related to cracking and ultimate LS respectively. The model assumes that the degradation of unloading stiffness, K(R), begins after the attainment of maximum resistance LS. K(R) is defined by (Eq. 2.13).

Shape parameter C_F defines the width of the cycle, it is evaluated by making equal the area below the unloading branch of hysteresis loop. Applying this method to each cycle, several values of C_F are obtained, i.e. one value for each experimental cycle. Since the authors affirm to have obtained the value of 0.7, it is inferred that it represents the averaged value.

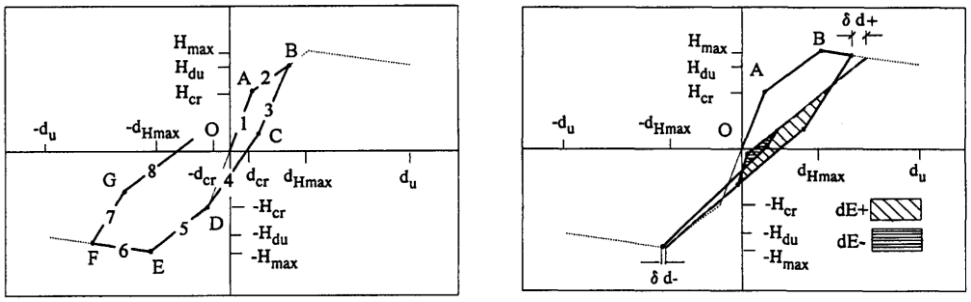

Fig. 2.14 General scheme of model, left, and definition of strength degradation parameter β, right (from Tomaževič et al., 1996).

$$C_K = \frac{(K_u/K_e) - 1}{(d_u/d_{cr}) - 1} \qquad \textit{(Eq. 2.12)}$$

$$K(R) = K(1)\left[1 + C_K\left(\frac{d_R}{d_{Hmax}} - 1\right)\right]0 \qquad \textit{(Eq. 2.13)}$$

Another scalar parameter, β, is used to model the strength degradation at repeated load reversals. This parameter allows to calculate the incremental increase in target displacement on the hysteresis envelope due to dissipated energy, distinguishing between the loading in both positive (δd^+) and negative (δd^-) directions, Fig. 2.14 right. Although the calculated values of parameter β are quite scattered, the authors have noted that the averaged values are close to 0.06 in all the cases considered. As for the shape parameter, the model considers the averaged value of parameter β.

2.3.3 Finite Element Modelling

The finite element method offers a widespread variety of possibility concerning the description of masonry structures within the frame of detailed non-linear analysis. Numeric representation of masonry can be achieved by modelling masonry constituents separately (units and mortar joints, micro-modelling approach, Fig. 2.15b,c), or by following a global approach in which the whole structure is schematized as a continuum without any distinction between masonry constituents (macro-modelling, Fig. 2.15d). The first approach can again be subdivided into detailed micro-modelling (Fig. 2.15b) in which units and mortar joints are

represented by continuum elements and contact surfaces between units and mortar by interface elements, and simplified micro-modelling (Fig. 2.15c), in which expanded units are represented by continuum elements and non-linear behaviour of mortar joints and contact surfaces is collapsed into interface elements.

The micro-modelling strategy for masonry has mainly focused on the development of reliable interface models, since the first introduced by (Page, 1978). Several constitutive laws were defined, incorporating damage and plasticity concepts (Gambarotta & Lagomarsino, 1997a; Rots, 1997) or plasticity theory only (Giambanco et al., 2001; Lotfi & Shing, 1994; Lourenço & Rots, 1997). (Lourenço, 1996) developed an interesting interface model under multi-surface plasticity theory, in which not only shear and tensile but also compressive behaviour can be taken into account through a cap model (Fig. 2.16). This interface model was further developed with a refined description of the dilatancy phenomenon by (van Zijl, 2004)

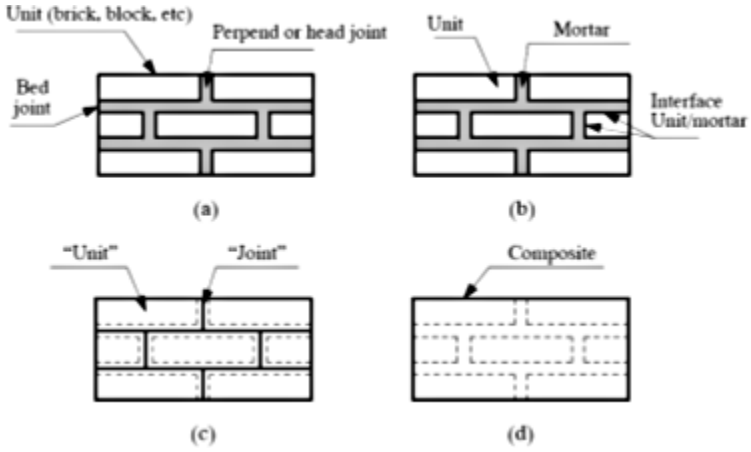

Fig. 2.15 Different modelling strategies for masonry structures: (a) real masonry specimen, (b) detailed micro-modelling, (c) simplified micro-modelling, (d) macro modelling (Lourenço, 1996).

Appropriate modelling of cracks through units is of basic importance, to avoid an over-stiff response and a considerable higher failure load of the numerical models than those experimentally determined (Chaimoon & Attard, 2007; Lourenço, 1996).

Within micro-modelling, cracks through masonry units can be accommodated by employing two main strategies. In the case of bricks, the insertion of a central potential vertical crack by means of interface elements suffices to simulate global behaviour correctly (Lourenço, 1996; Rots, 1997). The use of smeared crack models is more appropriate for blocks that may undergo distributed cracking (Giambanco et al., 2001; Lotfi & Shing, 1994; Rots, 1997). It is worth mentioning

that the first approach turned out to be very robust, whereas the second may present some convergence problems due to bifurcation (Lourenço, 1996; Rots, 1997).

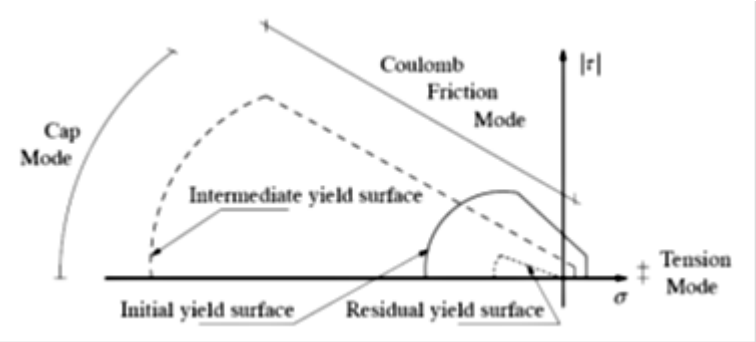

Fig. 2.16 Limit failure surfaces for interface model (Lourenço, 1996).

Macro-modelling commonly uses non-linear anisotropic constitutive material models. In some simplified cases, non-linear isotropic models are also employed. Several materials models are available for masonry, incorporating either damage (Calderini & Lagomarsino, 2008; de Borst, 2002; Gambarotta & Lagomarsino, 1997b) or multi-surface plasticity theory (Lourenço et al., 1997; Rots, 1997). Mechanical parameters may be derived from experimental data or deduced from homogenization techniques (Calderini & Lagomarsino, 2008; Pegon & Anthoine, 1997). This approach becomes effective when units and mortar joints can be taken into account on average; when this is not provided, possible discrepancies between real and numerical behaviour may arise (Lourenço, 1996; Lourenço et al., 1997). The smeared-crack scalar damage models or other similar models, such as that presented in (Faria et al., 1998) for massive concrete structures, are also used in macro-modelling of masonry. In this type of models, the damage is defined in a given point by a scalar value which defines the level of degradation, that ranges from the elastic state until collapse, and the cracking is considered as distributed along the structure.

Micro-modelling strategy is more detailed and is a valuable tool to reproduce masonry assemblages tested during experimental research. It requires a large number of parameters, but facilitates understanding of the local behaviour of masonry and parameterizing the results of experimental trials. Conversely, it is not suitable for simulating the global behaviour of buildings, since the computational burden is usually excessive. The macro-modelling approach is less detailed, but depends on a limited number of parameters. It is suitable for large structures, thus becoming more attractive for practice-oriented analyses.

2.4 Basics of Displacement-Based Design

Force-based seismic design remains nowadays the more widespread design method. In spite of this, in the last decades, the awareness of how the deformation, and not force, is the more meaningful parameter in order to quantify the expected damage from an earthquake has arisen (Moehle, 1992; Priestley, 1993). For elastic systems, forces and displacements are directly connected through the system stiffness. But real structures behave inelastically, and so the relationship is more complex.

In the current seismic codes, the capacity of inelastic systems is evaluated by means of concepts of load-reduction factor and ductility. In order to explain the limitations of this approach, in the following section a brief summary of force-based design is reported.

2.4.1 Brief Review of Force-Based Design

The first step is to estimate the fundamental period of vibration of the structure. In the case of linear static analyses, building codes often propose a simplified formula for estimating the period. Such an approach is independent of member stiffness and mass distribution. Instead, in the case of multi-modal analysis, these characteristics are taken into account. The seismic action is defined by means of the elastic acceleration spectrum. This spectrum is defined on the basis of the site of construction, soil type, and the return period. The elastic response corresponding to natural period(s) is then scaled by load-reduction factor R. This factor is given by the design code on the basis of structural system and material.

At this point it is possible to calculate the base shear force V_B. V_B can be distributed to the structure proportionally to the product of height and mass at different levels. Another possibility is to distribute V_B proportionally to mode(s) shape(s). In the case of multi-modal analysis, the seismic effects have to be combined, and this is possible only using statistical methods. In any case, seismic force is distributed between structural elements in proportion to their elastic stiffness.

Finally, structural elements can be checked, by means of strength verification at member sections level. If an element is not verified, it must be redesigned. This means changing the distribution of stiffness, and so a new analysis is required. When all the structure is verified, the displacements under seismic action can be estimated. Especially for damage limit states, additional verifications in terms of displacement capacity and interstorey drift are required.

The traditional force-based approach has the following limitations (Priestley, 2000):

- An estimate of the fundamental period is required to start the design process, as the period of the structure to be designed is not known. The empirical formulations provided by codes introduce necessarily an error, so generally tend to be conservative. But the displacement demand obtained at low periods is lesser than the actual, hence non-conservative.
- The load reduction factor R is given by code depending of the material of construction and the type of structural system used. This factor takes into account both the stiffness degradation and the dissipation of energy (Borzi et al., 2001). As for fundamental period, the assumption of code-prescribed values for factor R introduces an error.
- For the structures characterized by two or more load paths, the distribution of seismic forces on the basis of initial stiffness is not rational. Indeed, it is not probable that yielding occurs simultaneously in different elements.

In order to overcome the limitations of traditional force-based design methods, in the last decades several alternative approaches have been developed. These approaches are called “Performance Based Design”, since their aim is to achieve a specified performance level. An exhaustive overview of these methods can be found in (Sullivan et al., 2003). Among the several proposed methods, the Direct Displacement-Based Design (DDBD) can be regarded as a good compromise among simplicity of application, set of recommendations and quality of results. However, this method is still under development. For example, in Italy, a research line (linea 4) of the last RELUIS project had the aim to study the application of DDBD method for several structural type. The main result of this work is represented by Model Code for DDBD (Calvi & Sullivan, 2009b). The new RELUIS project intends to take into account the application of DDBD method also for the assessment of capacity of existing structures.

2.4.2 Fundamentals of Displacement-Based Design

The DDBD method has been developed by (Kowalsky et al., 1995) and (Calvi & Kingsley, 1996). The fundamental difference from force-based design is that DDBD characterizes the structure to be designed by a single-degree-of-freedom (SDOF) representation of performance at peak displacement response, rather than by its initial elastic characteristics.

It is based on the identification, in the initial phase of design process, of a design displacement (Δ_d) that ensures an acceptable damage level for the considered seismic intensity. The method assumes that this displacement can be determined without knowing the strength of structure. More precisely, the assumption is that damage is strain-related for structural elements, and drift-related for non-structural elements.

The equivalent structure is other important concept of the procedure, and was introduced by (Gulkan & Sozen, 1974) and (Shibata & Sozen, 1976). This concept enables to represent the inelastic behaviour of a complex structure through a single degree of freedom equivalent system. In such a way it is possible to use elastic displacement spectra, given by the code, while taking into account the deformation capacity of the real system. It has to pointed out that generally code displacement spectra are obtained from the acceleration spectra assuming the peak response as steady-state harmonic response. Such an approximation leads to not so reliable results, in particular for long periods (Bommer & Elnashai, 1999). So the definition of more reliable displacement spectra is still under investigation (Bommer & Pinho, 2006; Faccioli et al., 2004; Paolucci et al., 2008).

DDBD method also needs the definition of equivalent viscous damping (ξ_{eq}). This parameter depends on the system capacity, when it undergoes seismic action, to dissipate energy and it varies in function of structural typology. Once defined both design displacement and ξ_{eq}, it is possible to determine the effective period T_{eff} of equivalent SDOF system by applying a reduction factor to the elastic displacement spectrum. This reduction factor is normally defined, as in the case of (EN 1998-1, 2004) and (DM 14/01/2008, 2008), using the equivalent viscous damping.

Starting from effective period it is simple to compute the effective stiffness of equivalent SDOF system. Hence, the design base shear is obtained by multiplying this stiffness for design displacement. The use of effective stiffness enables the evolving of inelastic forces related to given stiffness at each structural element.

2.4.2.1 DDBD method for a SDOF system

In the following, the principal steps of the procedure for a SDOF structure are reported.

1. Selection of design displacement.

From experimental and analytical results (Priestley, 1993), it has been demonstrated that the yield curvature, for reinforced concrete and masonry elements, is essentially independent of percentage of reinforcement and axial load level, whereas it is more directly related to yield strain and section depth. For

example, the equation for estimating the yield curvature for a rectangular concrete wall is:

$$\Phi_y = 2.00 \cdot \epsilon_y / l_w \qquad \textit{(Eq. 2.14)}$$

Where ε_y is the yield strain of vertical reinforcement and l_w is the wall depth. Starting from yield curvature, it is possible to compute the yield displacement Δ_y. At this point, by introducing the design ductility μ_d, it is easy to obtain Δ_d:

$$\mu_d = {\Delta_d}/{\Delta_y} \qquad \textit{(Eq. 2.15)}$$

Obviously, Δ_d has to respect eventual code drift limits, and so a correction of μ_d could be needed.

2. Estimation of equivalent viscous damping.

With the correct value of μ_d it is possible to estimate the value of the equivalent viscous damping ξ_{eq}. A more detailed discussion on how this parameter could be evaluated will follow in §2.4.3. In (Priestley et al., 2007) the proposed equations is in the form:

$$\xi_{eq} = 0.05 + C \cdot \left(\frac{\mu - 1}{\mu\pi}\right) \qquad \textit{(Eq. 2.16)}$$

C is a factor that was calibrated by means of a large number of non-linear time-history analyses, and is related to the structural typology and material (hysteretic behaviour). The constant 0.05 represent elastic damping (ξ_{el}), expressed as damping ratio related to the critical damping, according to the value that normally is taken into account in the codes for elastic response spectra. Fig. 2.17 shows the relationship between damping and ductility expressed by (Eq. 2.16) for several hysteretic behaviour.

It is important to point out that factor C is valid only for ξ_{el} = 0.05, so if another value of ξ_{el} is assumed, a more complex equation has to be used (Eq. 2.33). This equation takes into account four coefficients, instead of one, and in addition to ductility, also the effective period (T_e) of the structure is considered, which is not appealing for design (Dwairi et al., 2007).

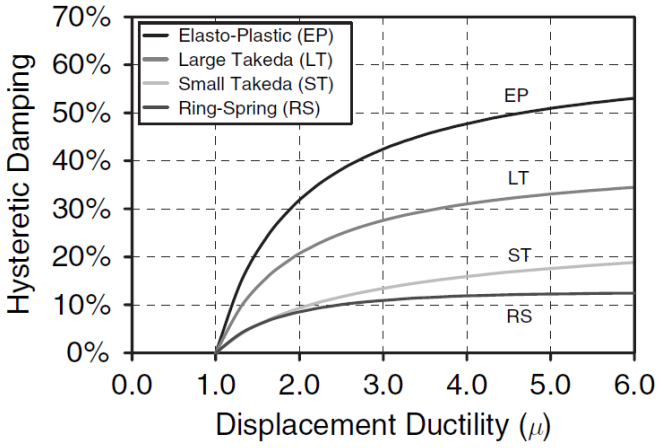

Fig. 2.17 Hysteretic damping versus ductility for several hysteretic behaviour (from Dwairi et al 2007)

3. Determination of equivalent period.

The value of ξ_{eq} is used to estimate the damping correction factor (η). This factor is defined as the ratio between actual inelastic displacement and elastic displacement spectra 5% damped. So it is used to scale displacement spectra, in order to obtain the effective period T_e corresponding to the design displacement Δ_d. The typical expression for η is given by (Eq. 2.17), that was proposed by (Bommer et al., 2000) and has be taken both in the current version of EC8 (EN 1998-1, 2004) and in Italian Technical Code (DM 14/01/2008, 2008). A similar equation (Eq. 2.18), included in the previous version of EC8, is suggested by (Priestley et al., 2007), the origin of which has not been documented (Bommer & Mendis, 2005). In both the equations, ξ is expressed as percentage.

$$\eta = \sqrt{\frac{10}{5+\xi}} \qquad \textit{(Eq. 2.17)}$$

$$\eta = \sqrt{\frac{7}{2+\xi}} \qquad \textit{(Eq. 2.18)}$$

The determination of T_e is represented in Fig. 2.18. Once the corner displacement Δ_c is scaled, the effective period can be simply found through a proportion between periods and displacements (Eq. 2.19).

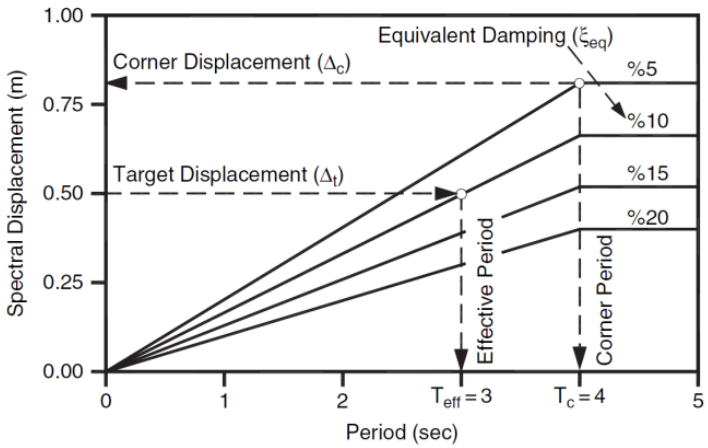

Fig. 2.18 Determination of effective period by means scaled elastic spectra (from Dwairi et al 2007).

4. Computing the design base shear force.

From effective period, the effective stiffness and base shear force V_b are calculated with (Eq. 2.20) and (Eq. 2.21), respectively. The structural elements can be now designed to provide the base shear.

$$T_e = \frac{\Delta_d}{\Delta_{c,\xi}} \cdot T_c \qquad \textit{(Eq. 2.19)}$$

$$K_e = \frac{4\pi^2 m}{T_e^2} \qquad \textit{(Eq. 2.20)}$$

$$V_b = K_e \cdot \Delta_d \qquad \textit{(Eq. 2.21)}$$

2.4.2.2 DDBD method for a MDOF system

This process can be applied also to MDOF structures. For these structures, at the beginning of the procedure, the equivalent SDOF system has to be defined (Fig. 2.19). This means to transform a system with n degrees of freedom in an equivalent SDOF system, identified by the equivalent height (H_e), mass (m_e) and design displacement Δ_d. This transformation is performed under the following assumptions (Medhekar & Kennedy, 2000):

- The MDOF system respond harmonically in the assumed shape;
- The base shear developed by the two systems is the same;

- The work done by the lateral inertial forces on both systems is the same;

The first step is to evaluate the inelastic displacement shape. This shape is related to structural typology, and simplified methods for RC frame and structural wall buildings are reported in (Priestley et al., 2007). From the inelastic displacement profile, Δ_d, m_e and H_e can be computed using (Eq. 2.22), (Eq. 2.23) and (Eq. 2.24) respectively. Once the characteristics of equivalent SDOF system are determined, it is possible to calculate Δ_y on the basis of strain and/or drift considerations, and then ductility using (Eq. 2.15). At this point, the procedure for SDOF systems, starting from step 2, can be applied.

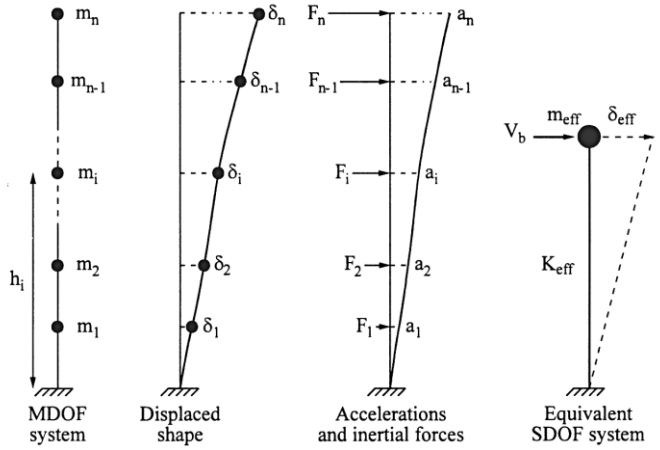

Fig. 2.19 MDOF transformation in equivalent SDOF system. (From Medhekar & Kennedy, 2000)

$$\Delta_d = \frac{\sum_{i=1}^{n} m_i \Delta_i^2}{\sum_{i=1}^{n} m_i \Delta_i} \qquad \textit{(Eq. 2.22)}$$

$$H_e = \frac{\sum_{i=1}^{n} m_i \Delta_i H_i}{\sum_{i=1}^{n} m_i \Delta_i} \qquad \textit{(Eq. 2.23)}$$

$$m_e = \frac{\sum_{i=1}^{n} m_i \Delta_i}{\Delta_d} \qquad \textit{(Eq. 2.24)}$$

At the end of the procedure, the base shear force has to be distributed to the n DOF of the system, in order to verify each structural element. On the basis of the assumption of harmonic-type response, the base shear can be distributed proportionally to the product of the mass and displacement, using (Eq. 2.25).

$$F_j = V_b \frac{m_j \Delta_j}{\sum_{i=1}^{n} (m_i \Delta_i)} \qquad \textit{(Eq. 2.25)}$$

2.4.3 Equivalent viscous damping

The concept of viscous velocity-dependent damping is generally used in structural engineering to represent nonlinear energy dissipation. This dissipation is due to various mechanisms such as cracking, interaction between structural and non-structural elements, soil-structure interaction etc… There is no physical cause to assume a linear viscous damping, but this choice has essentially two reasons. The first is that it is very difficult and unpractical to estimate each mechanism individually, whereas elastic viscous damping represents the combined effect of all mentioned dissipation mechanisms. Furthermore, the use of linear viscous damping simplifies the solutions of the differential equation of motion represented by (Eq. 2.26), where c is the damping coefficient. This equation can be re-written in function of the property of the system, obtaining (Eq. 2.27), where ω_n is the natural frequency of the system and ξ is the ratio between viscous and the critical damping coefficient.

$$m\ddot{u} + c\dot{u} + ku = 0 \qquad \textit{(Eq. 2.26)}$$

$$\ddot{u} + 2\xi\omega_n\dot{u} + \omega_n^2 u = 0 \qquad \textit{(Eq. 2.27)}$$

It is common use to consider the viscous damping as a sum of two components, the elastic and the hysteretic damping (Eq. 2.28). The elastic component of viscous damping allows taking into account further dissipative contributions, that are:

- Non-linearity in the elastic range, since the majority of hysteretic models consider the response as linear elastic at force levels less than yielding;
- Foundation damping;
- Non-structural damping;

The elastic damping is normally set to 5%. Despite the expression used in (Eq. 2.28), the two components should not be simply added. Furthermore, elastic component should be proportional to tangent stiffness, and not to initial stiffness (Priestley & Grant, 2005).

$$\xi_{eq} = \xi_{el} + \xi_{hys} \qquad \textit{(Eq. 2.28)}$$

The first attempt to make use of equivalent viscous damping in order to take into account the hysteretic damping was made by (Jacobsen, 1930). Jacobsen proposed an approximate solution of the steady-state response of a non-linear oscillator by defining an equivalent linear oscillator. The value of the equivalent viscous damping can be obtained equating the energy dissipated by the linear viscous system with the energy dissipated by the non-linear system, assuming that both of them have the same initial stiffness. This result is expressed by (Eq. 2.29), where E_{hys} is the energy dissipated in one hysteretic cycle, and F_m and u_m are the maximum force and displacement achieved.

$$\xi_{hys} = \frac{E_{hys}}{2\pi F_m u_m} \qquad \textit{(Eq. 2.29)}$$

(Rosenblueth & Herrera, 1964) proposed the first equivalent linear method in which the Jacobsen's damping was combined with secant stiffness at maximum deformation as the basis for selecting the period shift.

(Gulkan & Sozen, 1974) extended Jacobsen's approach by means of a series of dynamic tests on one-storey, one-bay RC frames. From experimental results and analytical studies they proposed that the earthquake input energy into a ductile structure is similar to that dissipated by an associated elastic system with substitute viscous damping (ξ_{sub}). They assumed that relative velocity of the associated elastic structure is the same as the ductile structure, and so, from the equality of energy, (Eq. 2.30) can be obtained. T_{sub} is the effective period related to the secant stiffness to maximum response, u is the displacement of the structure, $\ddot{u}_g$ is the ground acceleration, t is the duration of the excitation and τ is the time variable.

They also computed the same factor using the approximation by Jacobsen and found that results were not significantly different.

$$\xi_{sub} = \frac{T_{sub} \int_0^t \ddot{u}_g(\tau) \cdot \dot{u}(\tau) d\tau}{4\pi \int_0^t \dot{u}^2(\tau)\, d\tau} \qquad \textit{(Eq. 2.30)}$$

Later on, (Iwan & Gates, 1979) used results from time histories analyses of 12 recorded earthquake ground motions in order to calibrate empirical formula for period shift and equivalent damping of the equivalent linear system, expressed by (Eq. 2.31) and (Eq. 2.32) respectively. The hysteretic model used in the analyses is derived from a combination of elastic and Coulomb slip elements.

$$T_{eq} = T[1 + 0.121(\mu - 1)^{0.939}] \quad \textit{(Eq. 2.31)}$$

$$\xi_{eq} = \xi_0 + 0.0587(\mu - 1)^{0.371} \quad \textit{(Eq. 2.32)}$$

The Takeda hysteretic model was used by (Kowalsky et al., 1995) together with the secant stiffness at maximum deformation, for defining the period shift to derive an equation for equivalent viscous damping.

A comparison among those four approaches to estimate the maximum inelastic displacement demand of SDOF systems, when subjected to earthquake ground motion, can be found in (Miranda & Ruiz-García, 2002). They used elasto-plastic and stiffness-degrading models with periods between 0.5 and 3.0 s subjected to 264 ground motions recordered on a firm site in California. Miranda and García concluded that (Rosenblueth & Herrera, 1964) method (R&H) gives the highest damping values, and so it underestimates displacements. (Gulkan & Sozen, 1974), G&S, Iwan, and Kowalsky methods consider damping significantly smaller than those of R&H, and so they produce much better results. The mean relative errors increase with increasing displacement ductilities and with decreasing periods of vibration. In the short period range, G&S and Kowalsky methods tend to significantly overestimate maximum displacements, while Iwan's method underestimates maximum displacements.

(Kwan & Billington, 2003) proposed empirical relations for equivalent damping and period shift. These relations are based on optimal values obtained from the minimization of errors between the displacements of non-linear and equivalent linear systems. They considered six types of hysteretic behaviour within the period range from 0.1 to 1.5 s (each 0.1 s) and four ductility ratios (from 2 to 8).

In (Blandon & Priestley, 2005) equivalent viscous damping estimated by Jacobsen's approach was compared with effective damping factors obtained from an iterative procedure using time-history analyses of SDOF systems. They used six hysteretic models, with periods range from 0.5 to 4.0 s each 0.5 s and five ductility ratios (from 2 to 6), and six artificial records. The elastic viscous damping was set to zero, in order to directly determine the contribution of hysteretic damping. Blandon and Priestley found that, in general, Jacobsen's approach overestimates the value

of equivalent viscous damping. Based on analytical results, a series of design equations as a function of hysteresis rule, displacement ductility and period were developed (Eq. 2.33).

$$\xi_{eq} = \frac{a}{\pi}\left(1 - \frac{1}{\mu^b} - 0.1r\mu\right) \cdot \left(1 + \frac{1}{(T+c)^d}\right) \cdot \frac{1}{N} \qquad \textit{(Eq. 2.33)}$$

More recently, (Dwairi et al., 2007) performed an extensive evaluation of Jacobsen's equivalent damping approach combined with the secant stiffness method. Four hysteretic models were evaluated, with effective period range between 0.1 and 5.0 s each 0.1 s and five ductility ratios (from 1.5 to 6). The analyses were carried out using a catalogue of 100 ground motions records and tangent stiffness proportional elastic viscous damping set to 2%. The results confirmed an overestimation of the equivalent damping and consequently an underestimation of displacements for intermediate to long periods. The overestimation of damping is proportional to the amount of energy dissipated and ductility level. A large underestimation of the equivalent damping is evident for short effective periods, in particular less than 0.4 sec. New empirical equivalent damping equations as a function of hysteretic model, displacement ductility and effective period were proposed:

$$\xi_{eq} = \xi_v + C\left(\frac{\mu - 1}{\mu\pi}\right) \qquad \begin{array}{ll} C=A+B(1-T_{eff}) & T_{eff} < 1\ s \\ C=A & T_{eff} \geq 1\ s \end{array} \qquad \textit{(Eq. 2.34)}$$

This equation can be simplified considering that it is conservative to use low estimates of damping, and also that very often regular structures such as frame and wall buildings and bridges have effective periods greater than 1.0 s. Furthermore, for all the hysteretic behaviours, excluding the elasto-plastic model, the period dependency was found insignificant. Hence it can be considered adequate, and also conservative, to ignore the period dependency in design (Priestley et al., 2007). In such a way, the simplified formula express by (Eq. 2.16) is obtained.

2.5 DDBD Method for Masonry Buildings

This section is mainly derived from (Priestley et al., 2007). Masonry structures are often considered to be inadequate to resist seismic action. Considering the problem from a displacement capacity point of view, it is true that masonry elements

attain specific performances levels in terms of sustained damage at lower interstorey drifts when compared with other construction type. On the other hand, it has been noted that fundamentals periods of masonry buildings are also naturally lower than those of other structural types, and consequently the displacement demand is also comparatively smaller (Priestley et al., 2007).

Masonry structures have particular characteristics that allow to make some considerations:

- Very often, in seismic regions, masonry buildings are regular in their configuration plan. This, together with high redundant restrain system typical for this structural type, implies a rather low sensitivity to torsional problems;
- Due to the limited displacement capacity, second order effects are also scarcely relevant.
- Masonry buildings are in general simple, small structures and it is reasonable to consider simplified approaches.

It is assumed that displacement profile can be considered linear with height. Hence, assuming that floor masses and storey height are the same at each storey, the ratio of effective height to total height can be expressed by (Eq. 2.35), and so the effective height can be calculated from the number of storeys. Since the typical limited number of storeys, it can be considered the effective height as 0.8 times the total height. The equivalent mass can be taken as 0.9 times the total mass.

$$\frac{H_e}{H_n} = \frac{[\sum_{i=1}^{n}(m_i \Delta_i H_i)/\sum_{i=1}^{n}(m_i \Delta_i)]}{H_n} = \frac{(\sum_{i=1}^{n} i^2/\sum_{i=1}^{n} i)}{n} \qquad \textit{(Eq. 2.35)}$$

The definition of design displacement Δ_d, and so equivalent damping through ductility, is usually related to the assumption of drift limits. For what concern URM, in (Magenes & Calvi, 1997) these quantities are indicated in function of the failure mode, from an experimental and analytical study. The authors suggest an ultimate drift of 0.5% and 1.0%, and an equivalent damping equal to 10% and 15%, for shear and flexural failure respectively. In (Priestley et al., 2007) these drift limits are reduced of 20%, i.e. 0.4% for shear and 0.8% for flexural failure. These are also the limit imposed by Italian Technical Code. The equivalent viscous damping instead is assumed to be 15% for shear and 10% for flexural failure behaviour. Further indications can be found in (Calvi & Sullivan, 2009b), where bi-linear function related to ductility are proposed (Eq. 2.36) (Eq. 2.37) (Eq. 2.38) (Eq. 2.39). The first two are related to shear sliding failure, whereas the third and the fourth are related to diagonal cracking shear failure, ξ_0 can be taken as 0.02.

$$\xi_{eq} = 0.35\xi_0 + 0.11(\mu - 1) \quad \text{for } 1.0 \leq \mu < 2.5 \quad \textit{(Eq. 2.36)}$$

$$\xi_{eq} = 0.35\xi_0 + 0.165 \quad \text{for } \mu \geq 2.5 \quad \textit{(Eq. 2.37)}$$

$$\xi_{eq} = 0.35\xi_0 + 0.07(\mu - 1) \quad \text{for } 1.0 \leq \mu < 4.0 \quad \textit{(Eq. 2.38)}$$

$$\xi_{eq} = 0.35\xi_0 + 0.21 \quad \text{for } \mu \geq 4.0 \quad \textit{(Eq. 2.39)}$$

More recently, (Ahmad et al., 2010), on the basis of experimental data, have calibrated the coefficient C of equation (Eq. 2.16) for masonry walls. The definition of yield displacement used, based on idealized bi-linearization, implies ductility values less than one at lower displacements. These values are not been taken into account. By means a regression analysis the value of 0.32 for C has been obtained.

For RM, instead, there are not many references. The greater difference compared to URM is the possibility to apply capacity design principles. Indeed, it is possible to vary flexural and shear strength by changing vertical and horizontal reinforcement ratio. So shear failure has to be avoided, preferring flexural failure. Following a methodology similar to that proposed for RC walls, it is possible to compute the yield and ultimate drifts, and so ductility. In NTC 2008 it is proposed to consider 1.5 times the limits for URM, i.e. 0.6% for shear and 1.2% for flexural failure. Another possibility is to use analytical non-linear methods, even if simplified, as proposed by (Guidi, 2011; Guidi & da Porto, 2011).

The equivalent viscous damping can be computed using (Eq. 2.16), with the value of constant C=0.444. It should be pointed out that this coefficient C has been obtained using “small Takeda” model, which is mainly used for concrete wall buildings and bridges. Since typical values of ductility obtained with the methodology proposed in (Priestley et al., 2007) are around 2, an equivalent viscous damping of 10% is suggested. The design drift can be taken equal to that for flexure in URM, i.e. 0.8%. For RM structures it is also possible to design the coupling degree (β_{CB}) between structural walls and RC slabs in analogy with RC coupled walls structures. β_{CB} is defined by (Eq. 2.40).

$$\beta_{CB} = M_{CB}/M_{OTM} \quad \textit{(Eq. 2.40)}$$

M_{CB} is the total moment resulting at the base due to the presence of coupling beams, M_{OTM} is the total overturning moment, i.e. the sum between M_{CB} and the moment capacity of the walls. In this context, it is unfeasible treating such issue in a comprehensive manner, but a detailed description can be found in (Paulay & Priestley, 1992) and (Priestley et al., 2007). It should be considered that considering a coupling action, allows estimating the global system equivalent damping by means (Eq. 2.41). ξ_w and ξ_{CB} are the damping associated with wall and coupling beam action.

$$\xi_{sys} = (1 - \beta_{CB}) \cdot \xi_w + \beta_{CB} \cdot \xi_{CB} \qquad \textit{(Eq. 2.41)}$$

From this brief review it is easy to noticed that there are no many contributions on DDBD method for masonry structures. Despite it is reasonable to consider simplified procedure for this type of constructions, the number of approximations, such as the identification of equivalent SDOF system, drift limits at ULS, equivalent damping, make the application of DDBD principles very difficult.

2.6 Conclusions

As can be seen from the literature survey presented in this chapter, many issues regarding the seismic behaviour of masonry structures are still open. In particular the application of DDBD method suffers from same shortcomings. These are related to:

- Drift limits proposed in the codes, and also in Priestley, are usually derived from experimental results, and are related to the observed failure mode. Since the great variety of masonry types, it is unreliable to consider drift limits related only to failure mode. Furthermore, as showed in (Guidi, 2011; Guidi & da Porto, 2011), these limits seem to be too conservative. Guidi has demonstrated that the displacement capacity, not only related to ultimate capacity but also to evolution of damage, is strongly affected by the characteristics of masonry wall (mainly compressive strength and aspect ratio) and vertical load.
- For URM, the equivalent viscous damping can be derived from experimental results. In this case it is related to failure mode and considered constant and independent from displacement demand. The formulations provided in (Calvi & Sullivan, 2009b) are instead linear with displacement ductility. It is evident that this incoherency has to be further studied. Furthermore, in (Calvi &

Sullivan, 2009b) there is not a clear explanation of how the yielding of masonry can be computed. This lack, together with the absence of indications on ductility level associated to specific damage levels, i.e. limit states, makes impossible to apply the proposed damping relations.

- For what concern RM, Priestley consider the same ultimate drift and equivalent damping of those considered for URM failing in flexure. This strong approximation is not demonstrated by specific studies. Furthermore the suggested methodology for defining the yielding and ultimate displacements leads to results not so consistent with those derived from experimentations, such as (DISWall, 2008).
- Regarding the application of method to MDOF systems, the assumption of linear displacement profile has not been demonstrated in a rigorous manner. Furthermore, considering a schematization of real structure with one degree of freedom for each storey, the lumped mass at each degree of freedom should take into account of both the floor and walls. This means that masses of first and last degree of freedom could be differ from those of others degrees of freedom. Since the limited total number of storeys, the hypothesis of that floor masses are the same at each storey is unrealistic.
- From the previous observation, it arises that the simplified procedure described in §2.5, more precisely, the assumption that equivalent height and mass can be taken respectively 0.8 times the total height and 0.9 times the total mass, can leads to significant errors in determination of equivalent SDOF system.

3 EXPERIMENTAL DATA AND RESULTS

3.1 Introduction

The main aim of this chapter is to present the results of several experimental campaigns carried out at University of Padova in the last years. Tests were performed to determine the behaviour under in-plane combined vertical and horizontal actions, hence the seismic performance, of different masonry walls types. In this work, the relevant masonry types are a new system of reinforced masonry and historical stone masonry strengthened with hydraulic lime based grout injection.

3.2 Reinforced Masonry: Experimental Work and Results

The studied reinforced masonry system is based on the use of concentrated vertical reinforcement, similar to confined masonry. It is an innovative system, recently developed in the framework of European Project (DISWall, 2008), that utilized special clay units (Fig. 3.1). Horizontally perforated units with frogs for laying horizontal reinforcement and vertical perforated units for confining columns are used.

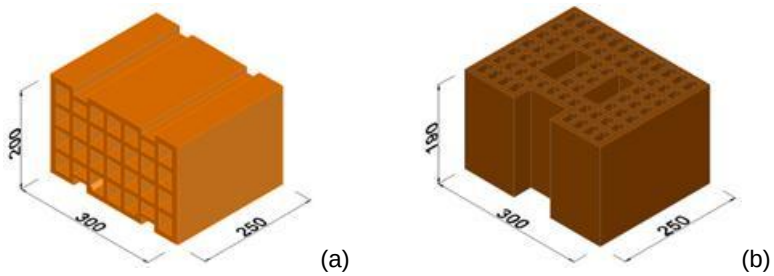

(a) (b)

Fig. 3.1 Details of (a) horizontally perforated unit (b) vertically perforated unit

Vertical reinforcement in the columns is composed of steel bars, whereas horizontal reinforcement may be made of either steel bars or prefabricated steel trusses (Fig. 3.2). A special mortar was developed for this reinforced masonry

system, especially for what concern the properties of consistence, plasticity, and workability, to allow for a proper bed joint and recess filling and also for a proper filling of the reinforced vertical cavities.

The main advantages of this system are related to durability and construction issues: placing the horizontal reinforcement into recesses filled with mortar improves reinforcement durability, makes the reinforcement positioning more precise and easier, allows producing good bond between mortar and units, and mortar and reinforcement. In addition, using units with horizontal holes helps fulfilling internal environment comfort conditions: this technique is traditionally adopted in the Mediterranean countries to improve thermal insulation. Units with horizontal holes could also benefit acoustic insulation, provided that head joints are covered with mortar, as it actually is.

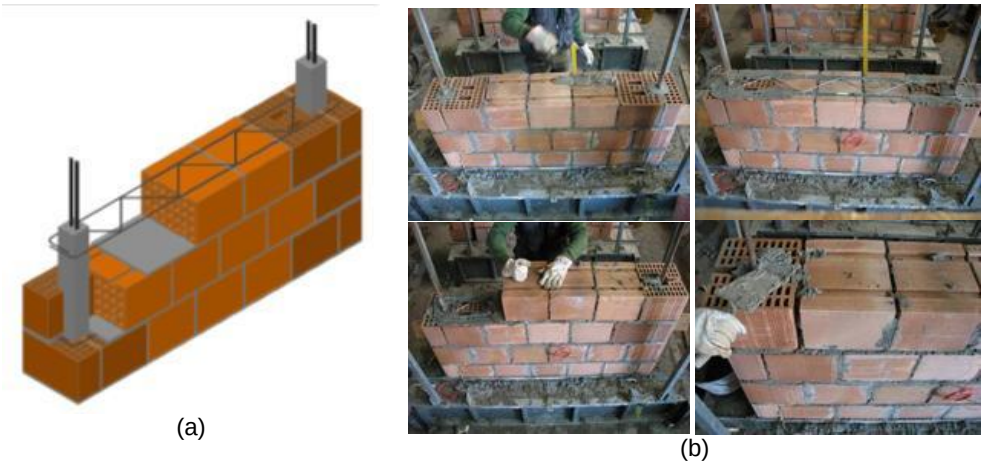

(a) (b)

Fig. 3.2 (a) Reinforced masonry system and (b) construction phases.

As regards mechanical behaviour, this system is conceived to perform as reinforced masonry, provided that units with horizontal holes are effective in transferring horizontal loads to the lateral confining columns and they do not present fragile behaviour. The main aim of the experimental program was to assess the system behaviour under seismic actions, by means of shear-compression cyclic tests. Instead, the effectiveness of horizontally perforated units in transferring horizontal loads to lateral confining columns may be reduced by unit brittleness and/or malfunctioning of the composite system at the interface between central masonry panels and confining columns. Hence, the basic properties of the constitutive materials (units, mortar and reinforcement) and the behaviour of the reinforced masonry system in compression have been extensively investigated (Mosele, 2009).

Cyclic shear compression tests were carried out on fourteen full-scale specimens, differentiated by: presence or absence of vertical reinforced confining columns, use of steel bars or prefabricated trusses as horizontal reinforcement, aspect ratio (height to length ratio) of tested specimens, and value of applied axial compression loads. The tests characterized the mechanical behaviour of the proposed construction system and allowed evaluation of the influence of these aspects on the main parameters (strength, ductility, energy dissipation, viscous damping, stiffness degradation) influencing the seismic behaviour of reinforced masonry walls.

3.2.1 Basic Material Characterization

The geometry of units, physical properties of mortar, and composition of both units and mortar were especially developed for the new reinforced masonry system. The horizontally perforated units were developed to optimize the behaviour under in-plane actions, following the concept of robustness mentioned in (EN 1998-1, 2004) and in (Tomaževič et al., 2006) and (da Porto et al., 2010a). The unit webs and shells were rectilinear and continuous, and the hole percentage was less than 45%, according to Italian seismic requirements (DM 14/01/2008, 2008). The horizontally perforated units contained 20% of tuff. Their mean compressive strength in the direction of vertical loads (f_{bm}) was 9.26 N/mm^2 and in the orthogonal direction to vertical loads, in the plane of the wall (f_{bhm}), it was 13.24 N/mm^2.

The main objective of mortar development was to use a single product, suitable for laying the horizontally perforated units and filling the vertical reinforced cavities. Mortar requirements were: compressive strength higher than 10 N/mm^2, as recommended by (EN 1998-1, 2004) and (DM 14/01/2008, 2008); balanced consistence, plasticity, and workability for bed and head joints and vertical cavities; good adhesion to units and reinforcement. The mean flexural ($f_{m,t}$) and compressive (f_m) strengths of the final product after 28 days' curing were 4.27 N/mm^2 and 14.07 N/mm^2.

The horizontal reinforcement was made of B450C hot-rolled steel with yielding stress (f_y) of 500 N/mm^2 and elastic modulus of 204.4 kN/mm^2; the truss reinforcement had yielding stress of 486 N/mm^2 and elastic modulus of 203.7 kN/mm^2. The vertical reinforcement was made of B450 cold-drawn steel, with yielding stress of 501 N/mm^2 and elastic modulus of 189 kN/mm^2.

The detailed description of the basic mechanical tests is reported elsewhere ((da Porto et al., 2010b);(Mosele et al., 2008)).

3.2.2 Uniaxial Compression Tests

To better understand the in-plane behaviour under cyclic horizontal loads, uniaxial compression tests on specimens of the entire system and on its single components (i.e., confining columns and masonry panels without confining columns) were carried out. The mean compressive strength (f_c) of masonry panels without confining columns and of the whole masonry systems was 2.71 N/mm^2 and 3.90 N/mm^2, respectively. Horizontally perforated units did undergo spalling, but they did not cause anticipated masonry failure. The frogs on the unit bed faces not only made reinforcement positioning faster and more precise, but also allowed very good bond between mortar and reinforcement to be created. The complete results of this preliminary characterisation, including experimental and numerical analyses, are reported in (Mosele, 2009) and (da Porto et al., 2010b).

3.2.3 In Plane Cyclic Tests

The specimens were tested with a cantilever-type boundary condition, with fixed base and top end free to rotate, by applying centered and constant vertical loads of 11% and 16% of the measured maximum compressive strength of the reinforced masonry walls, corresponding to 15% and 22% of the measured maximum compressive strength of the walls without confining columns. The corresponding compressive stress levels (0.4 and 0.6 N/mm^2) are adequate to represent typical vertical loads for buildings from two to four storeys in height. Two specimens, one for each pre-compression level, constitute each series listed in Table 3.1.

Name	Dimension (mm)	Horizontal Reinf.	ρ_w (%)	Vertical Reinf.	ρ_l (%)	N° of tests
HS	1550x300x1690	-	-	-	-	2
SRHS	1550x300x1690	Rebar	0.045	-	-	2
TRHS	1550x300x1690	Truss	0.040	-	-	2
SRSa	1550x300x1690	Rebar	0.045	4Φ16	0.173	2
TRSa	1550x300x1690	Truss	0.040	4Φ16	0.173	2
SRSb	1030x300x1690	Rebar	0.045	2Φ16	0.130	2
TRSb	1030x300x1690	Truss	0.040	2Φ16	0.130	2

Table 3.1 Specimens details for shear compression tests

Specimens were instrumented with 24 potentiometric displacement transducers to measure displacements, wall flexural and shear deformations, base uplift and

relative sliding between wall and footing. Four strain-gauges were used to measure strains in both vertical and horizontal reinforcement bars at characteristic sections of the wall. Lateral and vertical loads were measured by means of load cells with the three hydraulic actuators used. The lateral displacement at the top of the wall was measured by a magnetostrictive displacement transducer, which was also used for retro-activation of the actuators. Fig. 3.3 shows the instrumental scheme.

Horizontal cyclic displacements, of increasing amplitude and with peaks repeated three times for each displacement amplitude, were applied at a frequency of 0.004 Hz. Fig. 3.4 shows a view of the test set-up. Further details on tests setup, instrumentation and procedure are available in (Mosele, 2009).

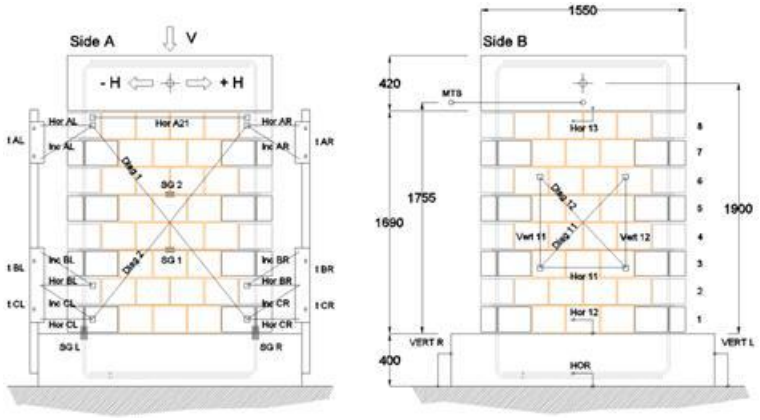

Fig. 3.3 Scheme of instruments for shear compression tests.

Fig. 3.4 Shear compression test set-up

During experimental tests, the attainment of four limit states, which can be used to idealize the behaviour of the masonry wall, were observed. These limit states correspond to changes in how the specimens resist the progressive increment of applied lateral displacement. This idealization, purposely developed for plain masonry (Abrams, 2001), was adapted to our reinforced masonry wall specimens.

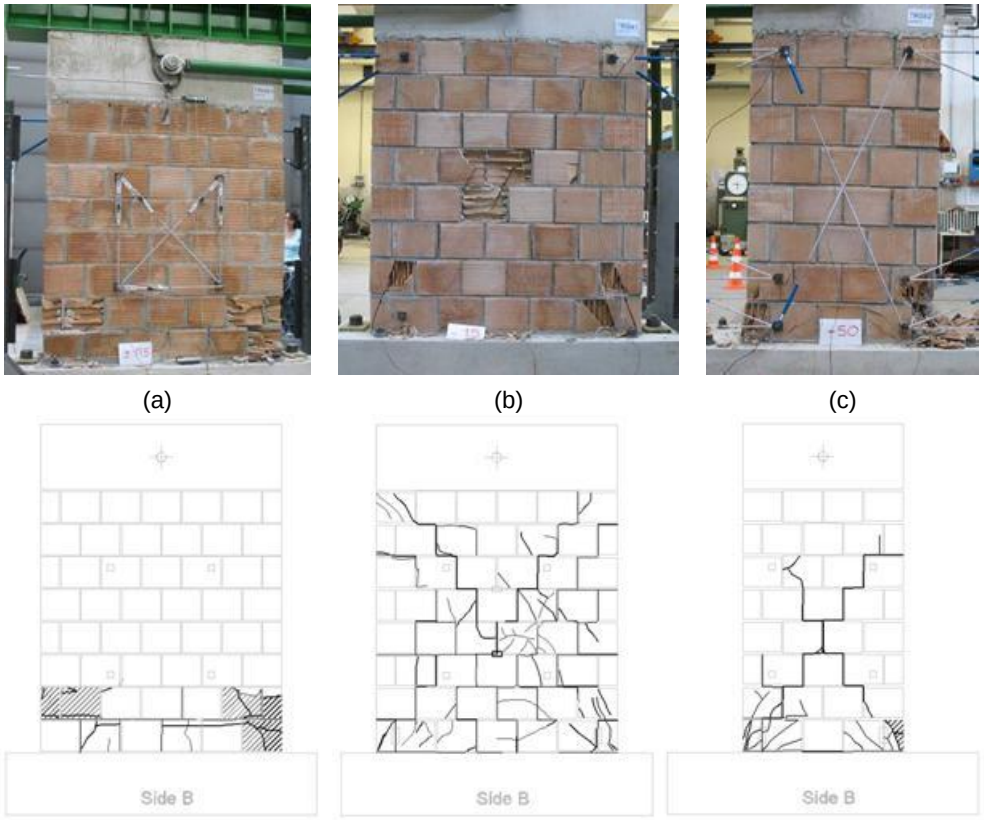

Fig. 3.5 Crack patterns at ultimate displacement in TRHS (a), TRSa (b) and TRSb (c) under compressive stresses of 0.6 N/mm^2.

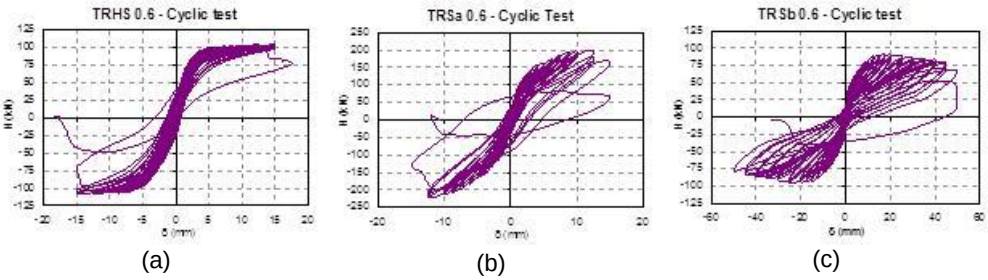

Fig. 3.6 Load displacement diagrams of (a) TRHS 0.6, (b) TRSa 0.6 and (c) TRSb 0.6.

Fig. 3.5 shows three specimens (TRHS, TRSa and TRSb) tested under compressive stresses of 0.6 N/mm^2, Fig. 3.6 shows the corresponding load-displacement diagrams, and Fig. 3.7 shows some details at failure. Fig. 3.8 compares limit states and the idealized envelope curves of all tested specimens. Lastly, Table 3.2 lists the values of lateral loads (H) and corresponding rotation angles ($\psi = \delta / H$) at the four limit states, the main load and ductility ratios, and observed failure modes.

The first non-linearity, due to the first cracks opening on the bottom bed-joints (H_f, δ_f), occurred at displacements of about 1 - 2 mm (mean rotation angle ψ = 0.075%), independently of type of specimen or applied axial load.

(a) (b) (c)

Fig. 3.7 (a) Buckling of vertical bars in TRSa 0.4; (b) tension failure of vertical bars in SRSb 0.4; (c) transverse deformation of truss at end of test in TRHS 0.6.

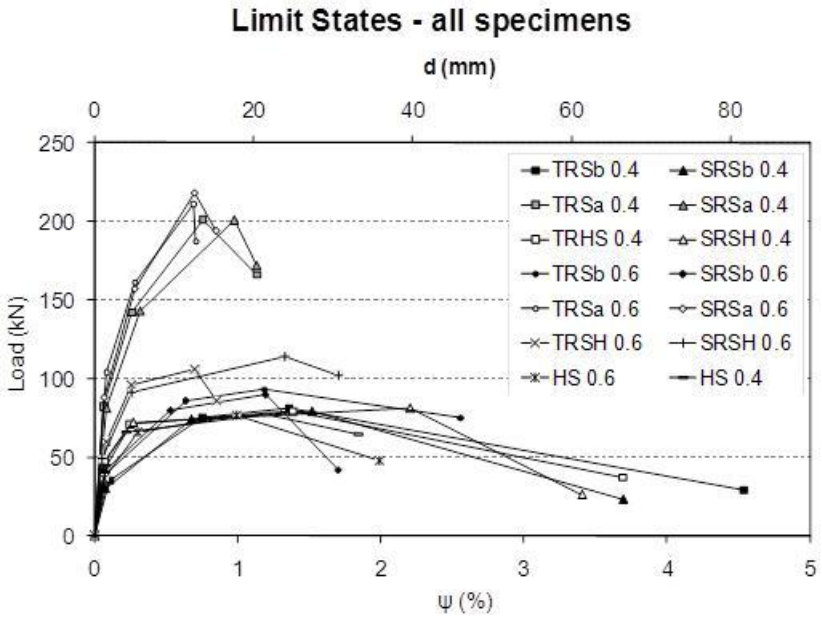

Fig. 3.8 Limit states envelop curves of masonry specimens

In slender specimens, which were characterized by flexural failure and damage concentrated at the compressed toe (Fig. 3.5c), the following crack limit state (H_{cr}, δ_{cr}) occurred when the vertical bars yielded, at displacements of 9-12 mm (ψ = 0.50-0.70%), according to axial loads and type of horizontal reinforcement.

In squat specimens, characterized by shear failure mode (Fig. 3.5b), the second non-linearity took place when the first diagonal crack opened and strains of shear reinforcement simultaneously increased. This occurred at displacements of 5 mm (ψ = 0.30%), independently of applied axial load.

Subsequently, in slender walls, loads increased gradually until maximum load (H_{max}) and the relevant displacement (δ_{Hmax}, Fig. 3.6c and Fig. 3.8) were reached. This condition represents the third limit state, and is characterized by crushing of masonry.

Specimen	H_f kN	ψ_f %	H_{cr} kN	ψ_{cr} %	H_{max} kN	ψ_{Hmax} %	H_u kN	ψ_u %	H_{cr}/H_{max}	H_u/H_{max}	ψ_{cr}/ψ_{Hmax}	ψ_u/ψ_{cr}	Failure mode
σ_0=0.6 N/mm²													
HS 06	36	0.07	66	0.31	77	0.99	48	1.99	0.86	0.63	0.31	6.42	R
TRHS 06	60	0.09	96	0.26	106	0.70	86	0.85	0.91	0.81	0.36	3.33	R
SRHS 06	49	0.06	91	0.26	114	1.33	102	1.71	0.80	0.89	0.20	6.58	R
TRSa 06	104	0.09	169	0.31	207	0.73	166	0.86	0.82	0.80	0.42	2.77	S
SRSa 06	88	0.06	159	0.31	217	0.74	182	1.04	0.73	0.84	0.41	3.41	S
TRSb 06	40	0.09	86	0.68	93	1.28	81	2.71	0.92	0.88	0.53	4.00	F
SRSb 06	41	0.08	80	0.53	89	1.20	70	1.81	0.90	0.79	0.44	3.42	F
σ_0=0.4 N/mm²													
HS 04	45	0.08	66	0.22	77	1.20	65	1.85	0.86	0.84	0.18	8.41	R
TRHS 04	47	0.07	71	0.25	79	1.39	37	3.69	0.90	0.47	0.18	14.76	R
SRHS 04	45	0.06	72	0.27	81	2.21	26	3.41	0.89	0.32	0.12	12.63	R
TRSa 04	82	0.07	144	0.30	199	0.70	160	1.25	0.72	0.80	0.44	4.13	S/F*
SRSa 04	81	0.09	137	0.30	200	1.04	149	1.45	0.68	0.75	0.29	4.80	S/F*
TRSb 04	32	0.10	74	0.73	79	1.18	68	3.29	0.94	0.87	0.62	4.53	F
SRSb 04	30	0.08	67	0.53	78	1.46	70	2.70	0.86	0.90	0.36	5.07	F

R = rocking, F = flexure, S = shear, S/F = combined shear/flexure mechanism

Table 3.2. Results of shear compression tests.

Conversely, squat specimens reached this state with consistently increased loads (Fig. 3.6b and Fig. 3.8) with the formation of a diagonal strut, defined by cracks which crossed units and mortar joints. Spalling of units was also observed

(Fig. 3.5b). At the lower axial load level, damage of the compressed toes due to buckling of vertical bars also occurred (Fig. 3.7a).

This phenomenon took squat specimens to the ultimate limit state with high strength degradation (10-15%) and low displacement capacity (12-20 mm, corresponding to ψ = 0.70-1.14%, according to axial compression load). This ultimate limit state corresponded to the values of displacements δ_u (and loads H_u), at which the specimens still showed stable behaviour, before reaching maximum experimental displacement and collapse. Slender walls had high displacement capacity (30-60 mm, ψ = 1.70-3.70%) and hence ductile behaviour, due to flexural failure mode, which occurred with fracture of vertical bars, according to axial load (Fig. 3.7b). In walls without vertical reinforcement, high values of ultimate displacements were due to rocking, and damage was concentrated at the bottom of the specimen (Fig. 3.5a and Fig. 3.7c).

The values of rotation angles at the ultimate limit state were weighed against those proposed by the Italian standard (DM 14/01/2008, 2008) for non-linear static analysis of reinforced masonry buildings. 1.2% assumed for flexural behaviour and 0.6% assumed for shear behaviour are moderately conservative, compared with the experimental values.

Lastly, the seismic response of buildings is related not only to strength and displacement capacity, i.e., ductility, of the structural members, but also to typical parameters of cyclic behaviour, such as energy dissipation capacity, stiffness degradation and viscous damping coefficient, according to damage propagation. The energy dissipation capacity of our reinforced masonry system was lower than that usually reported for reinforced masonry walls ((Tomaževič et al., 1996), (Magenes et al., 1996), (Bernardini et al., 1997)). The ratio between dissipated and input energy of the complete reinforced masonry system ranges between 20% and 40% (Fig. 3.9). In any case, these values are still higher than those generally given for unreinforced masonry ((da Porto et al., 2009), (Magenes & Calvi, 1997)). The trend of the viscous damping coefficient is generally similar to that of energy dissipation capacity (Fig. 3.10). The viscous damping coefficient was about 5%, and tended to increase in the post-peak phase in reinforced masonry walls (TRS and SRS), whereas it remained constant for specimens without vertical reinforcement (HS series). A complete summary of experimental results can be found in (da Porto et al., 2011)

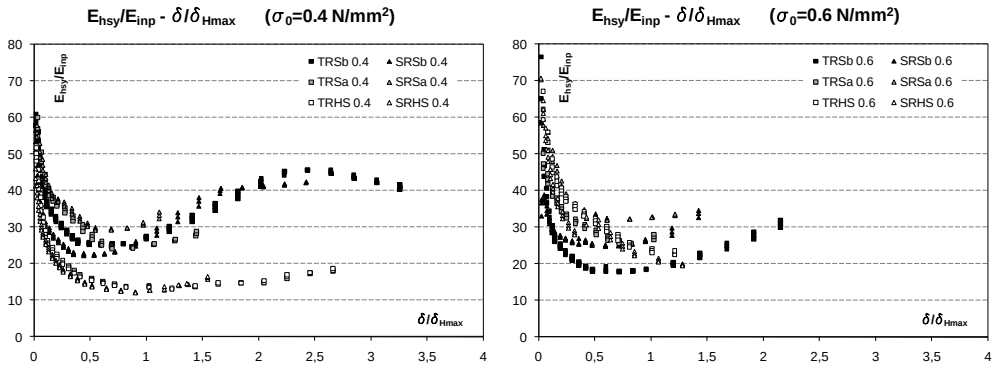

Fig. 3.9. Ratio of dissipated/input energy vs normalized displacement. Specimens under (a) 0.4N/mm^2 and (b) 0.6N/mm^2.

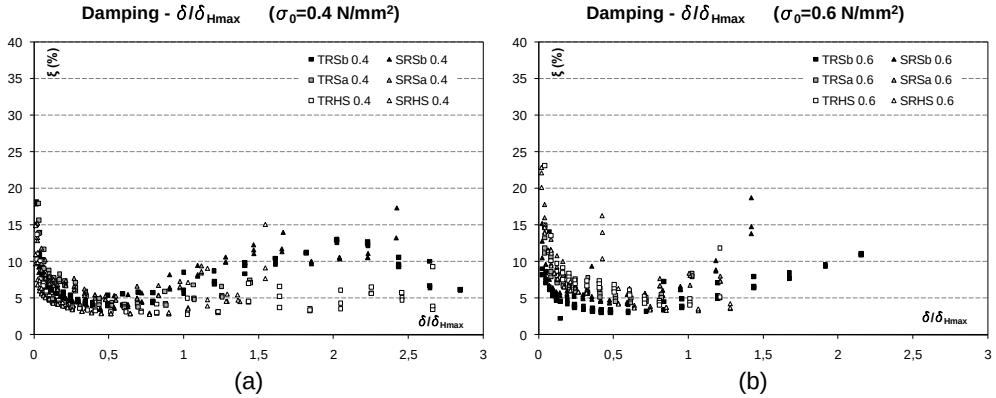

Fig. 3.10. Viscous damping coefficient vs normalized displacement. Specimens under (a) 0.4N/mm^2 and (b) 0.6N/mm^2.

3.3 Stone Masonry: Experimental Work and Results

The historical stone masonry type studied is multi-leaf, which was a building technique widely employed for common historical constructions, not only in Italy but also in other European countries. Over the years, the special features and failure mechanisms of three-leaf masonries have been examined in depth (Tomaževič & Apih, 1993; Toumbakari & van Gemert, 1997; Vintzileou & Miltiadou-Fezans, 2008). First, this structural system is mainly characterized by a wide presence of voids in the inner core of the wall which is constituted by stone fragments. Second, transversal connections between opposite external layers are normally not provided. These aspects make the masonry especially prone to brittle mechanisms

of failure, such as detachment of external layers and out-of-plane collapse. These mechanisms are mainly caused by both compressive stresses, due to dead-loads, and horizontal actions, namely in-plane and out-of-plane forces, due to seismic loads.

For is type of masonry, the effects of hydraulic lime-based grout injection have been considered. This strengthening technique aims at limiting all the previously described failure mechanisms, which are typical for this type of masonry, assessing at the same time the compatibility among materials (Valluzzi et al., 2004). The first part of the whole experimental program involved shaking table tests on building models under different conditions. Unreinforced, strengthened and repaired structures were subjected to several seismic loads at the ENEA Research Centre ("la Casaccia") in Rome. The second part of the experimental program focused on quasi-static tests on masonry panels. This experimental section was performed at the Laboratory of Materials and Structures of Department of the Structural and Transportation Engineering of the University of Padua. Several undamaged panels could be recovered during the dismantling of building models subjected to seismic actions. Part of these specimens were tested under monotonic compression, while shear compression tests were performed on the remaining samples.

In the following sections a brief summary of uniaxial compression and shear compression tests results are presented, a complete description of work is reported in (Mazzon, 2010).

3.3.1 Uniaxial Compression Tests

Compression tests were carried out under displacement control with a Universal Amsler machine. This also allowed the post-peak branch of the load-displacement relationship to be investigated. The tested specimens can be divided in two typologies: "S" elements were strengthened, starting from undamaged conditions, whilst "R" piers were repaired by injection, being cracked and damaged. The aim of this experimental campaign was to investigate the variation in mechanical parameters, such as compressive strength, Young's modulus and the Poisson ratio.

Differences in the overall behaviour of the Strengthened and Repaired specimens, observed during the experiments, were confirmed from analyses of the stress-strain relationships. Both the vertical and horizontal strains are approximately linear up to 50% of the maximum attained vertical load on "R" samples. Over this stress level, horizontal deformation widely increased, due to opening of vertical cracks in the specimen. Strengthened specimens manifest a vertical linear deformation almost up to the attainment of compressive strength. Instead,

horizontal strains start to widely increase already at 30% of compressive strength. Beyond the attainment of maximum compressive strength, the samples of “S” series are able to sustain larger deformations. This reflect a gradual decrease in stress, followed by a noticeable increase in both vertical and horizontal deformations. Thus, differences between strengthened and repaired elements are more evident in the post-peak behaviour, while during the first phase, up to the compressive strength, they are limited.

The tests results are reported in Table 3.3.The difference in mean strength between the two series is lower than 1 N/mm^2. In fact, the maximum allowable stress on strengthened samples was 6.88 N/mm^2, while repaired specimens settled at 7.72 N/mm^2. However, as a general result also the mean value of 7.4 N/mm^2 can be considered as representative of this kind of masonry.

Specimen	σ_{max} (N/mm^2)		$\sigma_{I,cr}$ (N/mm^2)		$\sigma_{I,cr}$ (%)	
	R	S	R	S	R	S
3	7.05	7.31	1.47	3.15	20.9%	43.1%
6		7.87		2.39		30.3%
7	8.45	9.63	2.11	2.19	25.0%	22.8%
8		5.25		2.60		49.5%
9	5.58	7.59	1.22	2.18	21.8%	28.7%
10	7.29	8.14	0.90	2.71	12.4%	33.2%
11	6.01	8.24	1.68	2.84	28.0%	34.5%
average	6.88	7.72	1.48	2.21	21.6%	32.1%

Table 3.3. Compression strength of specimens and stress level corresponding to the first crack appearance

3.3.2 In Plane Cyclic Tests

The test set-up and instrumentation was similar to that already described in §3.2.3 The specimens were positioned in the test rig and a vertical pre-load was initially applied. After this preliminary phase, the horizontal displacement history was applied. The level of vertical stress, kept constant during the whole test, may reasonably range between 15% and 30% of the compressive strength of specimens, as suggested by some authors (Bosiljkov et al., 2004; Tomaževič, 2000). Hence, the applied stress levels were 1 N/mm^2 and 2 N/mm^2. These rather high loads are justified by the aim to investigate the influence of grout injection on the shear strength of multi-leaf masonries. Therefore, applying a higher stress level

will force the shear failure mechanism also on slender specimens, in which the rocking or flexural behaviour is more probable if the vertical stress is low.

Specimens are characterized by two different slenderness ratios, approximately equal to 1.0 and 1.5. Furthermore, during the preliminary phase of shear compression tests, consisting of the application of a vertical load to achieve the chosen precompression level, it was possible to evaluate the elastic properties of each panel. The results are summarized in Table 3.4.

Specimen	σ'_0 (N/mm^2)	Thickness (mm)	Width (mm)	Height (mm)	Slenderness -	E (N/mm^2)
R2	1.0	320	1463	1221	0.8	4057
S2	2.0	325	1453	1370	0.9	2738
Specimen	σ'_0 (N/mm^2)	Thickness (mm)	Width (mm)	Height (mm)	Slenderness -	E (N/mm^2)
R4	1.0	320	913	1236	1.4	5513
S4	1.0	331	923	1275	1.4	6708
R5	2.0	321	930	1381	1.5	4640
S5	2.0	328	929*	1381	1.5	4323

Table 3.4. Pre-compression levels applied during shear compression tests, geometric properties and computed elastic modulus.

The specimens exhibited different overall behaviours during the execution of tests even if, on the other hand, similarities linked all the experiments. For instance, specimens with the same slenderness ratio and stress level showed comparable overall behaviours. Four different phases could be identified for each panel, depending on the ratio between the height and the width of sample and the applied vertical load.

The first phase was related to the opening of the first cracks. This phenomenon occurred on all specimens at a displacement level ranging between 1 mm and 2 mm (ψ = 0.05–0.10%), independently of both the pre-load applied and the slenderness of the element. These cracks appeared horizontally on the first or second mortar bed joint at about 10 cm or 15 cm from the bottom of the specimen.

After the opening of these cracks, the overall behaviour was different, according to the different typology of specimen. Both squat specimens and the slender specimens with higher vertical stress, exhibited the beginning of diagonal oriented cracks due to shear mechanisms. Instead, slender specimens with a lower axial load, S4 and R4 samples, showed a crack pattern due to a rocking mechanism (Fig. 3.11b), highlighting sub-vertical cracks in the compressed toe because of bending.

The previously described mechanisms developed on specimens up to the attainment of maximum lateral resistance (H_{max}, δ_{Hmax}), when an overall degradation could be identified. The final phase was characterized by the achievement of maximum horizontal displacement at which masonry panels completely failed ($H_{\delta max}$, δ_{max}). The majority of specimens exhibited a brittle collapse, anticipated by the pulling out of central parts of lateral edges.

Fig. 3.11 shows the three strengthened specimens at ultimate displacement, Fig. 3.12 shows the corresponding load-displacement diagrams. Cracks in stones (Fig. 3.13a) occurred earlier on slender specimens with a higher vertical load than on other samples, even if on all panels this damage was clearly evident. Moreover, both slender specimens tested under low vertical stress exhibited the same overall behaviour before failure. First, as above described, a rocking mechanism cracked the wall horizontally at about 15 cm from the bottom of the panel. When this crack involved the whole width of samples and beyond the attainment of lateral resistance, the part above the breaking line became squat. Immediately after this, due to a shear mechanism, a deep diagonal crack suddenly appeared and, shortly afterwards, led to its collapse.

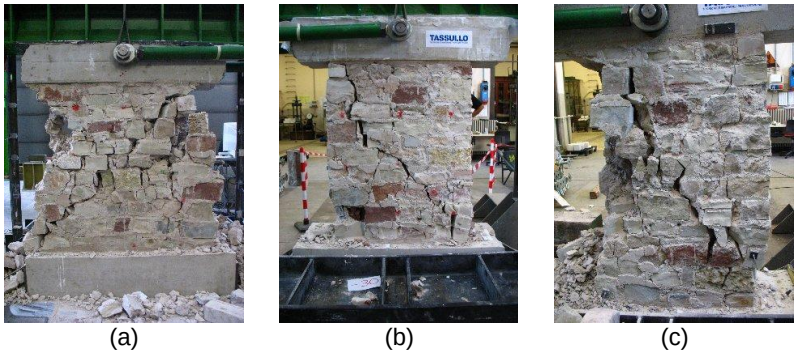

(a) (b) (c)

Fig. 3.11 Crack patterns at ultimate displacement in (a) R2, (b) R4 and (c) R5.

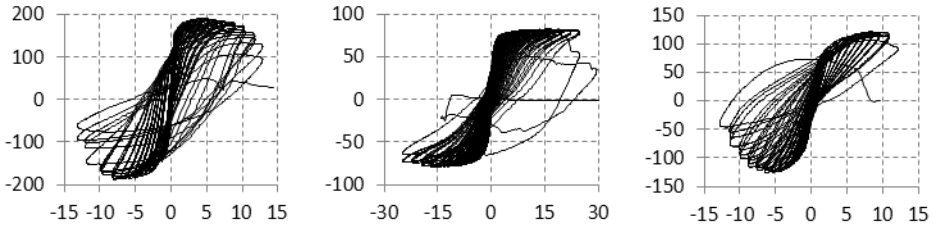

(a) (b) (c)

Fig. 3.12 Load displacement diagrams of (a) R2, (b) R4 and (c) R5.

Furthermore, each specimen exhibited the beginning and the development of its characteristic failure mode but, when the damage was widely diffused and the panel was close to failure, sub-vertical cracks appeared (Fig. 3.13b). Therefore, over the attainment of lateral resistance, the effects of compression became noticeable. This caused the opening of cracks in transversal sides, due to the buckling of external layers of masonry (Fig. 3.14), as already observed during compression tests.

Specimen	Cracking limit			Maximum resistance			Maximum displacement		
	H_{cr}	δ_{cr}	ψ_{cr}	H_{max}	δ_{Hmax}	ψ_{Hmax}	$H_{\delta max}$	δ_{max}	$\psi_{\delta max}$
	kN	mm	%	kN	mm	%	kN	mm	%
R2	151	1.23	0.10%	187	5.09	0.42%	147	11.76	0.96%
S2	221	2.19	0.16%	256	5.08	0.37%	225	9.60	0.70%
R4	71	3.73	0.30%	80	14.59	1.18%	75	24.67	2.00%
S4	75	3.55	0.28%	88	11.33	0.89%	71	22.01	1.73%
R5	108	3.59	0.26%	124	7.36	0.53%	97	11.09	0.80%
S5	110	3.86	0.28%	122	7.13	0.52%	108	9.81	0.71%

Table 3.5. Characteristic values of horizontal force, displacement and rotation angle at identified Limit State

(a) (b)

Fig. 3.13 (a) Cracks occurring in stones and (b) the formation of sub-vertical cracks on specimen R5.

(a) (b)

Fig. 3.14 Separation of outer layers on specimens R2 (a) and S2 (b).

The ratio between dissipated and input energy (Fig. 3.15) was generally high, but it was also characterized by a wide variation. It generally decreased during the first part of the test, up to the minimum values, corresponding to the attainments of lateral resistance. Beyond this phase, the energy ratio showed a limited increase up to failure. In general the ratio ranged between 30% and 60%. The trend of equivalent viscous damping was similar to that reported for the energy ratio, and a mean value of 10% can be considered (Fig. 3.16).

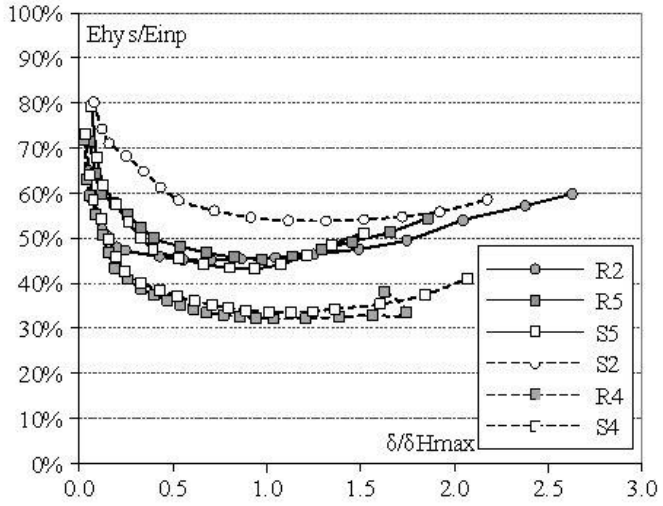

Fig. 3.15. Ratio of dissipated/input energy vs normalized displacement.

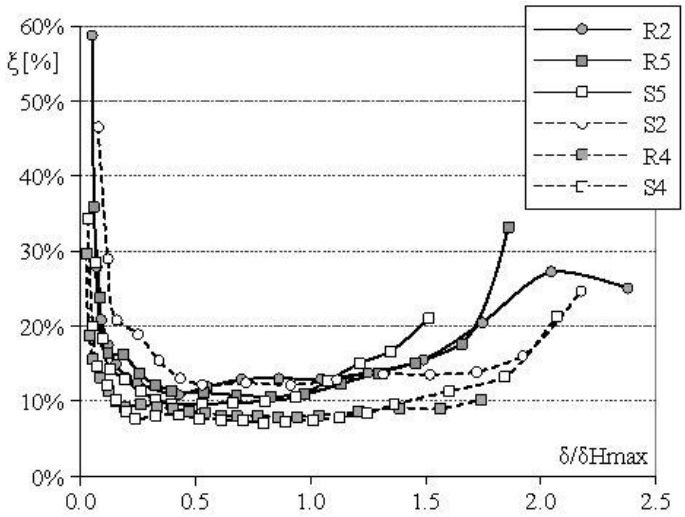

Fig. 3.16. Viscous damping coefficient vs normalized displacement.

4 DEVELOPMENT OF AN HYSTERETIC MODEL FOR DYNAMIC ANALYSES

4.1 Introduction

In this chapter the development of an hysteretic model is presented. Starting from critical analysis of existing models for in-plane loaded masonry walls and some observations on the experimental behaviour, a new model has been proposed. This model is able to reproduce the response of a masonry wall under in plane cyclic loads for both shear and flexural failure modes, and for a wide range of masonry types. Thereafter a comparison between experimental and modelled hysteretic behaviour is presented.

The model has been implemented in MATLAB environment, in order to carry out non-linear dynamic analyses. To reach this goal, also re-loading rules needed to be defined.

4.2 Application of Tomaževič model

Initially, an attempt to use the model proposed by (Tomaževič & Lutman, 1996) to model the experimental load-displacement cycles has been done. Since this model was developed for reinforced masonry, it has been applied to the studied RM system. Two specimens for comparison of experimental and analytical results have been chosen: TRSa06 and TRSb06. The first is representative of shear failure, the latter of flexural failure.

In the original model, the hysteretic loops are based on an idealized tri-linear envelope curve, determined by cracking point, maximum resistance and ultimate limit state of masonry wall. Since our masonry system is characterized by the attainment of four limit states, it has been chosen to use a quadri-linear curve as skeleton curve. Fig. 4.1 shows the comparison between the experimental data and the modelled hysteretic loops. It can be noticed that modelled cycles tend to be more similar to the experimental ones before the peak level. On the contrary, for amplitudes greater than maximum resistance, the model capacity to approximate

the real behaviour decreases. This happens because the model, with the exception of the first part of unloading, takes into account an unique value of stiffness.

Conversely, in the experimental loops, instead, an increase of stiffness when displacements tend to zero can be observed. In addition, for this reason the model always overestimates the input energy. The dissipated energy, instead, is generally overestimated for cycles minor than d_{CR} and greater than d_{Hmax} and underestimated between these two limit states. This means that the modelled values of ratio between dissipated and input energy have a different trend, when compared to the experimental ones, as shown in Fig. 4.2. It is easy to notice that experimental values describe a concave side up curve, whereas the modelled described a concave side down curve.

In conclusion, it can be said that the different shape of hysteresis cycles, between model and experimental, and the not very precise modelling of the energy balance, which is important for our analyses, suggested to develop a new model, based on actual observed in plane behaviour. This model is described in the following paragraphs.

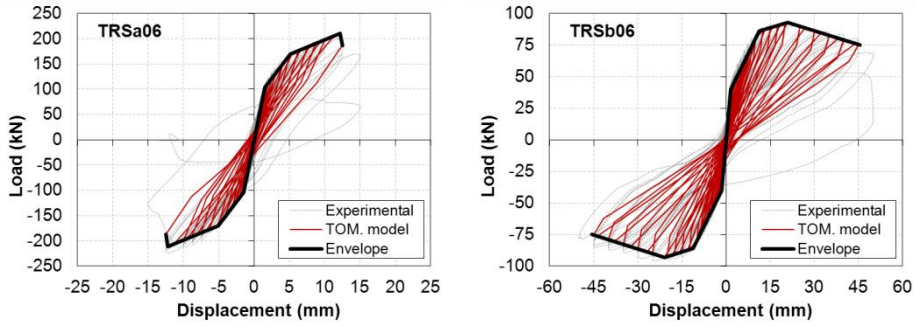

Fig. 4.1 Comparison between experimental and modelled cyclic shear compression tests with Tomaževič model. Squat (left) and slender (right) specimens tested under 0.6 N/mm^2 vertical compression.

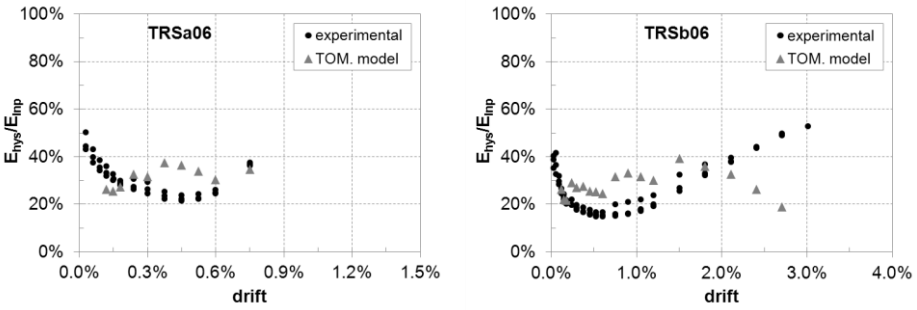

Fig. 4.2 Ratio between dissipated and input energy. Comparison between experimental and modelled values. Squat (left) and slender (right) specimens tested under 0.6 N/mm^2 vertical compression.

4.3 Hysteretic Model Description

4.3.1 General Scheme

The idealized envelope curves on which the construction of the hysteresis loops was based, were taken as the quadri-linear curves defined by the four experimental limit states given in § 3.2.3. It has been noticed that the first two limit states correspond to the main variation of tangent stiffness of the envelope of hysteresis loops, which can be considered as a general criterion for the estimation of limit states starting from the cyclic shear-compression test results.

This criterion consists on considering the envelope of hysteresis loops, that is the envelope of the points corresponding to maximum displacement at each cycle. In this way, we obtain two piecewise linear curves, one for positive displacement cycles and the other for negative displacement cycles. Then, for each curve, it is possible to compute the stiffness between two following points, that is the tangent stiffness to each linear branch.

Then, for each cycle, calculating the variation of the tangent stiffness compared to the previous one, it is possible to noticed that this variation is characterized by two minimum points, before the attainment of maximum resistance. These two points correspond to the main sensitive stiffness variation of the envelope. The corresponding displacements are very close to first two experimentally observed limit states.

The experimental observation on which the model is based are the follow:

1. The loading phase can be divided in two parts: the first part, with low displacement and high stiffness, and a second part with lower stiffness. The former remains almost unchanged among different loading cycles, with only low decay of stiffness values; conversely, the second phase presents high stiffness decay. Furthermore, the transition between these two parts occurs when forces and displacements are close to the first limit state and decreases with the increase of cycle amplitudes.
2. The un-loading phase can be subdivided in three parts: the first characterized by a high value of stiffness which determines the width of cycle and the dissipated energy, the second in which stiffness is almost the same as in the second loading phase. Finally, the third phase where stiffness increases again and remains constant in the succeeding loading phase of the following loading cycle. The latter increase of stiffness happens when forces are similar to those at the stiffness change during the loading phase, giving the typical S form of hysteresis cycles.

3. Repeated amplitude cycles shows high strength decay in the loading phase, whereas the unloading phase strength is almost unchanged compared to the first cycle of that amplitude. Hence, the following cycles with the same amplitude are smaller and less dissipates less energy compared to the first cycle.

Starting from these observations, the construction of the hysteresis loops has been based on the definition of four symmetrical points (A, B, C, D). These points are found by means of two coefficients: C_1 and C_2, which are calculated by imposing the equality of the input energy and the dissipated energy between experimental and modelled loops.

Modelling of the first cycles at each displacement level is carried out as follow. The system is linear elastic until the displacements are smaller than the first limit state. Non-linear inelastic behaviour starts beyond this level of displacement. For this reason, the modelling of hysteretic cycles begins at the first cycle that goes beyond the elastic limit.

Point A is always placed on the first branch of the skeleton curve, namely the linear elastic phase. Its ordinate is expressed as a function of the maximum resistance (H_{max}) using the coefficient C_1 and the Z parameter. Point B is found on the skeleton curve for a displacement corresponding to the current cycle amplitude. The slope of branch A-B (K_{A-B}) is stored and will be utilized for modelling both the negative part of the current cycle and the next cycle.

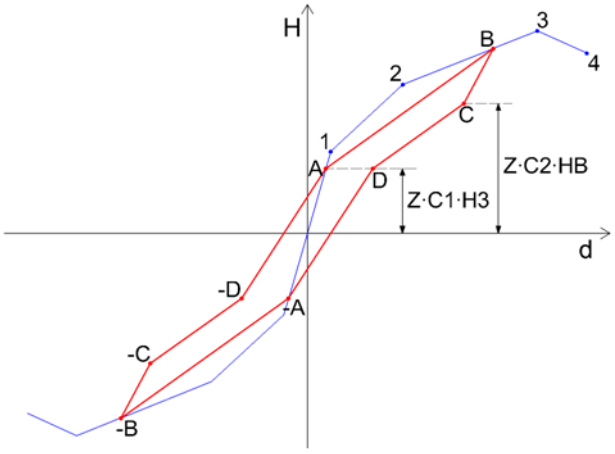

Fig. 4.3 Idealized envelope curve (blue) and general scheme of hysteretic model.

After point B, the system starts to unload. The ordinate of point C is expressed as a function of point B by means of C_2 coefficient and Z parameter. The slope of the first unloading branch (K_{B-C}) is defined by (Eq. 4.2). In such a way this stiffness

changes linearly from the value of the first branch of skeleton curve, i.e. the elastic stiffness, until the tangent stiffness at the second branch of skeleton curve, i.e. $K_{1\text{-}2}$. Point D has the same ordinate of point A, and is found by imposing the equality of slope $K_{C\text{-}D}$ and $K_{A\text{-}B}$. Beyond point D the system continues to unload, and it moves to the symmetrical points of A, B, C and D. Since displacements at point A remain almost constant, whereas displacements at point D increase along with the increase of the cycle amplitude, $K_{D\text{-}A}$ decreases at every modelled cycle (Fig. 4.4).

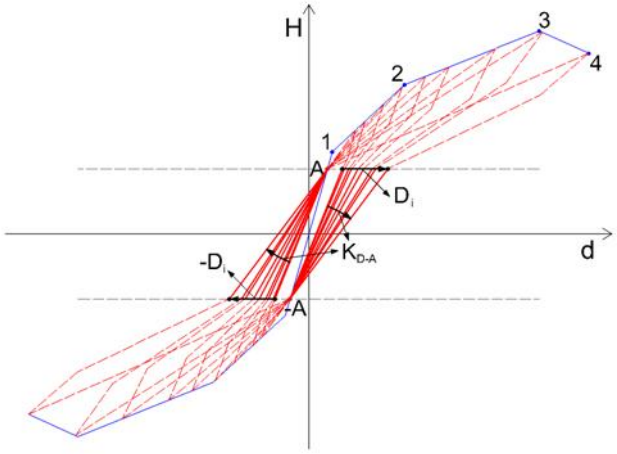

Fig. 4.4 Degradation of stiffness $K_{D\text{-}A}$.

$$C_K = \left(\frac{K_{1-2}}{K_1} - 1\right) \Big/ \left(\frac{d_4}{d_1} - 1\right) \qquad \textit{(Eq. 4.1)}$$

$$K_{BC} = K_1 \cdot \left[1 + C_K \cdot \left(\frac{d_B}{d_1} - 1\right)\right] \qquad \textit{(Eq. 4.2)}$$

$$d_E = \frac{H_{max}}{K_1} \qquad \textit{(Eq. 4.3)}$$

$$C_Z = \left(\frac{d_1}{d_E} - 1\right) \Big/ \left(\frac{d_4}{d_E} - 1\right) \qquad \textit{(Eq. 4.4)}$$

$$Z = 1 + \frac{1}{2} \cdot C_Z \cdot \left(\frac{d_B}{d_E} - 1\right) \leq 1 \qquad \textit{(Eq. 4.5)}$$

Z parameter (Eq. 4.5) is utilized in order to obtain constant values of C_1 and C_2 coefficients. Indeed, without using Z parameter, fitting of experimental tests would give a constant trend, for these coefficients, only for first cycles, followed by a decreasing trend with the increase of cycles amplitude. Hence, Z parameter can be seen as a corrector factor that allows to use a couple of constants for coefficients C_1 and C_2, that is appreciable from the implementation point of view, and at the same time to take into account their variation without introducing new independent parameters in the model. This parameter is a function of maximum displacement, and is evaluated on the basis of C_Z (Eq. 4.1) and d_E (Eq. 4.3), which indeed are evaluated on the basis of the basic model parameters. For displacements less than d_E, Z is considered equal to one. When maximum displacement has exceeded d_E, Z decreases linearly. This parameter has to be updated each time a new d_{max} is reached, and so for every d_B since every cycle has an amplitude greater than the previous ones.

4.3.2 Arrangement of Hysteretic Model for Random Input

The model, as it has been defined, assumes to know the amplitude of each cycle. Furthermore, every cycle is greater than the previous one, so the displacement at point B (d_B) is also the maximum current displacement (d_{max}). So it is possible to define for each cycle the stiffness of the branch A-B (K_{A-B}) as the stiffness that brings the system to moves exactly from point A to point B. Since the final aim of the model is to carry out dynamic analyses, in general it is impossible assuming a priori the amplitude of cycles. Indeed, the earthquake induced displacements represent the unknown quantities. Therefore, K_{A-B} has been re-defined by taking into account the displacement history of the system, so as to ensure increasing stiffness degradation for increasing displacements.

Referring to i-th cycle, represented in Fig. 4.5, the model initially takes d_{max} to be equal to d_{B-1}, (maximum displacement of the previous cycle). Current stiffness K_{A-B} is thus secant to A_{i-1} and B_{i-1}. Therefore, the system moves from A_{i-1} point in order to reach B_{i-1} point, which is placed on the skeleton curve. Then it continues following the skeleton curve until the attainment B_i point, that represents the current d_{max}. At this point, Z is updated, so that the current A_i point, and the exact negative loading branch of the hysteresis loop can be calculated. This means that asymmetrical cycles are obtained. The unloading phase flows the rules described in the previous paragraph.

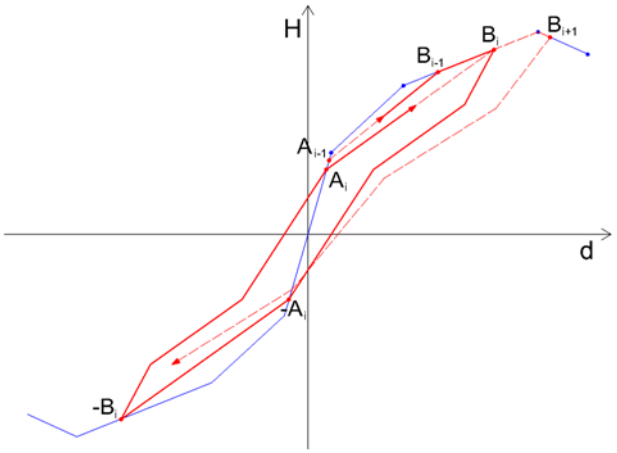

Fig. 4.5 Asymmetrical cycles.

4.4 Experimental Shear Compression Tests and Modelling

Calibration of the hysteretic model was carried out on the basis of cyclic shear compression tests. In the next paragraphs the results obtained for reinforced and strengthened masonry are presented, in terms of comparison between experimental and modelled hysteretic cycles and also ratio between dissipated and input energy.

4.4.1 Reinforced Masonry

Fig. 4.6 and Fig. 4.7 show the comparison between the experimental data and the modelled hysteretic loops. As can be seen, there is fair good agreement for both failure modes, namely shear or combined shear/flexural failure for specimens “a” and flexural failure for specimens “b”. From the comparison between experimental and modelled values of the ratio between dissipated and input energy (Fig. 4.8 and Fig. 4.9), it is possible to distinguish a difference in trend. Indeed, experimental data shows a “U” trend, with high values at firsts cycles, the minimum between d_{CR} and d_{Hmax} and then an increasing trend until maximum displacement. On the contrary, the model energy ratio has an always increasing trend and, in particular, the first descending branch for displacements smaller than d_{CR} is absent. However, the average value of several relative differences at each cycle is lower than 10 % for each specimen.

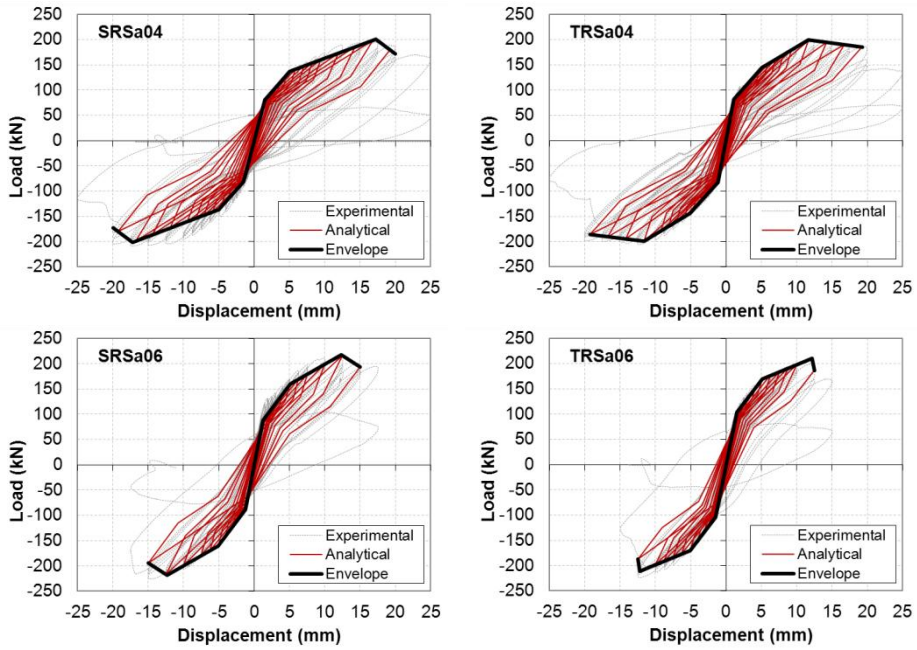

Fig. 4.6 Comparison between experimental and modelled cyclic shear compression tests. Squat specimens tested under 0.4 N/mm^2 (above) and 0.6 N/mm^2 (below) vertical compression.

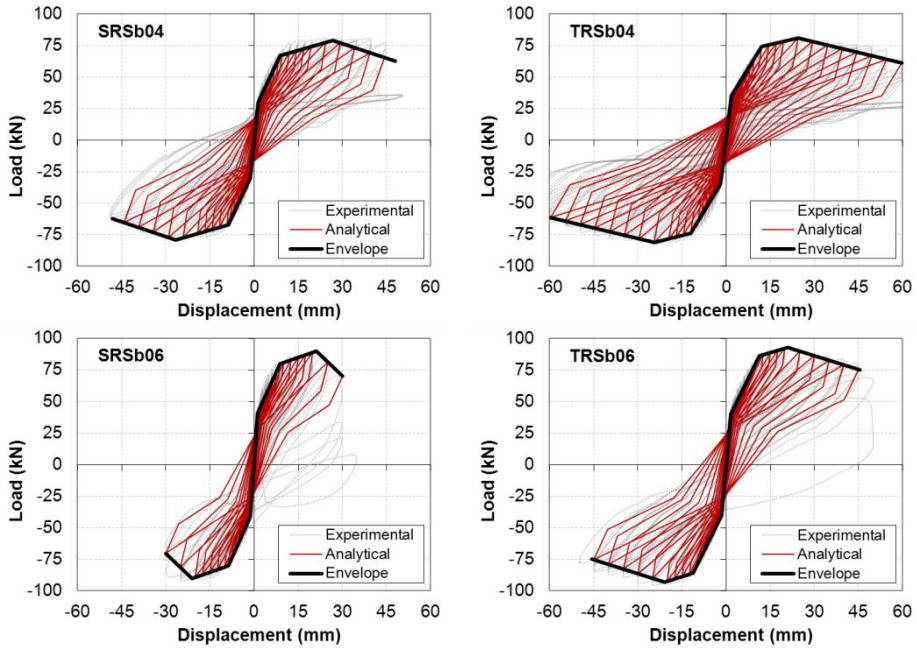

Fig. 4.7 Comparison between experimental and modelled cyclic shear compression tests. Slender specimens tested under 0.4 N/mm^2 (above) and 0.6 N/mm^2 (below) vertical compression.

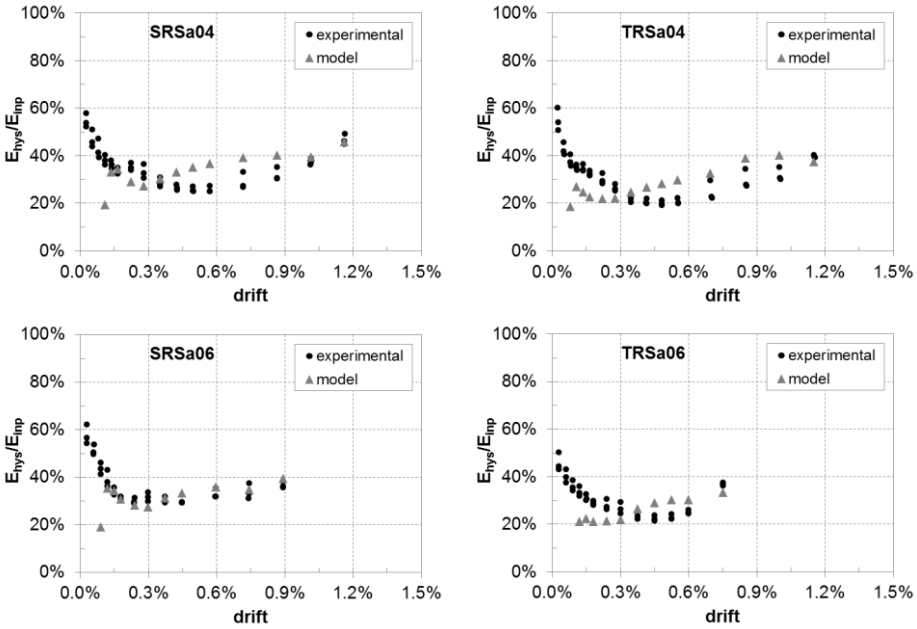

Fig. 4.8 Ratio between dissipated and input energy. Comparison between experimental and modelled values. Squat specimens tested under 0.4 N/mm^2 (above) and 0.6 N/mm^2 (below) vertical compression.

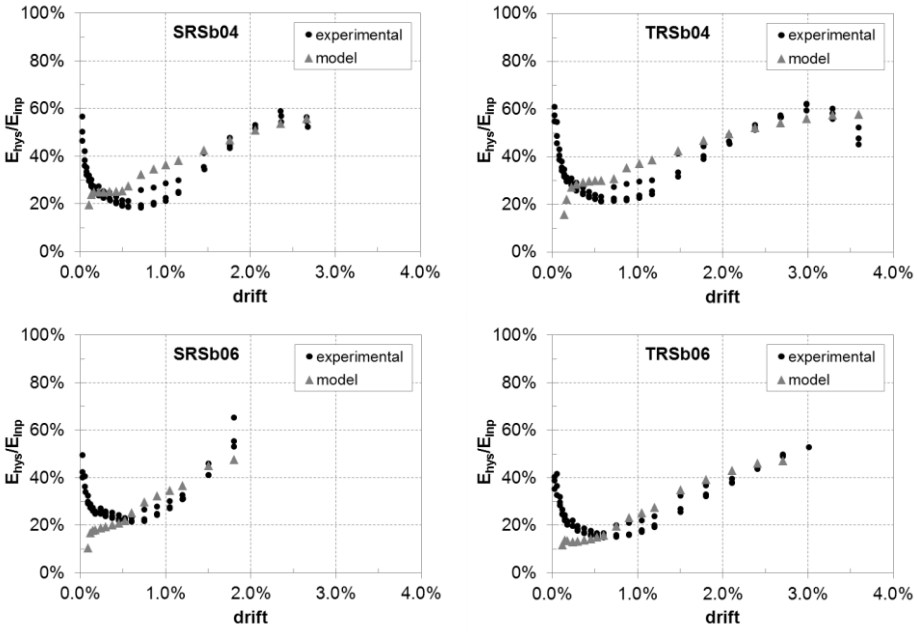

Fig. 4.9 Ratio between dissipated and input energy. Comparison between experimental and modelled values. Slender specimens tested under 0.4 N/mm^2 (above) and 0.6 N/mm^2 (below) vertical compression.

Squat walls	C_1	COV C_1	C_2	COV C_2
SRSa 0.4	0.402	12.5 %	0.836	8.3 %
TRSa 0.4	0.398	14.0 %	0.904	6.7 %
SRSa 0.6	0.424	6.0 %	0.846	4.1 %
TRSa 0.6	0.466	7.0 %	0.892	7.5 %
mean	*0.422*	*9.9 %*	*0.869*	*6.6 %*
Slender walls	C_1	COV C_1	C_2	COV C_2
SRSb 0.4	0.311	20.2 %	0.852	6.6%
TRSb 0.4	0.311	22.4 %	0.803	8.0 %
SRSb 0.6	0.391	17.5 %	0.922	2.7 %
TRSb 0.6	0.396	10.8 %	0.950	2.0 %
Mean	*0.352*	*17.7 %*	*0.882*	*4.8 %*

Table 4.1 Hysteretic model coefficients C_1 and C_2 for Reinforced Masonry.

4.4.2 Strengthened Masonry

The same calibration described in the previous paragraph was repeated for strengthened masonry. For this type of masonry, three limit states have been identified, i.e. cracking limit, maximum resistance and maximum displacement. The developed model takes into account also a fourth LS, i.e. flexural limit, for the definition of idealized envelope curve. Hence, the experimental results have been analysed using the criterion of variation of tangent stiffness in order to identify this limit. In this way, it has been possible modelling the cycles before cracking limit, which would been neglected using three LS, as shown in Fig. 4.10. The obtained LS, used in the modelling, are listed in Table 4.2.

For this type of masonry, the equivalence of energies for determination of coefficients C_1 and C_2 led to constant values independently of amplitude of cycles. This can be noticed observing the low values of COV reported in Table 4.3. So the parameter Z was set to one for this modelling.

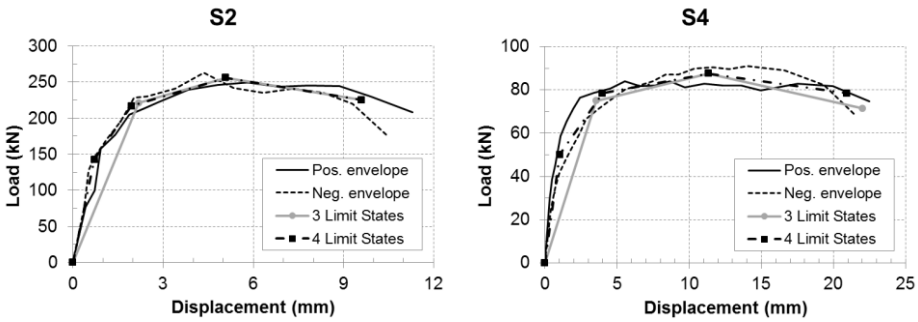

Fig. 4.10 Comparison between three and four limit states idealization of hysteresis envelope curve. Squat specimens tested under 2.0 N/mm^2 (left) and slender specimen tested under 1.0 N/mm^2 (right) vertical compression.

Fig. 4.11 and Fig. 4.12 show a comparison between experimental and modelled cyclic tests, whereas Fig. 4.13 and Fig. 4.14 show the comparison in terms of ratio between dissipated and input energy. As well as for reinforced masonry, there is a difference in trend between experimental values and model. "U" trend, with a descending branch followed by an ascending one, characterizes the experimental, whereas the model has an always increasing trend. In any case, the differences is very small, generally lower than 5 %. In addition, it can be noticed that beyond $d_{CR,}$ experimental and modelled energetic ratio are almost superimposed.

Specimen	Flexural limit		Cracking limit		Max. Resist.		Max. Displ.	
	δ_f mm	H_f kN	δ_{cr} mm	H_{cr} kN	δ_{Hmax} mm	H_{max} kN	δ_{max} mm	$H_{\delta max}$ kN
R2	0.90	132	2.40	170	5.09	187	11.76	147
S2	0.72	142	1.94	217	5.08	256	9.60	225
R4	1.78	63	4.72	75	14.59	80	24.67	75
S4	1.03	50	3.99	78	11.33	88	20.92	78
R5	1.24	77	3.59	108	6.58	121	11.09	97
S5	1.06	67	3.12	102	7.32	121	9.81	108

Table 4.2 Limit states obtained with tangent stiffness criteria.

Squat walls	C_1	COV C_1	C_2	COV C_2
R2 1.0	0.698	1.5 %	0.821	0.6 %
S2 2.0	0.482	14.1 %	0.623	6.7 %
Mean	*0.590*	*7.8 %*	*0.722*	*3.6 %*
Slender walls	C_1	COV C_1	C_2	COV C_2
R4 1.0	0.663	15.0 %	0.879	6.2 %
S4 1.0	0.480	11.8 %	0.816	3.2 %
R5 2.0	0.549	11.8 %	0.695	11.3 %
S5 2.0	0.546	1.8 %	0.696	9.0 %
Mean	*0.560*	*10.1 %*	*0.772*	*7.4 %*

Table 4.3 Hysteretic model coefficients C_1 and C_2 for Strengthened Masonry.

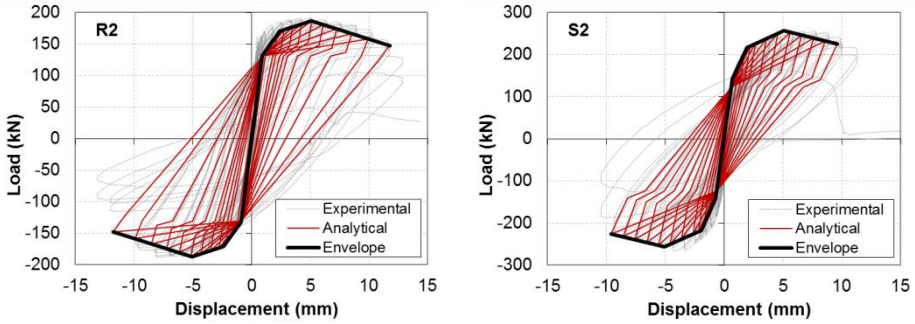

Fig. 4.11 Comparison between experimental and modelled cyclic shear compression tests. Squat specimens tested under 1 N/mm^2 (left) and 2 N/mm^2 (right) vertical compression.

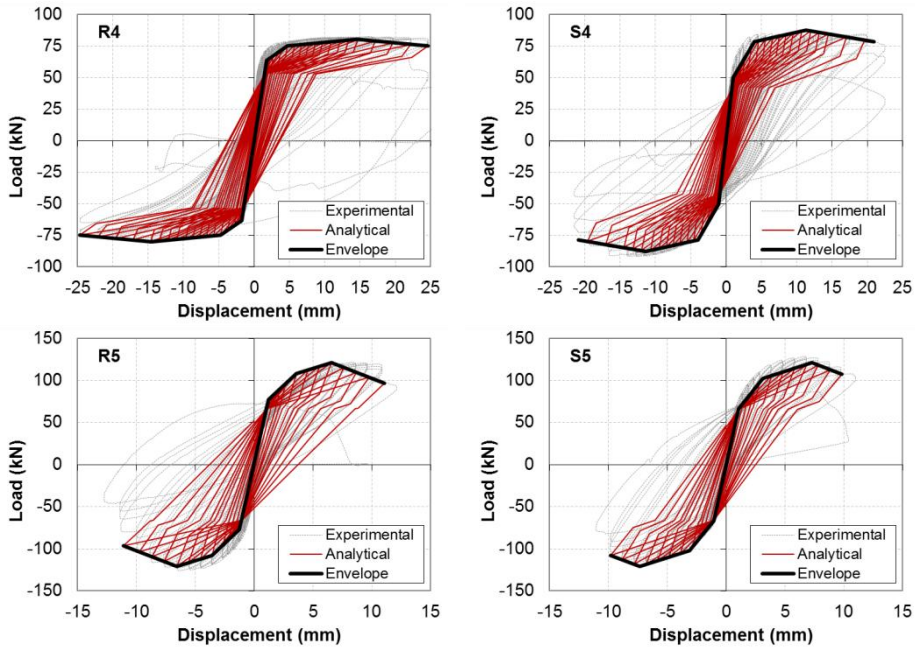

Fig. 4.12 Comparison between experimental and modelled cyclic shear compression tests. Slender specimens tested under 1 N/mm^2 (above) and 2 N/mm^2 (below) vertical compression.

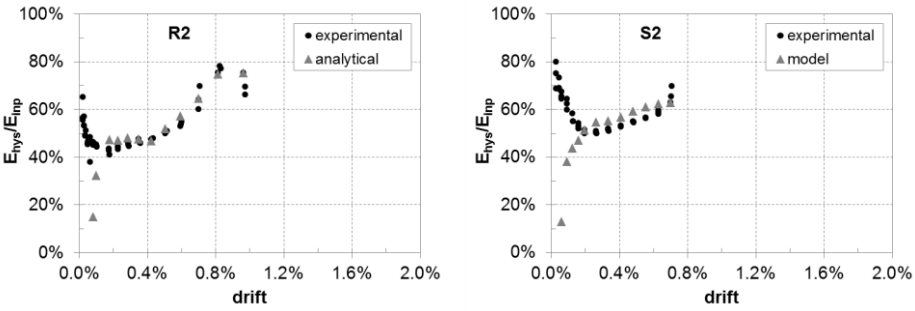

Fig. 4.13 Ratio between input and dissipated energy. Comparison between experimental and modelled values. Squat specimens tested under 1 N/mm^2 (left) and 2 N/mm^2 (right) vertical compression.

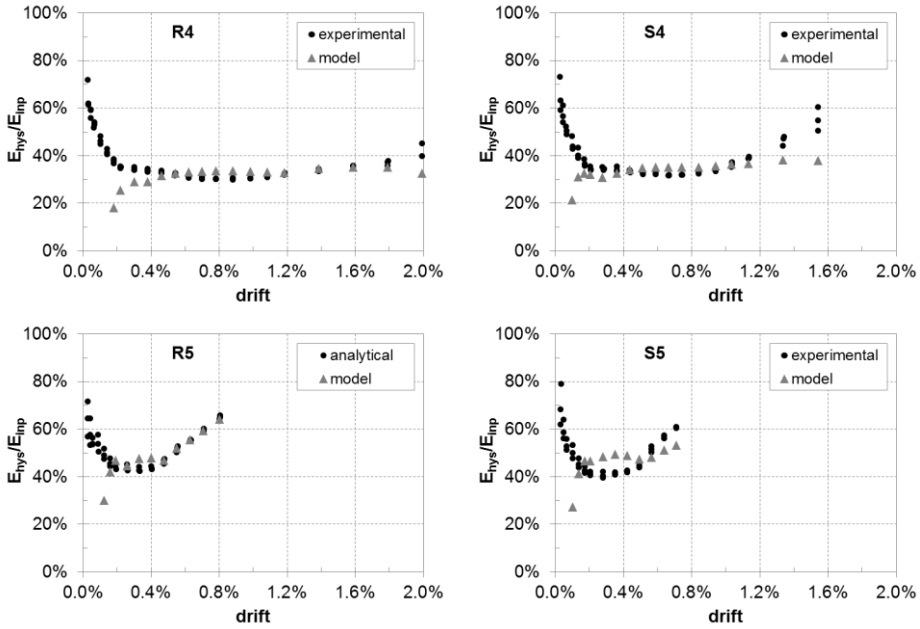

Fig. 4.14 Ratio between input and dissipated energy. Comparison between experimental and modelled values. Slender specimens tested under 1 N/mm^2 (above) and 2 N/mm^2 (below) vertical compression.

4.5 Implementation of Model

The model was implemented in MATLAB environment, in order to carry out non-linear time-histories (NLTH) analyses. The greater difficult in this phase was to predict every situation that can arise during a dynamic analysis, and provide the model with precise rules so that it behaves properly.

An important feature is that regarding the stiffness of the section D-A (K_{D-A}). This stiffness cannot be defined implicitly as the secant to points D and A, as above described. Indeed, for casual cycle amplitudes, the monotone degradation is not ensured. Therefore, when the slope of the section D-A is lower than the current K_{D-A}, the latter is updated according to the D-A secant. Thus, the system passes through point A. Otherwise, beyond point D, the system moves with the current stiffness K_{D-A} until it reaches the strength H_A, defining point E. After point E, K_{A-B} is used.

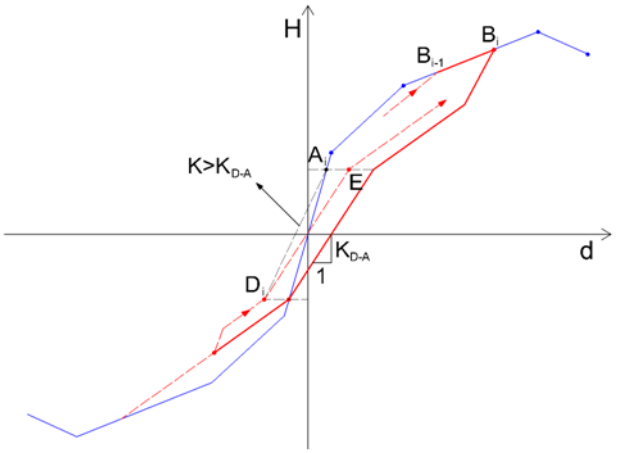

Fig. 4.15 Stiffness of branch D-A and definition of point E..

4.5.1 Re-loading Rules

The possibility of un-loading considered until now occurs in the section A-B, but this is merely one of the possible conditions. Indeed, during a dynamic analysis, the direction of displacement may change at any time. It is therefore possible to distinguish other two cases: displacement inversion in sections B-C or C-D (Fig. 4.16 on the left) and displacement inversion in the section D-A (Fig. 4.16 on the right).

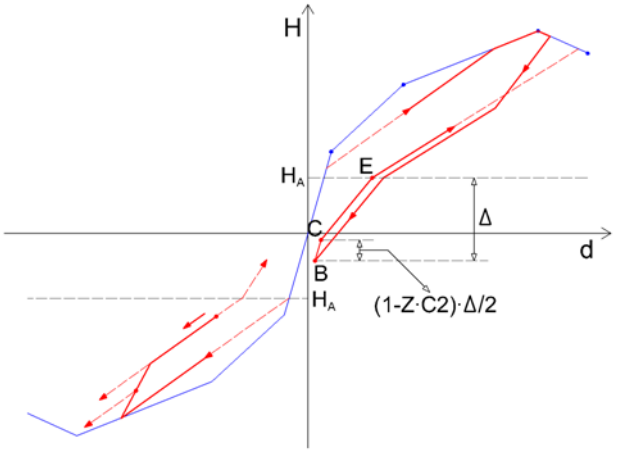

Fig. 4.16 Re-loading conditions.

In the first case, the system simply changes its direction, and starts reloading with stiffness K_{A-B}. On the contrary, in the second case, the cycle opens, according to parameter Z, coefficient C_2 and amplitude Δ. This amplitude represent the difference between load levels H_A and the point at which displacement inversion occurs (Fig. 4.16). Reloading in section D-A is characterised by a first branch, B-C, with stiffness K_{B-C}, and a second branch C-E with stiffness K_{D-A}. After point E, the system moves with K_{A-B} stiffness. In this way, there are no discontinuities of behaviour due to the random position of reloading. Indeed, if we consider a re-loading point in the D-A branch, the nearer the system is to point D, the more elastic its behaviour is, as it would occurs if re-loading point was before point D. Conversely, the nearer the system is to point A, the more similar its behaviour is to the response that it would has if it overcame point A. This means that nearer the re-loading point is to point A, the larger cycle width is, because this is proportional to amplitude Δ, that is maximum when re-loading point corresponds to point A, ($\Delta = 2 \cdot H_A$), and minimum when re-loading point corresponds to point D, ($\Delta = 0$).

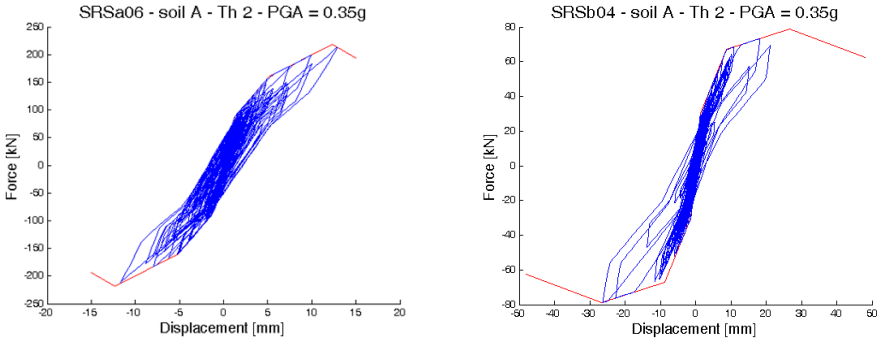

Fig. 4.17 Results of NLTH analyses: Force-Displacement graphs. Shear (left) and flexural (right) behaviour under the same Time History at 0.35 g.

The last phase of the implementation was the debugging. In order to solve every kind of numerical instability, a large number of NLTH analyses were carried out, using several time histories at different levels of Peak Ground Acceleration (PGA). Fig. 4.17 shows the results of two analyses utilizing the same time history at the same PGA, for the specimens Sa06 and Sb04, representative of shear and flexural behaviour respectively.

4.6 Conclusive Remarks

In this chapter the development of an hysteretic model has been described. This model is enough accurate in modelling the actual behaviour for both failure modes of RM and, with a little variation, also for SM. In particular it can be highlighted that:

- The relative error between modelled and experimental input or dissipated energy is in average lower than 10% and 15%, respectively.
- The model has been implemented in Matlab environment, in order to carry out dynamic analyses. For what concerns the integration of equation of motion, it was used the Newmark constant average acceleration scheme.
- The model was then tested, performing a large number of analyses using several time histories, in order to highlight and debug eventual instability until it has proven to be robust and capable of performing non-linear analyses with very low computational effort.

5 NON-LINEAR DYNAMIC ANALYSES OF SINGLE DEGREE OF FREEDOM MASONRY STRUCTURES

5.1 Introduction

In this chapter a procedure for the determination of equivalent viscous damping (ξ_{eq}) is presented. This procedure can be divided in two phases: in the first phase nonlinear time history (NLTH) analyses are carried out using the hysteretic model described in previous chapter. NLTH analyses makes use of synthetic time histories. In the second phase, through an equivalent elastic system, ξ_{eq} is defined. The procedure has been applied to both modern reinforced masonry and injected stone masonry walls described in chapter 3.

5.2 Procedure

The scope of the procedure is to determine the value of viscous damping that has to be applied to an equivalent linear system in order to obtain the same response of the inelastic system. This equivalence is done in terms of peak displacement. For each time history considered, the following steps are performed:

1. *Definition of target displacements*.
   Hysteretic model considers the system response as elastic until the achievement of first limit state. Hence, target displacements are placed from first limit state until the ultimate displacement capacity. n equal-spaced points subdivide the non-linear part of envelope curve (it was chosen n = 7).
2. *Search of PGA multiplier factor.*
   For each target displacement, NLTH analyses using the 10 synthetic time histories are carried out. Elastic damping is taken close to zero. These analyses are repeated scaling the TH using a multiplier factor of PGA until the maximum displacement achieved by NLTH is equal to target displacement within a specified tolerance. It is a iterative procedure and at each iteration the PGA is updated from previous one taking into account the difference between the actual maximum and the target displacement.
3. *Determination of secant stiffness and effective period.*

When target displacement is achieved, we know the multiplier factor of PGA to achieve it. Thus the corresponding secant stiffness can be calculated by the point on the envelope curve at target displacement. Knowing the secant stiffness, it is easy to obtain the effective period:

$$T_{eff} = 2\pi \cdot \sqrt{\frac{m}{K_S}} \qquad \textit{(Eq. 5.1)}$$

4. *Definition of Equivalent Linear System.*
   The linear elastic equivalent system is defined through effective period (or the corresponding secant stiffness) given from previous step and from elastic component of damping equal to that used in point 2. On this system, a TH analysis is carried out using scaled PGA in point 2. Maximum displacement obtained from this analysis represents the linear response of equivalent system for the considered elastic damping.
5. *Search of Equivalent Viscous Damping.*
   Equivalent viscous damping (ξ_{eq}) is the value of damping which makes equal the displacement of the equivalent linear system and the target displacement. Hence, for each iteration, linear elastic analysis is repeated varying the damping value on the basis of the difference between the obtained and the target displacements.

NLTH analyses were carried out using the Newmark constant average acceleration integration scheme. Elastic damping coefficient used in point 2 of the procedure is close to zero because the aim is finding the damping component due to hysteretic dissipation. To avoid numerical problems, the starting value of elastic damping was set at a very low value, but zero. It was chosen a conventional value of 0.5% (one tenth of usual elastic damping component). The tolerance imposed in NLTH analyses to find the PGA was set to 2% of target displacement, while for linear elastic analyses it was set to 1%.

5.3 Seismic Input Used in the Analyses

Dynamic analyses were carried out on 10 synthetic time-histories composed of 2048 points taken at a sampling frequency of 100 Hz. The time-histories were created in MATLAB™, and are compatible with the type 1 spectra of (EN 1998-1,

2004) with a lower bound and upper bound of 10% of deviation between generated and code-prescribed spectra in the period range from 0.10 to 2.00 s. In Fig. 5.1 the elastic response spectra recommended by code are reported, their Peak Ground Acceleration (PGA) is normalized to a_g.

Definition of the response spectra varies according to the different types of soils. The main five soil categories are: A, rock or other rock-like geological formation; B, very dense sand, gravel, or very stiff clay; C, medium-dense sand, gravel or medium stiff clay; D, loose-to-medium cohesionless soil or predominantly soft-to-firm cohesive soil; E, soil profile consisting of a surface alluvium layer.

The analyses were repeated for the two limit soil groups, i.e. soil A and soil D. Despite soil E has a peak spectral acceleration higher than soil D, the latter shows a larger plateau, that means a bigger seismic demand at medium-high periods. Hence, the effective response in the non-linear range determine an increase of effective periods, that are often beyond the T_C of soil E (i.e. 0.5 s). To characterize the whole response until the ultimate capacity, soil D spectra appear to be more severe.

Fig. 5.2 and Fig. 5.3 show the spectrum-compatibility between mean value of 10 time-histories normalized to a_g and the corresponding code spectra for the two types of soil: A (rock soil) and D (soft soil), in the period range 0.10-2.0 s. Out of this range, time-histories spectra diverge from code spectra. This is more evident in displacement response spectra, as can be seen in Fig. 5.3. Anyway, this does not affect the analyses, as the periods range of interest, as will be show in the following paragraphs, is included between 0.1 and 1.0 s.

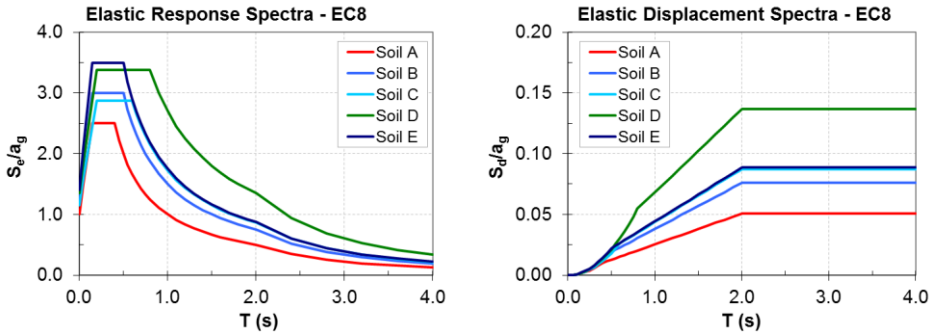

Fig. 5.1 Eurocode 8 recommended elastic response acceleration (left) and displacement (right) spectra.

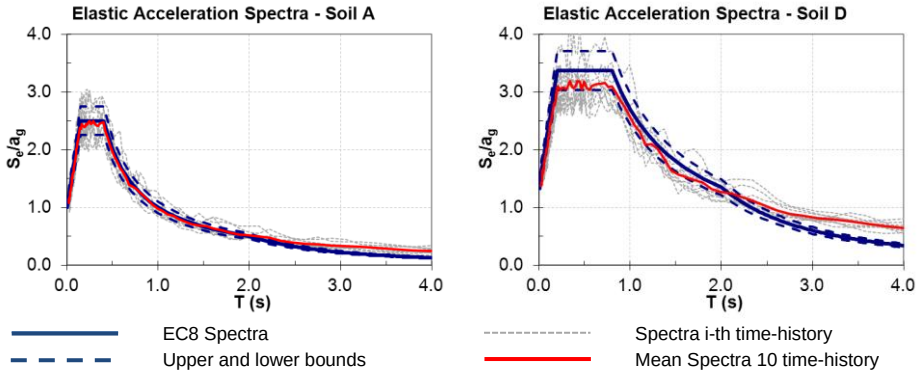

Fig. 5.2 Elastic response spectra of the utilized time-histories and code recommended acceleration spectra for soil A (left) and D (right).

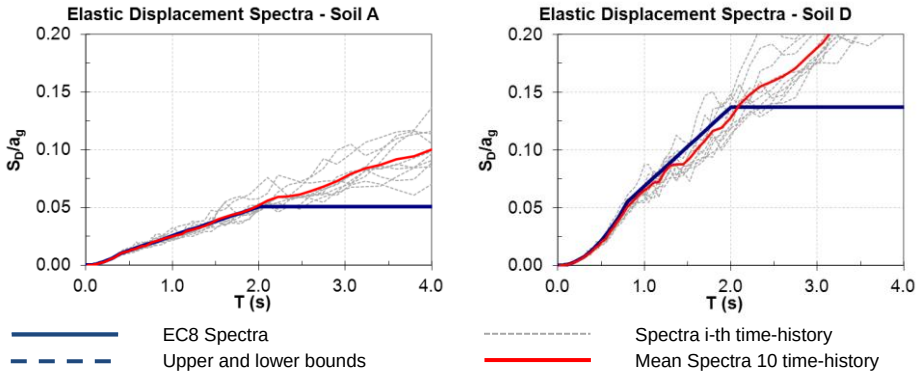

Fig. 5.3 Elastic response spectra of the utilized time-histories and code recommended displacement spectra for soil A (left) and D (right).

5.4 Results of the Analyses

In this section, results of the described procedure are presented. For each modelled specimen (8 for RM system and 6 for SM system), the procedure was repeated for each target displacement (7) and for each time history (10) generated for both ground type considered (A and D), giving a total number of 1960 runs. The obtained values of ξ_{eq} are related to drift ratio, instead of displacement, to achieve results that are independent from the specimens dimensions. Furthermore, other two important results are obtained applying this procedure: the first is the ratio between elastic and inelastic displacements. The second is the relationship between the displacements ratio and ξ_{eq}.

5.4.1 Reinforced Masonry (RM)

5.4.1.1 Equivalent Viscous Damping

In Fig. 5.4 and Fig. 5.5 the results of this procedure for reinforced masonry system are presented, divided for soil type. Each line in the figures represents one experimental wall. Each of the seven dots composing the line is the mean value of the results obtained using 10 time histories, at the corresponding target displacement. It can be seen that, obviously, damping is almost zero at the elastic limit (not zero because elastic component was set to 0.5%) and, in general, it shows a logarithmic trend with increasing target displacements. It can be noticed how, at the same drift level, shear behaviour of walls (red and orange curves) involves higher values of damping compared to flexural behaviour (blue and light blue curves). When shear failure occurs damping shows a sudden increase, after displacement at maximum strength (drift 0.7÷1.0%). It increases by about 50%, going from values around 10% to value around 15%.

In Fig. 5.5 the same results are showed, but displacements are a-dimensionalised to the second limit state (d_{cr}). This limit was chosen as it is representative of damage state in relation with failure mode. Indeed, as reported in Table 3.5, the drift level at critical LS is around 0.30% for shear behaviour, whereas it is about twice this value for flexural behaviour (0.53÷0.7%). It can be noted that damping curves, plotted against this displacement ratio (DR), tend to be superimposed, for both failure modes and both soil types considered.

Regarding period shift, as reported in Table 5.1, it can be said that, for shear walls, effective period ranges from 0.10 s at elastic limit until about 0.30 s at ultimate displacement capacity. For flexural walls, indeed, this range is between 0.15 and 0.65 s. Taking into account the recommended spectra for ground types A and D, the period shift for all walls is included in the plateau ($T_B < T_{eff} < T_C$) with the exception of flexural walls on soil A ($T_C = 0.4$ s). This explains why obtained curves for soil A and flexural behaviour (blue and light blue), tend to stabilize around 12% for Displacement Ratios bigger than 2. On the contrary for soil D, whose spectrum is characterized by a wider plateau ($T_C = 0.8$ s), an always increasing trend, until values of about 20%, can be noted.

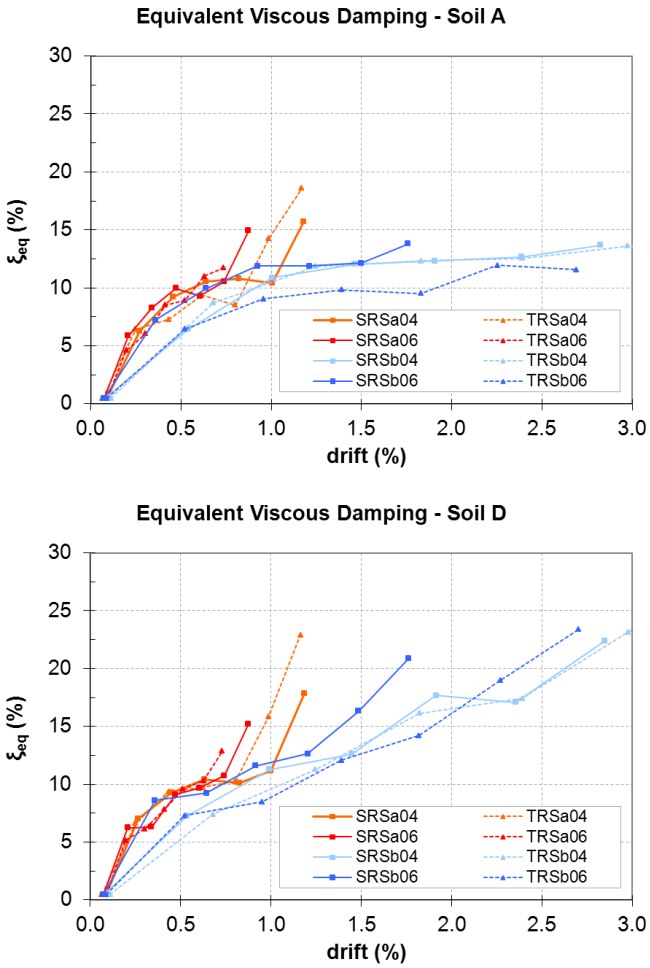

Fig. 5.4 Equivalent Viscous Damping versus Drift.
Experimental RM walls on soil type A (above)and type D (below).

Squat walls	T_{EL} (s)	T_U (s)
SRSa 0.4	0.11	0.29
TRSa 0.4	0.10	0.27
SRSa 0.6	0.12	0.29
TRSa 0.6	0.13	0.27
mean	*0.12*	*0.28*
Slender walls	T_{EL} (s)	T_U (s)
SRSb 0.4	0.15	0.61
TRSb 0.4	0.16	0.68
SRSb 0.6	0.15	0.56
TRSb 0.6	0.17	0.66
Mean	*0.16*	*0.63*

Table 5.1 Period Shift for Reinforced Masonry

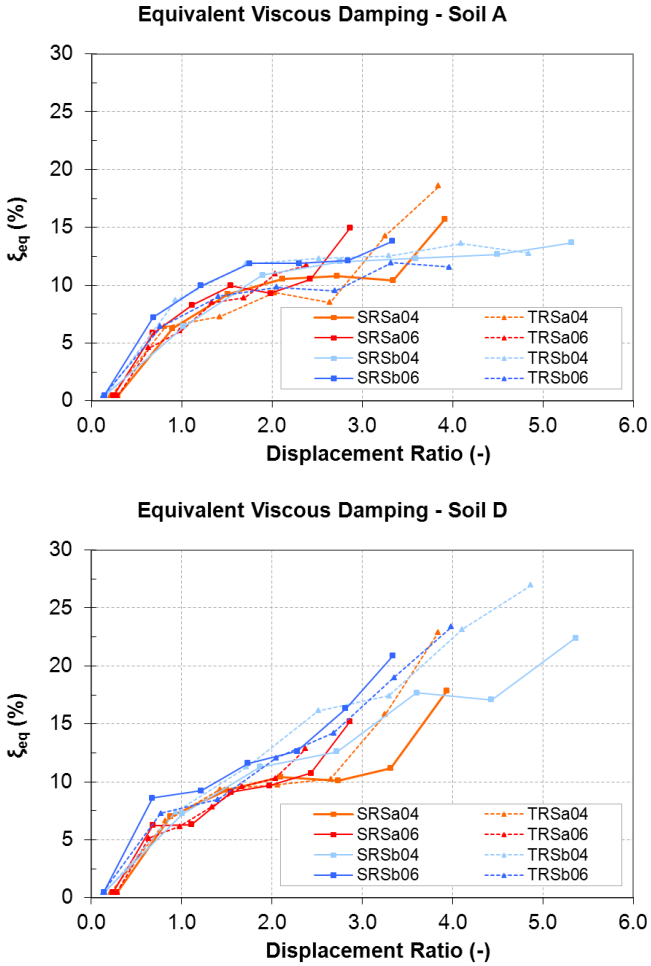

Fig. 5.5 Equivalent Viscous Damping versus Displacement Ratio. Experimental RM walls on soil type A (above)and type D (below).

5.4.1.2 Relationship between Elastic and Inelastic displacements

Fig. 5.6 and Fig. 5.7 show the ratio between elastic and inelastic displacements (d_{IN}). The latter are the target displacements, or more precisely, the displacements obtained during step 2 of the procedure. Elastic displacements (d_{EL}) were computed utilizing the Equivalent Linear System obtained in step 3 of procedure, and considering an elastic damping set to 5%. This value of damping was chosen as it is the value of elastic damping that normally is considered in the codes ((DM 14/01/2008, 2008) and (EN 1998-1, 2004)) for the definition of elastic spectra. This means that d_{EL} represents the actual spectra ordinate for the considered time-history and effective period. Since the used time histories are spectrum compatible, as shown in Fig. 5.3, the ratio between elastic and inelastic displacement can be

considered as the relationship between elastic displacement spectrum and actual displacement response of masonry walls.

If we do not consider the values obtained at first target displacement, elastic displacement is always greater than inelastic, so their ratio is bigger than 1. The reason of this is that elastic displacement is computed considering the damping constant and equal to 5%. But observing the obtained damping curves, it is possible to notice that damping is always greater than 5%, with the exception of the values obtained at the first target displacement. Hence, generally in the elastic analyses the value of damping is underestimated, and this is the reason why elastic displacement is greater than inelastic. So their ratio (d_{EL}/d_{IN}) is bigger than one. For this reason the axes scales in Fig. 5.6 and Fig. 5.7 are not the same. More precisely, the grid of Y axis is twice that of X axis. This means that the bisector of these graph represents a constant ratio between elastic and inelastic displacement, equal to 2.

In the figures, the results obtained for the ground type A are pointed with a circular indicator, whereas the obtained results for ground type D are pointed with a triangular indicator. The trend of ratio between d_{EL} and d_{IN} is ascending, but not really constant. A good approximation can be obtained considering the type of power function expressed by (Eq. 5.2). The latter was used to determine the best regression functions using the least squares fitting technique. In Fig. 5.6 and Fig. 5.7 these functions are shown, using continuous line for A soil and dashed line for D soil.

$$d_{EL} = \beta \cdot d_{IN}{}^{\gamma} \qquad \textit{(Eq. 5.2)}$$

It can be noticed that, for shear behaviour, there are not sensitive differences between the results obtained for the two types of considered soil. Indeed, the regression curves for each panel are almost superimposed. On the contrary, for flexural behaviour, it can be noticed that the two curves are initially superimposed, but they start to diverge for increasing displacements. In this case, curves for soil D are above those obtained for soil A. This phenomenon is more evident for panels of series T (horizontal reinforcement made by prefabricated steel trusses).

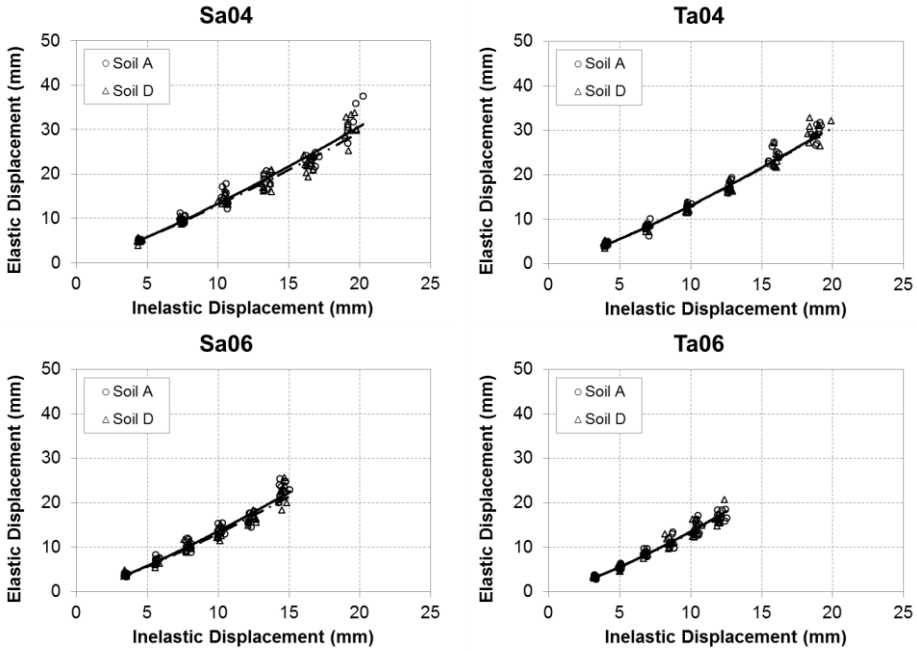

Fig. 5.6 Elastic displacement versus Inelastic displacement. Squat specimens with pre-load corresponding to 0.4 N/mm^2 (above) and 0.6 N/mm^2 (below).

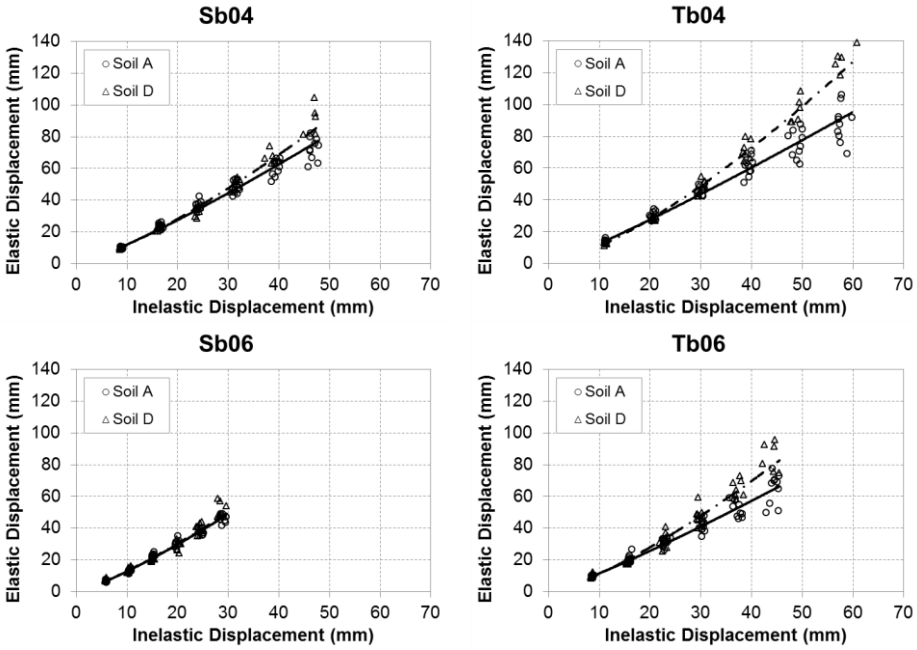

Fig. 5.7 Elastic displacement versus Inelastic displacement. Slender specimens with pre-load corresponding to 0.4 N/mm^2 (above) and 0.6 N/mm^2 (below).

Squat walls	β Soil A	γ Soil A	R^2	β Soil D	γ Soil D	R^2
SRSa 0.4	0.835	1.203	0.974	0.864	1.176	0.975
TRSa 0.4	0.755	1.238	0.985	0.764	1.232	0.983
SRSa 0.6	0.809	1.226	0.975	0.802	1.212	0.975
TRSa 0.6	0.701	1.286	0.972	0.741	1.250	0.976
mean	*0.775*	*1.238*		*0.793*	*1.218*	
Slender walls	β Soil A	γ Soil A	R^2	β Soil D	γ Soil D	R^2
SRSb 0.4	0.791	1.185	0.983	0.611	1.280	0.988
TRSb 0.4	0.945	1.127	0.975	0.451	1.337	0.991
SRSb 0.6	0.776	1.218	0.988	0.781	1.223	0.978
TRSb 0.6	0.814	1.153	0.973	0.545	1.315	0.977
Mean	*0.832*	*1.171*		*0.597*	*1.289*	

Table 5.2 Regression functions for ratio between d_{EL} and d_{IN}: β and γ coefficients and coefficient of determination R^2.

Values of obtained regression functions are reported in Table 5.2. The chosen power function is able to approximate very well the trend of ratio between d_{EL} and d_{IN}. Indeed the values of coefficient of determination R^2 are very high, all of them are greater than 0.97. A more detailed discussion and analyses of these results will be present in the next chapter.

5.4.1.3 Damping Correction Factor

Another important issue of this research is to study the relationship between ratio d_{EL}/d_{IN} and damping. Indeed, for each point of graphs in Fig. 5.6 and Fig. 5.7 it is possible to associate a value of damping. The ratio between d_{IN} and d_{EL} is usually defined as Damping Correction Factor (η). Many authors propose to express this factor as function of Equivalent Viscous Damping (ξ_{eq}), using expression like:

$$\eta = \sqrt{\frac{\alpha + \xi_{EL}}{\alpha + \xi_{EQ}}} \qquad \textit{(Eq. 5.3)}$$

where α is a coefficient, ξ_{EL} is conventional damping considered in elastic response spectra (i.e. 5%) and ξ_{EQ} is Equivalent Viscous Damping. In (EN 1998-1, 2004) and (DM 14/01/2008, 2008) the value of coefficient α is set to 5. Fig. 5.8 and Fig. 5.9 show the obtained relationship between η factor and ξ_{eq}. It has been used the same convention used in the previous graphs, regarding the soil types. Furthermore, the function expressed by (Eq. 5.3), considering α equal to 5, is indicated in dashed line.

It seems there is no significant difference between soil A and D. Indeed circular and triangular indicators are almost superimposed. Furthermore, as can be noticed in Fig. 5.8 and Fig. 5.9, there is a good correlation between the obtained results and

code proposed function, but probably it is possible to better calibrate coefficient α using the least squares method. Indeed, as reported in Table 5.3, the values of Coefficient of Determination obtained utilizing α equal to 5 are very low, all lower than 0.73.

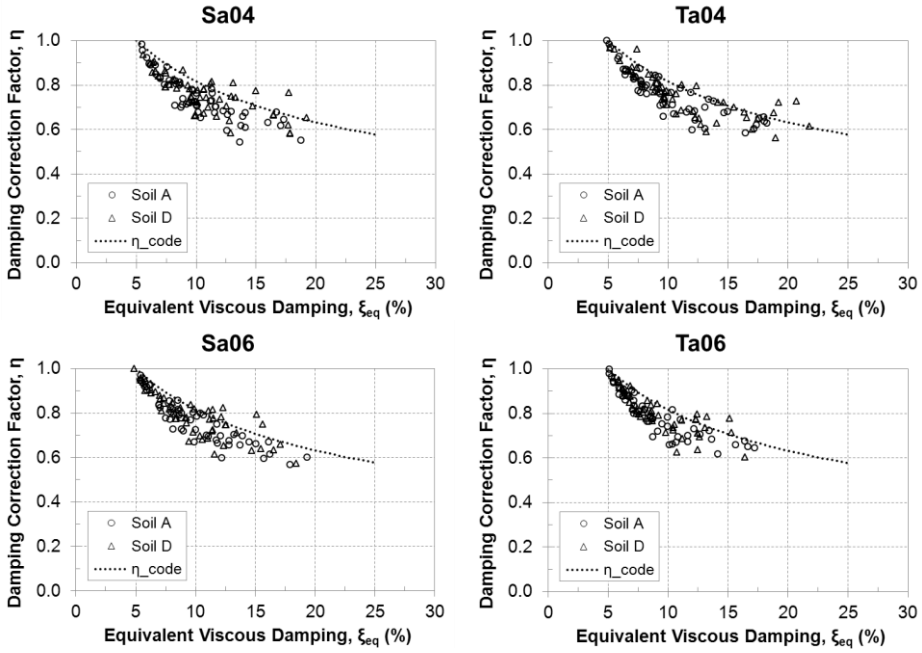

Fig. 5.8 Damping Correction Factor versus Equivalent Viscous Damping. Squat specimens with pre-load corresponding to 0.4 N/mm^2 (above) and 0.6 N/mm^2 (below).

Specimen	R^2 – Soil A	R^2 – Soil D
SRSa 0.4	0.201	0.437
TRSa 0.4	0.566	0.676
SRSa 0.6	0.587	0.681
TRSa 0.6	0.716	0.726
SRSb 0.4	0.039	0.504
TRSb 0.4	-0.256	0.553
SRSb 0.6	0.168	0.472
TRSb 0.6	0.278	0.684

Table 5.3 Coefficient of determination for Damping Correction Factor using α = 5.

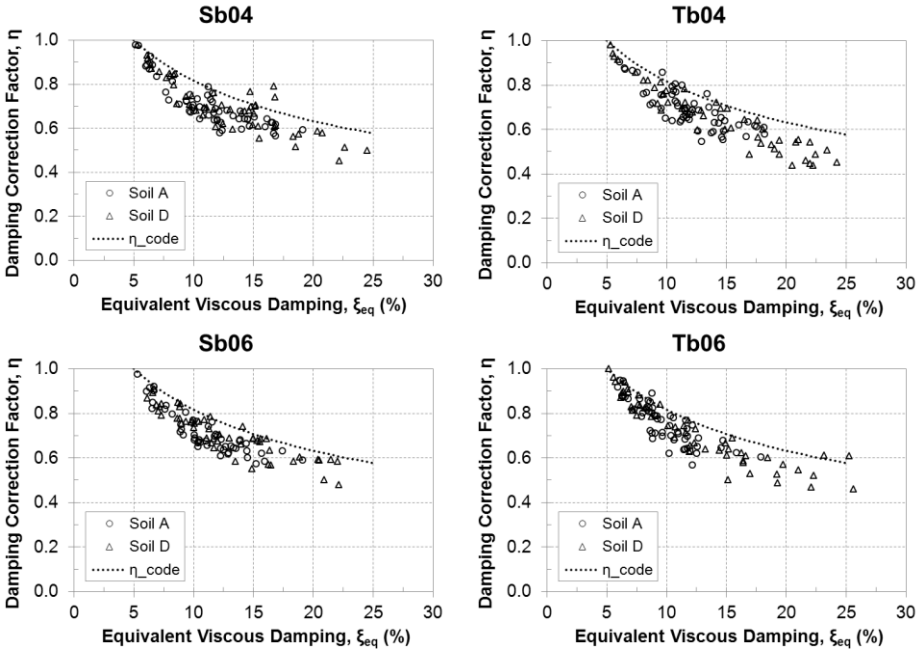

Fig. 5.9 Damping Correction Factor versus Equivalent Viscous Damping. Slender specimens with pre-load corresponding to 0.4 N/mm^2 (above) and 0.6 N/mm^2 (below).

5.4.2 Injected Stone Masonry (SM)

5.4.2.1 Equivalent Viscous Damping

In Fig. 5.10 and Fig. 5.11 the results of the procedure for strengthened masonry walls are presented, divided for soil type. Squat specimens are represented with continuous lines and square indicators, whereas slender specimens are represented with dashed lines and triangular indicators. Furthermore, panels tested under 2.0 N/mm^2 are indicated in red and blue, whereas panels tested under 1.0 N/mm^2 are indicated in orange and light blue. It can be noticed that panels in same condition (pre-load and aspect ratio) give very similar results.

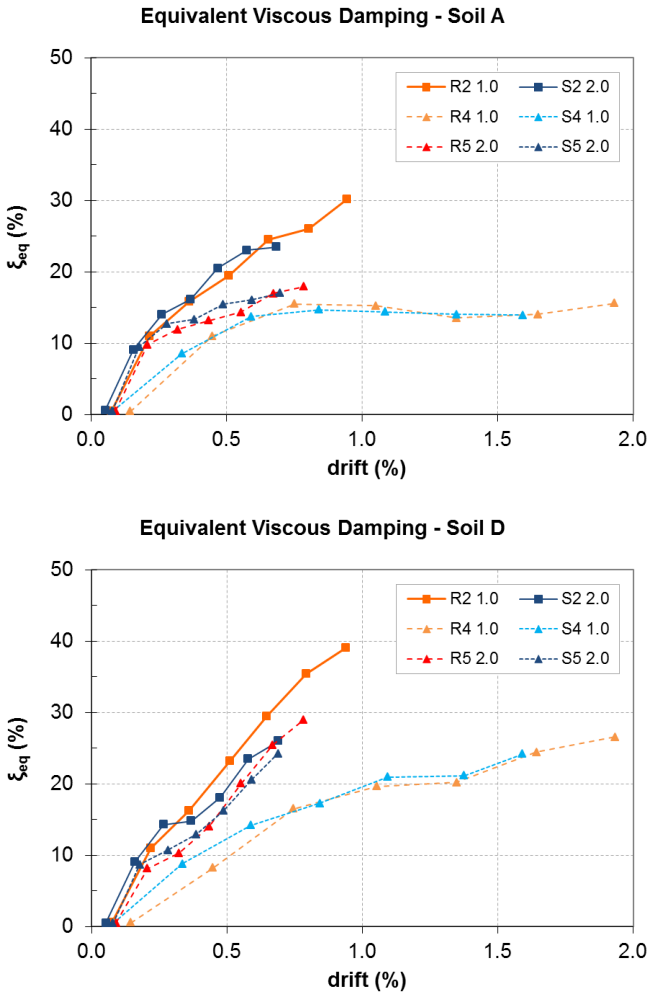

Fig. 5.10 Equivalent Viscous Damping versus Drift curves.
Experimental SM walls under soil type A (above) type D (below).

The obtained damping values are very high, probably due to high vertical pre-load applied. Indeed, to force shear behaviour, it has been applied a vertical stress equal to 15% and 30% of compressive strength. However, it is possible to say that squat specimens show higher values, about 25% for both soil types. Slender specimens, instead, show similar values for soil D (about 20-25%), whereas for soil A lower values have been obtained (about 17%).

The same results, but adimensioning the displacement respect to second limit state (d_{cr}), are shown in Fig. 5.11. It can be noticed that in this way the curves are closer to each other, especially in the first phase.

Regarding the period shift (Table 5.4), it is possible to say that all panels remain in the plateau of spectra, with the exception of slender panels on soil A. These panels attain constant values of damping on soil A, whereas on soil D, as other panels on both soils, show always ascending values.

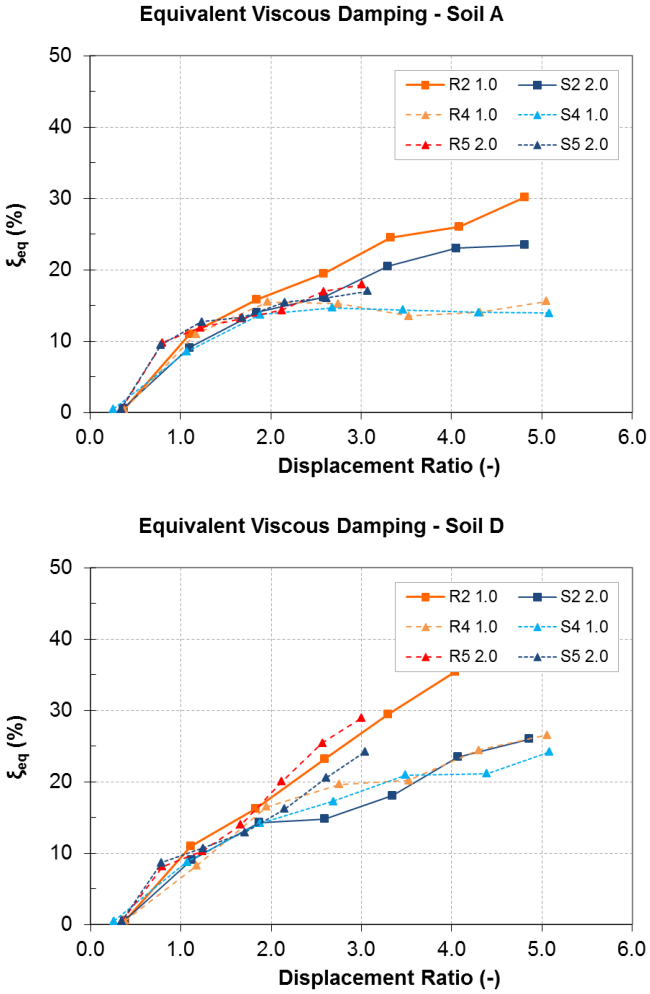

Fig. 5.11 Equivalent Viscous Damping versus Displacement Ratio curves. Experimental SM walls under soil type A (above) type D (below).

Squat walls	T_{EL} (s)	T_U (s)
R2 1.0	0.11	0.39
S2 2.0	0.14	0.40
mean	*0.13*	*0.40*

Slender walls	T_{EL} (s)	T_U (s)
R4 1.0	0.18	0.63
S4 1.0	0.16	0.57
R5 2.0	0.20	0.53
S5 2.0	0.20	0.48
Mean	*0.18*	*0.55*

Table 5.4 Period Shift for Strengthened Masonry

5.4.2.2 Relationship between Elastic and Inelastic displacement

Fig. 5.12 and Fig. 5.13 show the ratio between elastic and inelastic displacement. The relationship between d_{EL} and d_{IN}, for this type of masonry, seems to be very similar to already observed for reinforced masonry. So, the considerations explained in § 5.4.1.2, regarding the grid's axes, are still valid. In addition, it has been used again the function type expressed by (Eq. 5.2) for the regression analyses.

For squat specimen tested under 1.0 N/mm^2 of pre-load, the obtained regression curves are almost superimposed. For specimen tested under 2.0 N/mm^2 of pre-load, the curves diverge. In this case, curve for soil A is above that obtained for soil D.

For slender specimens different results have been obtained. Indeed, at high level of pre-load, the regression curves for both soils are almost superimposed. On the contrary, at low level of pre-load, they diverge. In this case, as for reinforced masonry, curves for soil D are above the one's obtained for soil A.

Values of obtained regression functions are reported in Table 5.5. Also in this case, the chosen power function is able to approximate very well the trend of ratio between d_{EL} and d_{IN}. Indeed the values of coefficient of determination R^2 are very high, all of them are greater than 0.95.

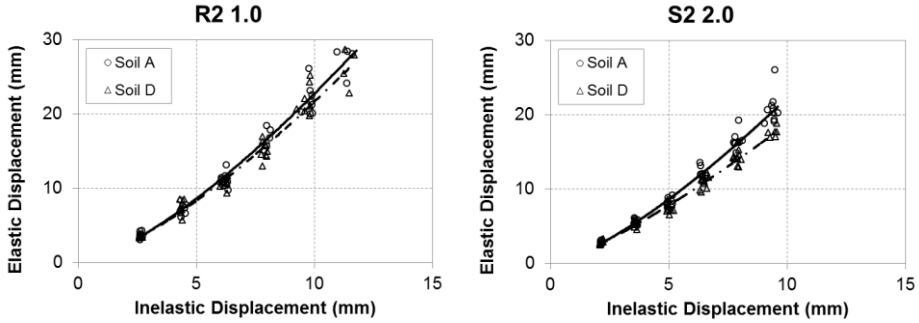

Fig. 5.12 Elastic displacement versus Inelastic displacement. Squat specimens with pre-load corresponding to 1.0 N/mm^2 (left) and 2.0 N/mm^2 (right).

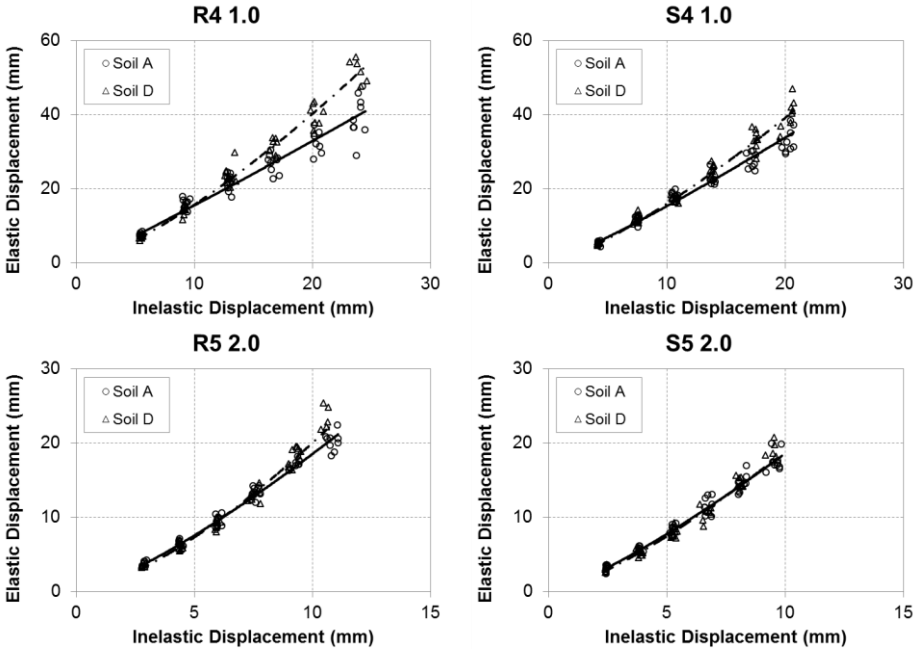

Fig. 5.13 Elastic displacement versus Inelastic displacement. Slender specimens with pre-load corresponding to 1.0 N/mm^2 (above) and 2.0 N/mm^2 (below).

Squat walls	β Soil A	γ Soil A	R^2	β Soil D	γ Soil D	R^2
R2 1.0	0.907	1.400	0.984	0.902	1.381	0.978
S2 2.0	0.966	1.363	0.986	1.034	1.260	0.983
mean	*0.937*	*1.382*		*0.968*	*1.321*	
Slender walls	β Soil A	γ Soil A	R^2	β Soil D	γ Soil D	R^2
R4 1.0	1.279	1.084	0.955	0.689	1.359	0.982
S4 1.0	1.102	1.143	0.972	0.817	1.292	0.989
R5 2.0	0.945	1.293	0.987	0.707	1.453	0.984
S5 2.0	1.024	1.260	0.981	0.864	1.341	0.980
Mean	*1.088*	*1.195*		*0.769*	*1.361*	

Table 5.5 Regression functions for ratio between d_{EL} and d_{IN}: β and γ coefficients and coefficient of determination R^2.

5.4.2.3 Damping Correction Factor

In Fig. 5.14 and Fig. 5.15 the relationship between Damping Correction Factor and ξ_{eq} are shown. In these graphs, as already done for RM, the code recommended formulation for η is plotted. It can be say that there are little differences between effective η for soil A and soil D. More precisely, results for soil A (circular indicators) are lightly lower respect to those obtained for soil D (triangular indicators). In any case, for both soils, the majority of effective η are below code recommended values, that means that Damping Correction Factor is overestimated.

The poor ability of code recommended formulation to approximate the effective η can be seen also in Table 5.6. In this table the values of R^2 obtained using α equal to 5 are showed. As can be seen, very low values have been obtained, all lower than 0.6. For soil A and slender walls, even negative values have been gained. Since the trend of effective η seems to be well correlated with the function expressed by (Eq. 5.3), a calibration of coefficient α can give a reliable estimation of Damping Correction Factor.

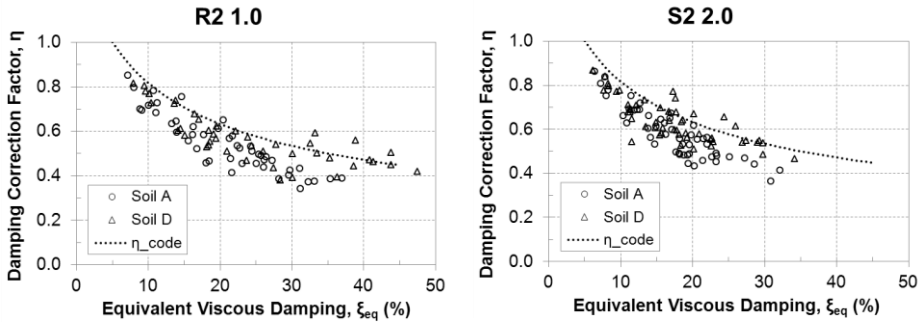

Fig. 5.14 Damping Correction Factor versus Equivalent Viscous Damping. Squat specimens with pre-load corresponding to 1.0 N/mm^2 (left) and 2.0 N/mm^2 (right).

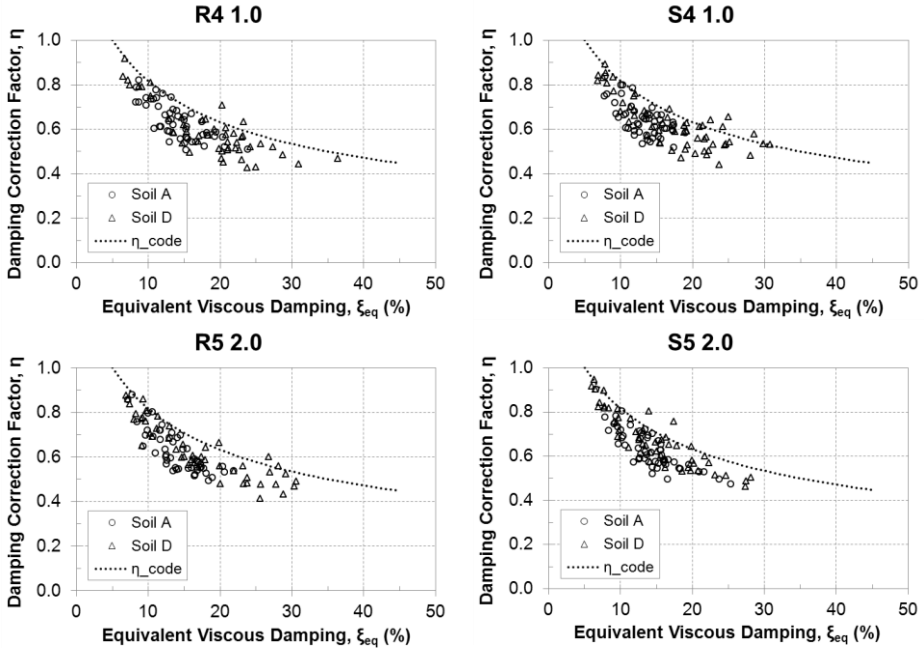

Fig. 5.15 Damping Correction Factor versus Equivalent Viscous Damping. Slender specimens with pre-load corresponding to 1.0 N/mm^2 (above) and 2.0 N/mm^2 (below).

Specimen	R^2 – Soil A	R^2 – Soil D
R2 1.0	0.201	0.591
S2 2.0	0.008	0.318
R4 1.0	-0.872	0.332
S4 1.0	-0.786	0.379
R5 2.0	-0.695	0.558
S5 2.0	-0.292	0.587

Table 5.6 Coefficient of determination for Damping Correction Factor using α = 5.

5.5 Sensitivity Analysis

5.5.1 Motivations of the Sensitivity Analysis

The model used in the procedure is described in the chapter 4. The input data for the model are the four limit states, C_1 and C_2 coefficients and the equivalent mass *m**. The latter is obtained by (Eq. 5.4), where σ_0 is the vertical stress, *b* and *t* are the base dimensions and *g* is the gravity acceleration. This means that *m** represents the mass that should be applied to a panel with the same dimensions in order to obtain a vertical stress equal to σ_0. Several sets of these parameters are considered, one for each experimental test. So the procedure can be applied to models that represent the same conditions (geometry and pre-load) at which shear-compression tests have been performed.

$$m^* = {}^{\sigma_0}/_{(b \cdot t) \cdot g} \qquad \textit{(Eq. 5.4)}$$

The four LS are determined as described in §3.2.3 and *m** is directly obtained starting from geometric dimensions of walls and pre-load level applied. So these values can be considered as exact, i.e., they can be exactly evaluated for a wall once the geometry is known and idealized envelope of its in-plane behaviour is given. Two coefficients C_1 and C_2 (C coefficients), instead, are calculated by imposing the equality of the input energy and the dissipated energy between experimental and modelled loops. This equality is imposed for each cycle, so, for each panel, one couple of coefficients is obtained for each cycle. As described in §4.3.1, the use of parameter Z enables to obtain almost constant values of coefficients C for the several cycles. Hence, it is reasonable to consider that the model could use the average of these values in the analyses, without sensitive loss of quality in the simulation of hysteretic behaviour.

It is important to point out that, given the quadri-linear envelope curve, the quality of modelling is strictly related to the values of these coefficients, on which the quantity of input and, specially, dissipated energy depends. In Table 4.1 the values of C coefficients and their coefficients of variation are reported. As can be seen, the values of COVs are generally low, but not zero. Since hysteretic damping depends on the energy dissipated by the structure, and energy is defined by means of C_1 and C_2, it is clear that the use of approximate values for these coefficients, introduces an error on the estimation of damping. From these considerations, the importance of performing a sensitivity analysis, in order to assess how much the variation of C coefficients influences the values of damping obtained from the procedure has arisen.

5.5.2 Methodology and Results

In general, COV for C_1 varies between 5% and 20%, whereas for C_2 this range is included between 2% and 10% (Table 4.1). The mean value of COV for C_1 is 14% and for C_2 is 6%. Hence, it can be said that the variation of C_1 is about twice compared to that of C_2. For this reason, it has been chosen to consider the following ranges of variability: ±10% with step 5% and ±5% with step 2.5%, for C_1 and C_2 respectively. In such a way, the total number of combinations is 25. The influence of the variability of C coefficients on the damping can be different when considering the different failure modes and soil types. So, it has been chosen to repeat the sensitivity analysis for two panels, one for each failure mode, and for two ground types. The chosen panels are Sa06 and Tb06, representative of shear and flexural behaviour respectively.

The results of the analysis show that:

- The values of damping related to first target displacement (d_t, described in §5.2) are not affected by the variability of C coefficients. This is reasonable, since the first d_t is placed just beyond elastic limit. In the elastic phase, there is no energy dissipation by hysteresis, so the value of damping obtained at the first d_t is in any case close to the elastic component (set to 0.5%), independently by the variability of the coefficients.
- The values of damping related to second target displacement are the most affected by the variability of C coefficients. It is important to point out that this d_t is always placed between the first two LSs, i.e. flexural and critical limit states. The unloading phase between these LSs is characterized by a quite high stiffness, close to the elastic one. This means that the opening of hysteretic cycles is not so wide. So, the amount of dissipated energy is relatively small, and strongly affected by the values of C coefficients.

- From the third target displacement, the sensitivity of damping, related to the variability of C coefficients, starts decreasing with the increase of target displacements. So, the greater is the d_t, the lower is the variability.

Fig. 5.16 shows the obtained results, at the third d_t, for the panels characterized by shear and flexural failure on A and D type soils. The results are expressed in terms of relative difference of damping values obtained using several variations of C coefficients. In general, damping decreases with the increase of C_2 coefficient, and increases with the increase of C_1 coefficient. No significant differences can be noticed between the two soil types. The flexural failure mode shows greater sensitivity to variability of C coefficients, than the shear failure.

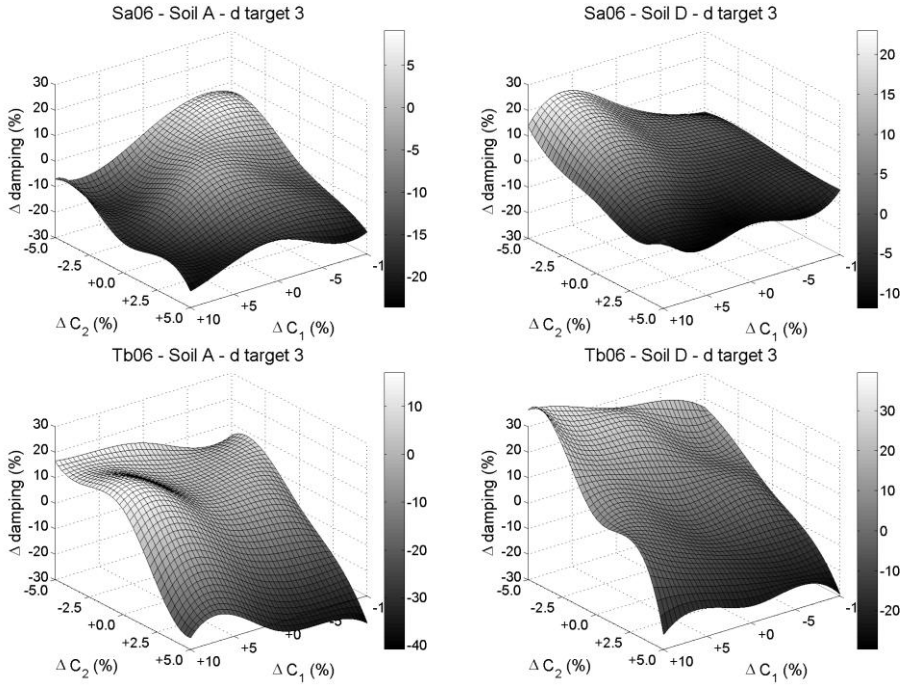

Fig. 5.16 Sensitivity of damping, express as relative difference, versus coefficients C variability. Shear failure (above) and flexural failure (below) on soil type A (left) and D (right).

In order to quantify the sensitivity of damping, a linearization of results has been performed. More precisely, for each coefficient, a linear regression of the results has been done, considering the other coefficient as a constant. Furthermore, the variability of each coefficient has been divided in two parts: from zero to negative limit, and from zero to positive limit. The results of this analysis are shown in Table 5.7 and Table 5.8, for shear and flexural failure respectively. The values obtained at the first two target displacements for the shear panel and considering a positive

variation of coefficient C_1 are not taken into account. Indeed, in general the value of coefficient C_1 is less than ratio between H_1 and H_{max}, so point A is placed in the first branch of quadri-linear envelope curve (Fig. 4.3). On the contrary, for this panel, the value of C_1 is slightly greater than ratio H_1/H_{max}, and this means that point A is initially placed in the second branch of envelope curve. In any case, during a dynamic analysis, the parameter Z reduces the ordinate of point A for increasing displacements (Eq. 4.5). However, for little displacements, parameter Z is set to one, that means that it does not affects the determination of point A. Considering, at the first target displacements, a variation of +10% for C_1 coefficient, imply the positioning of point A in the second branch of envelope curve. This fact provides disagreeing results, compared with the others, and so they cannot be considered reliable.

It can be noticed that, considering C_1 as a constant, a variation of -5% of C_2 coefficient involves a difference of about 6% and 12% of the values of damping, for shear and flexural failure modes respectively. The opposite variation (+5%) of the same coefficient involves more or less the opposite differences in terms of damping, namely -7% and -20%. On the other hand, considering C_2 as constant, a variation of -10% of C_1 coefficient involves a difference of about -2.5% (shear) and -6% (flexural) on the values of damping. The opposite variation (+10%) of the same coefficient produces a difference, in terms of damping value, of about +2% (shear) and +7% (flexural).

These values of relative difference can appear to be too high, but it is important to point out that, for each damping curve, the first and the last values of damping are the less affected by the variability of C coefficients. Hence, the initial value (close to elastic component) and the final value, can be considered reliable. Furthermore, the fact that similar conditions, in terms of aspect ratio and preload level, give similar values of damping, ensure the reliability of obtained results on the whole range of displacement capacity.

	C1 = cost				C2 = cost			
	ΔC2 = -5%		ΔC2 = +5%		ΔC_1 = -10%		ΔC_1 = +10%	
d_t	soil A	soil D	soil A	soil D	soil A	soil D	soil A	soil D
1	-0.2%	-2.1%	-2.0%	-2.6%	0.3%	0.8%	-	-
2	17.8%	24.2%	-16.7%	-14.7%	5.8%	0.0%	-	-
3	7.6%	10.1%	-11.3%	-7.2%	-2.2%	-3.3%	-9.6%	0.3%
4	3.3%	3.1%	-6.7%	-6.0%	-4.8%	0.0%	-6.6%	1.7%
5	7.0%	4.1%	-4.3%	-5.9%	-4.6%	-4.8%	6.2%	1.3%
6	3.4%	3.5%	-6.3%	-3.5%	-7.1%	-6.4%	5.0%	5.2%
7	4.7%	3.2%	-4.0%	-3.0%	-3.6%	-4.5%	4.4%	9.5%
mean	*6.4%*		*-6.7%*		*-2.5%*		*+1.7%*	

Table 5.7 Results of regression analysis on relative difference between damping values obtained varying coefficients C. Panel Sa06, characterized by shear failure.

	C1 = cost				C2 = cost			
	ΔC2 = -5%		ΔC2 = +5%		ΔC_1 = -10%		ΔC_1 = +10%	
d_t	soil A	soil D	soil A	soil D	soil A	soil D	soil A	soil D
1	-0.1%	-0.4%	1.4%	-0.7%	0.0%	0.0%	-6.1%	14.9%
2	28.6%	16.8%	-47.8%	-41.6%	-11.1%	-4.5%	10.2%	6.7%
3	8.7%	24.2%	-33.8%	-26.5%	-6.0%	-6.7%	7.1%	8.8%
4	15.7%	15.9%	-23.9%	-14.9%	-4.8%	-4.6%	5.9%	8.3%
5	14.6%	10.2%	-18.7%	-13.2%	-6.2%	-17.4%	7.0%	5.5%
6	12.1%	5.4%	-14.4%	-13.9%	-7.7%	-10.7%	9.9%	8.3%
7	4.9%	4.5%	-18.2%	-8.8%	-4.0%	3.0%	6.4%	6.0%
mean	*11.5%*		*-19.6%*		*-5.8%*		*7.1%*	

Table 5.8 Results of regression analysis on relative difference between damping values obtained varying coefficients C. Panel Tb06, characterized by flexural failure.

5.6 Summary and Conclusions

A procedure for determination of Equivalent Viscous Damping has been developed. This procedure makes use of dynamic analyses, based on an on-purpose hysteretic model, and of equivalent linear system. Two ground types, and 10 spectrum-compatibles synthetic time-histories for each soil type, have been taken into account.

A first analysis of the results allows to gather the following conclusions:

- Equivalent Viscous Damping shows an increasing trend that can be considered as logarithmic. Indeed, damping increases with increasing displacements, when period corresponding to secant stiffness is included in spectrum plateau. Otherwise damping can be considered constant.
- At the same drift level, a shear type of behaviour involves higher values of damping than a flexural behaviour. Hence, in general, squat panels are characterized by higher values of damping than those of slender walls. When displacement is a-dimensionalized to d_{cr}, it is possible to obtain damping curves that are closer to each other, although they are obtained for different failure modes.
- Squat panels, that have a period shift included in spectra plateau of both soils A and D, give similar values of damping for the different ground types. On the contrary, slender walls show an appreciable difference related soil type, since the period shift of these panels is included in spectra plateau only for soil D. In this case, lower values are obtained with soil A compared to soil D.
- Relationship between elastic and inelastic displacement is more than proportional. A good approximation of numerical results can be obtain using a

power function. In such a way, very high values of R^2 have been obtained. For the majority of panels of both masonry systems there are not significant differences between soil types. If any, soil D curves are lightly above those of soil A.

- Values of effective Damping Correction Factor are well correlated with code proposed formulation. Furthermore, it seems that differences between various soil types for RM are not significant. For SM, instead, different values are obtained considering different soil types. Damping Correction Factor is lower for soil A than for soil D. In any case, for both RM and SM, code formulations overestimate the real ratio between inelastic and elastic displacement. For these reasons, a calibration of expression (Eq. 5.3) is needed.

6 ANALYSIS OF RESULTS

6.1 Introduction

This chapter presents and discusses the results of the analyses. For both types of masonry taken into account, and for each specimen, values of ξ_{eq} are reported and commented. Furthermore, a comparison between the results obtained with the proposed methodology and the Gulkan & Sozen approach is carried out.

Another important result of analyses is represented by the relationship between inelastic and elastic displacement, i.e. the η factor. This factor is defined in function of ξ_{eq} in several regulations. Existing code formulations are taken into account and compared with obtained numerical results.

6.2 Reinforced Masonry System

6.2.1 Equivalent Viscous Damping

Fig. 6.1 and Fig. 6.2 show the comparison between proposed procedure (black indicators) and Gulkan and Sozen (gray indicators) values of ξ_{eq}. In these graphs the regression functions obtained using the least square method are also shown. The type of function used for regression analysis is represented by:

$$\xi_{eq} = \alpha + \beta \cdot ln(\Psi) \qquad \textit{(Eq. 6.1)}$$

where Ψ is drift expressed in percentage. The functions related to proposed procedure are plotted in continuous line, those related to Gulkan and Sozen (G&S) procedure are plotted in dashed line. As can be seen, the values obtained with proposed procedure are more scattered than those obtained with G&S procedure. This means that approximation quality of regression functions is greater for G&S than for our procedure. Indeed, coefficients of determination obtained for the procedure range between 0.74 and 0.88 (Table 6.1), whereas for G&S these coefficients are always greater than 0.85 (Table 6.2). In any case, the function

expressed by (Eq. 6.1) is able to represent with sufficient accuracy the effective trend of results for both approaches.

Furthermore, the use of analytical function to approximate numerical results, allows to calculate the mean integral value of damping. In general, damping values obtained with G&S are lower than those obtained with our procedure. For soil type A the difference can be considered negligible, because its mean value is about 5%. For soil D, instead, the difference is greater, about 15%. These differences are more marked for slender walls, for some of them are greater than 20%.

Squat walls	α Soil A	β Soil A	R^2	α Soil D	β Soil D	R^2
SRSa 0.4	12.266	4.780	0.758	12.818	5.114	0.779
TRSa 0.4	12.669	4.770	0.793	13.538	5.124	0.772
SRSa 0.6	13.438	5.021	0.750	13.177	4.970	0.771
TRSa 0.6	13.217	5.371	0.743	13.066	5.261	0.792
mean	*12.897*	*4.986*		*13.150*	*5.117*	
Slender walls	β Soil A	γ Soil A	R^2	β Soil D	γ Soil D	R^2
SRSb 0.4	9.819	3.762	0.823	11.925	4.975	0.828
TRSb 0.4	9.543	3.835	0.762	12.002	6.064	0.878
SRSb 0.6	11.322	4.202	0.841	13.331	5.222	0.778
TRSb 0.6	8.489	3.227	0.763	11.736	5.399	0.756
Mean	*9.793*	*3.757*		*12.249*	*5.415*	

Table 6.1 Regression functions for ξ_{eq} (procedure) vs Ψ: α and β coefficients and coefficient of determination R^2.

Squat walls	α Soil A	β Soil A	R^2	α Soil D	β Soil D	R^2
SRSa 0.4	11.997	4.882	0.983	12.249	5.144	0.962
TRSa 0.4	10.981	4.121	0.961	11.449	4.328	0.952
SRSa 0.6	12.267	4.659	0.970	12.678	4.860	0.956
TRSa 0.6	11.130	4.689	0.958	11.022	4.663	0.954
mean	*11.594*	*4.588*		*11.850*	*4.749*	
Slender walls	β Soil A	γ Soil A	R^2	β Soil D	γ Soil D	R^2
SRSb 0.4	11.997	4.882	0.983	12.249	5.144	0.962
TRSb 0.4	10.981	4.121	0.961	11.449	4.328	0.952
SRSb 0.6	12.267	4.659	0.970	12.678	4.860	0.956
TRSb 0.6	11.130	4.689	0.958	11.022	4.663	0.954
Mean	*11.594*	*4.588*		*11.850*	*4.749*	

Table 6.2 Regression functions for ξ_{eq} (Gulkan and Sozen) vs Ψ: α and β coefficients and coefficient of determination R^2.

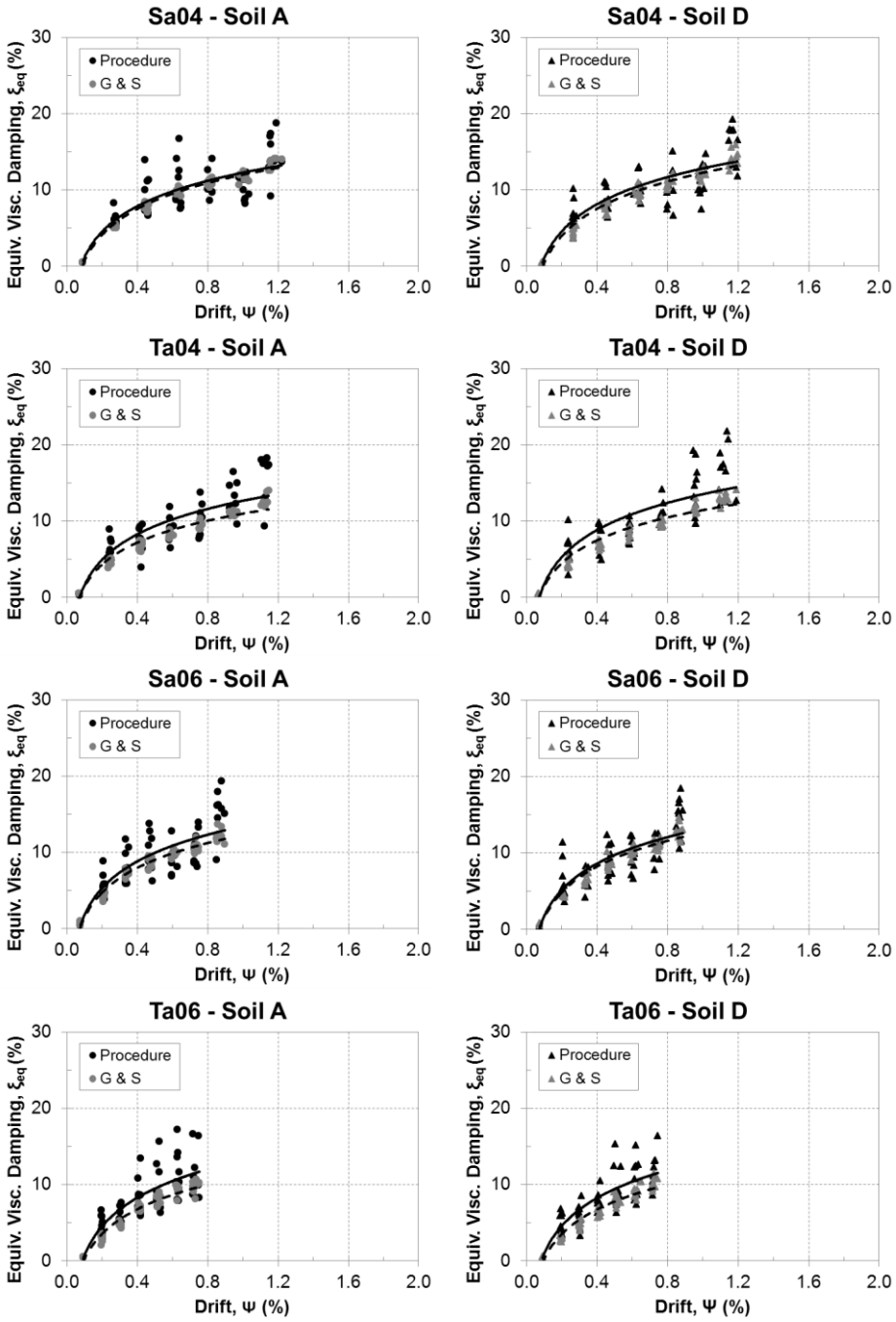

Fig. 6.1 Comparison between proposed procedure and Gulkan and Sozen values of ξ_{eq}. Squat specimens under soil type A (on the left) and D (on the right).

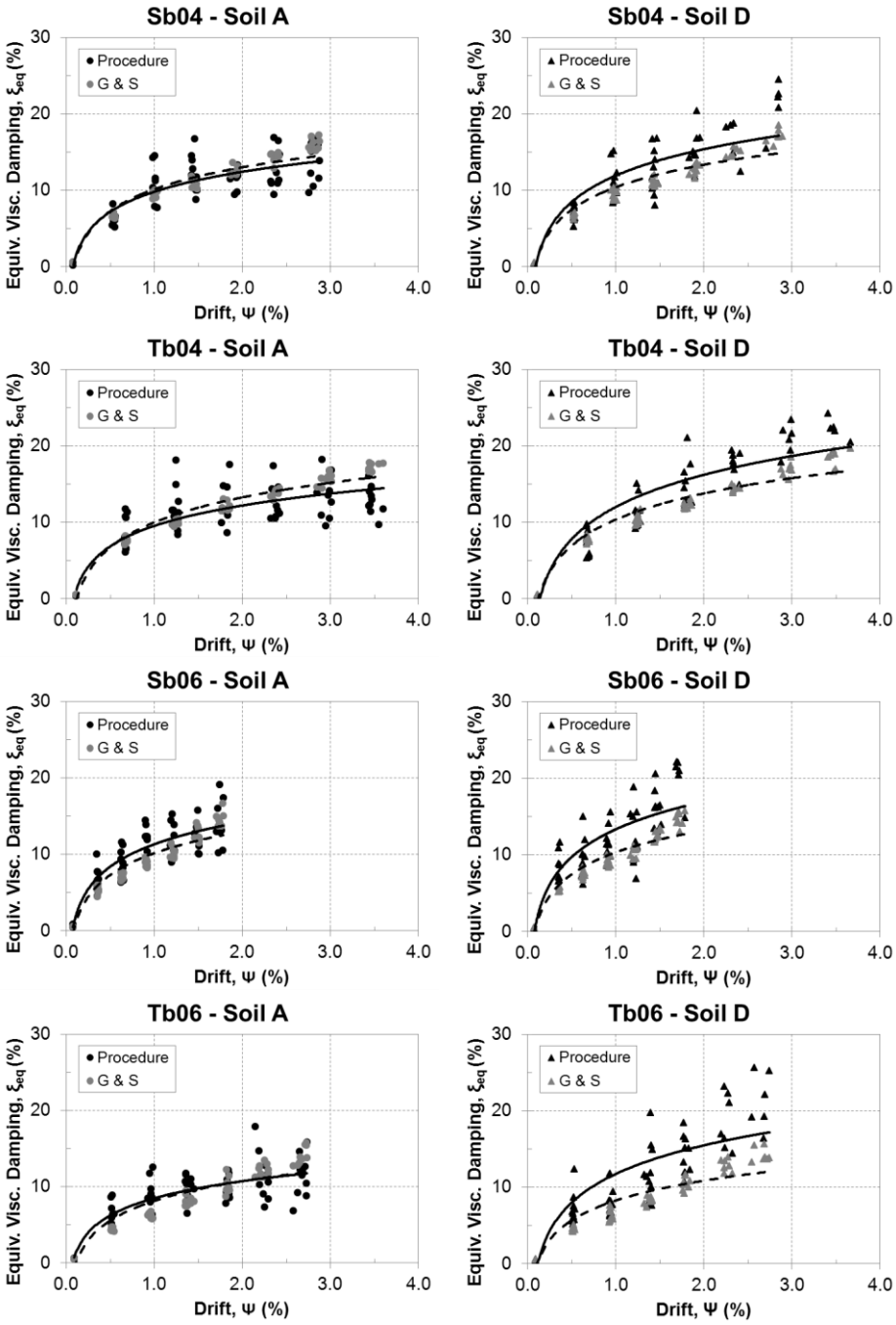

Fig. 6.2 Comparison between proposed procedure and Gulkan and Sozen values of ξ_{eq}. Slender specimens under soil type A (on the left) and D (on the right).

Furthermore, it can be noticed that G&S approach leads to no sensitive difference between soil types. Indeed, the relative differences between soil D and A are lower that +5% for all the panels, with a mean value of about +2%. From the physical point of view, two approaches should lead to the same results, given the validity of equal velocity assumption. Indeed, whereas G&S approach computes the damping by imposing the equality of dissipated energy by the inelastic and equivalent elastic systems, through the assumption of equal relative velocity of both systems (§2.4.3), our procedure imposes directly the equality of displacements, which implies the energy equality. Since the validity of equal velocity hypothesis has not been proven, and also that the aim of equivalent viscous damping is to give the same peak displacements as the hysteretic response by an equivalent linear system, the results of our procedure seem to be more reliable.

The coefficients obtained by regression analysis, and listed in Table 6.1, have been used to plot all the damping curves in one graph only, for each soil type. Fig. 6.3 shows these graphs. As can be seen, for soil A all the panels reach a value of damping of about 13% at ultimate displacement. While shear panels have a maximum drift level of about 0.8-1.2%, flexural panels have greater displacement capacity, with an ultimate drift of about 2.0-3.0%. So flexural curves are below the shear ones.

For soil D, instead, shear and flexural curves are superimposed until the maximum displacement for shear panels. Beyond this point, flexural curves continue to increase, reaching a maximum value of damping of about 17%.

The coefficients α and β in Table 6.1 and Table 6.2 are referred to damping versus drift. They can be also referred in function of displacement ratio, considering the logarithmic properties. In other words, is possible to use (Eq. 6.2) in order to describe the functions shown in Fig. 6.3.

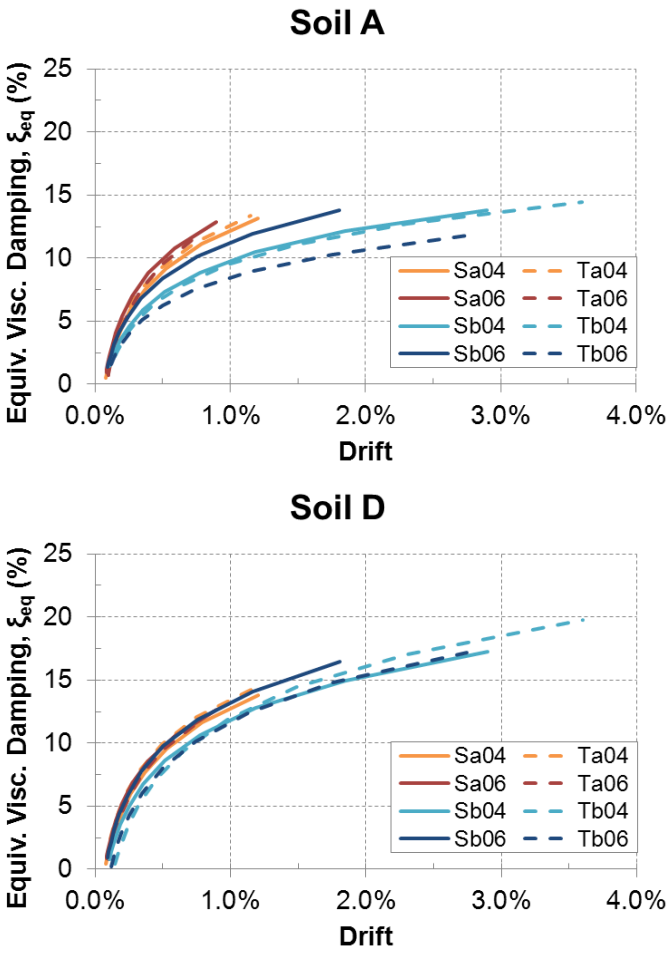

Fig. 6.3 Equivalent Viscous Damping versus Drift curves.
Experimental RM walls under soil type A (above) type D (below).

$$\xi_{eq} = \alpha_{DR} + \beta_{DR} \cdot ln(DR) \qquad \textit{(Eq. 6.2)}$$

Change of variables is expressed by following expressions:

$$\beta_{DR} = \beta_{\Psi} \qquad \textit{(Eq. 6.3)}$$

$$\alpha_{DR} = \alpha_{\Psi} + \beta_{\Psi} \cdot ln(\Psi_{cr}) \qquad \textit{(Eq. 6.4)}$$

where subscript DR indicates a coefficient referred to displacement ratio, and subscript Ψ indicates a coefficient referred to drift. Ψ_{cr} is drift at critical limit state. The value of coefficient of determination remains the same.

Fig. 6.4 shows the same curves of Fig. 6.3, but expressed in function of displacement ratio (DR), that is displacement a-dimensionalised to the second limit state, i.e. d/d_{cr}. It is interesting to notice that, in this case, for soil A, curves for both failure modes are almost superimposed, whereas for soil D, flexural curves are above those for soil A. The reason of this is connected to the similar values of ultimate DRs for the two failure modes. Indeed, ultimate drift for flexural failure is almost three times ultimate drift for shear failure, whereas ultimate flexural DR is slightly greater than that for shear failure. This means that curves of both failure modes are stretched in a similar range.

Observing results obtained for two soils considered, it is possible to say that there are no significant differences between damping for both soils for what concern shear walls. Indeed, for both soil types, damping curves for these panels reach values of about 13%. For each panel, the relative difference between obtained values for different soils, is generally lower than 5%. So it can be said that equivalent viscous damping for shear walls is not influenced by soil type. It cannot be said the same for flexural walls. These panels reach the same damping values of shear panels, at maximum displacement, for soil A, i.e. about 13%. Nevertheless, damping curves for soil D increase until values of about 17%. Hence, flexural panels give damping curves for soil D greater by 30% compared to those obtained for soil A.

It can be noticed that damping curves for the same failure mode and same soil are close to each other. This means that different level of pre-load do not influence the damping, although the studied range is quite limited: 0.4 N/mm^2, orange (shear) and light blue (flexural) curves, 0.6 N/mm^2, red (shear) and blue (flexural) curves. This means that the most significant parameters, for defining damping of reinforced masonry structures, are failure mode and soil type. For this reason, a new regression analysis has been performed, distinguishing the results only between the mentioned parameters. The points clouds and corresponding regression curves are shown in Fig. 6.5 and Fig. 6.6, related to drift and displacement ratio, respectively. Red and square indicators are related to panels that failed in shear, whereas blue and circular indicators are related to panels that have flexural failure. Obtained regression functions are also shown, in red for shear failure and in blue for flexural failure.

The obtained regression functions are described by (Eq. 6.5), (Eq. 6.6), (Eq. 6.7) and (Eq. 6.8). These equations have a coefficient of determination R^2 that ranges between 0.75 and 0.80. This means that the quality of approximation does not decrease if the regression analysis is performed on all the panels characterized by the same failure mode. Indeed, as above mentioned, the coefficient R^2 varies between 0.7 and 0.9 performing the analysis separately for each panel.

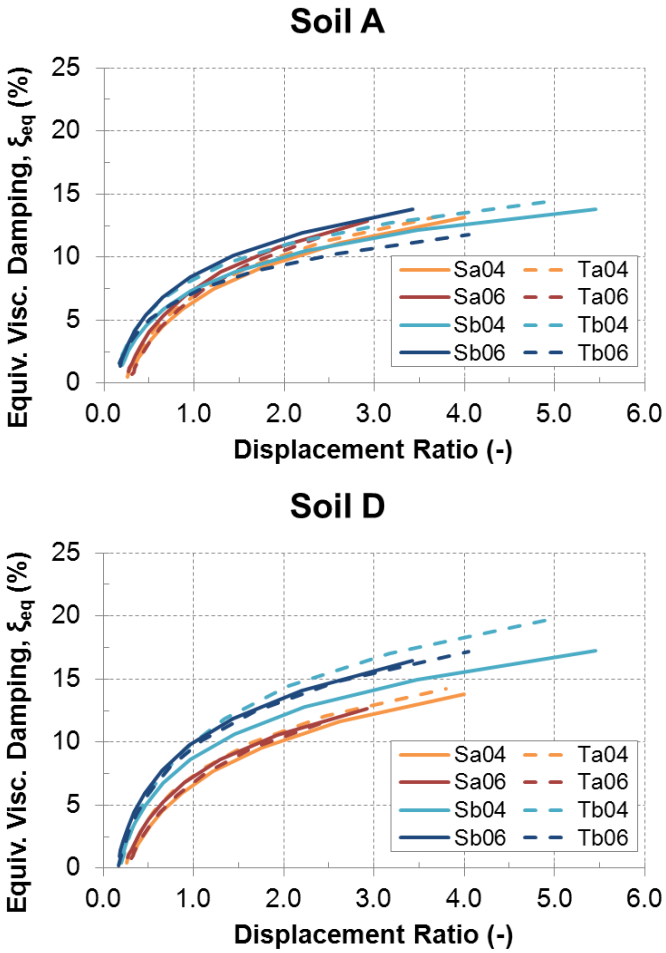

Fig. 6.4 Equivalent Viscous Damping versus DR curves.
Experimental RM walls under soil type A (above) type D (below).

The regression functions are compared to each other in Fig. 6.7. Curves for shear failure are plotted in red, those for flexural failure in blue. Continuous line is used for soil A and dashed line for soil D. As can be seen, there are no differences between soil types for shear behaviour. Indeed, considering the graphs related to both drift and displacement ratio, red curves are almost perfectly superimposed. On the contrary, flexural behaviour involves rather different damping values, according to soil type. The curves for soil D, related to both drift and displacement ratio, are almost 30% greater than those related to soil A.

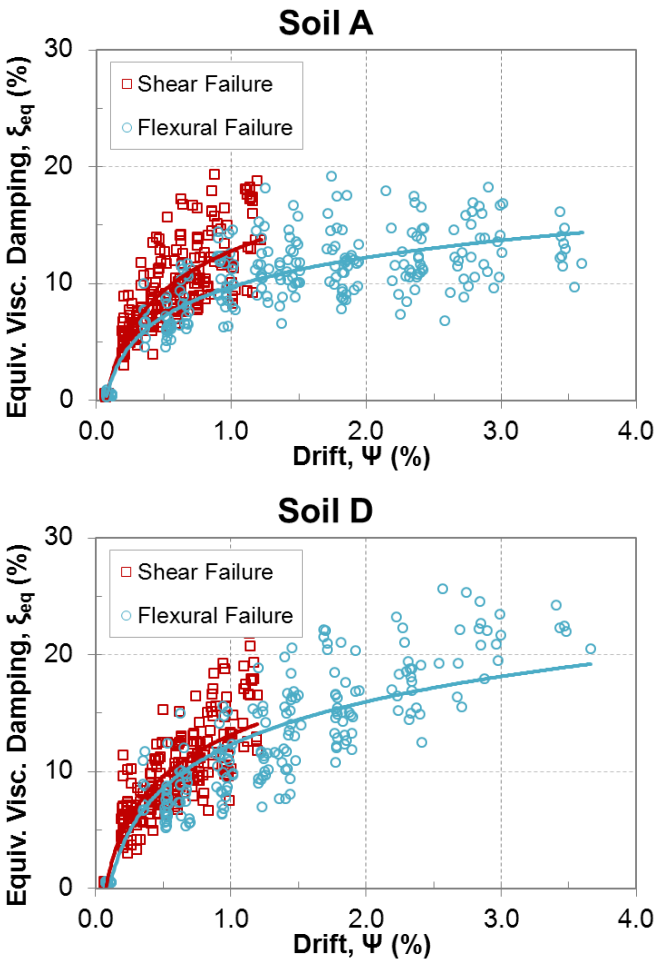

Fig. 6.5 Regression functions, related to drift, for the two failure modes. Soil type A (above) and type D (below).

Shear – Soil A $\xi_{eq} = 12.795 + 4.903 \cdot ln(\Psi)$ *(Eq. 6.5)*

Flexural – Soil A $\xi_{eq} = 9.709 + 3.621 \cdot ln(\Psi)$ *(Eq. 6.6)*

Shear – Soil D $\xi_{eq} = 13.139 + 5.108 \cdot ln(\Psi)$ *(Eq. 6.7)*

Flexural – Soil D $\xi_{eq} = 12.284 + 5.323 \cdot ln(\Psi)$ *(Eq. 6.8)*

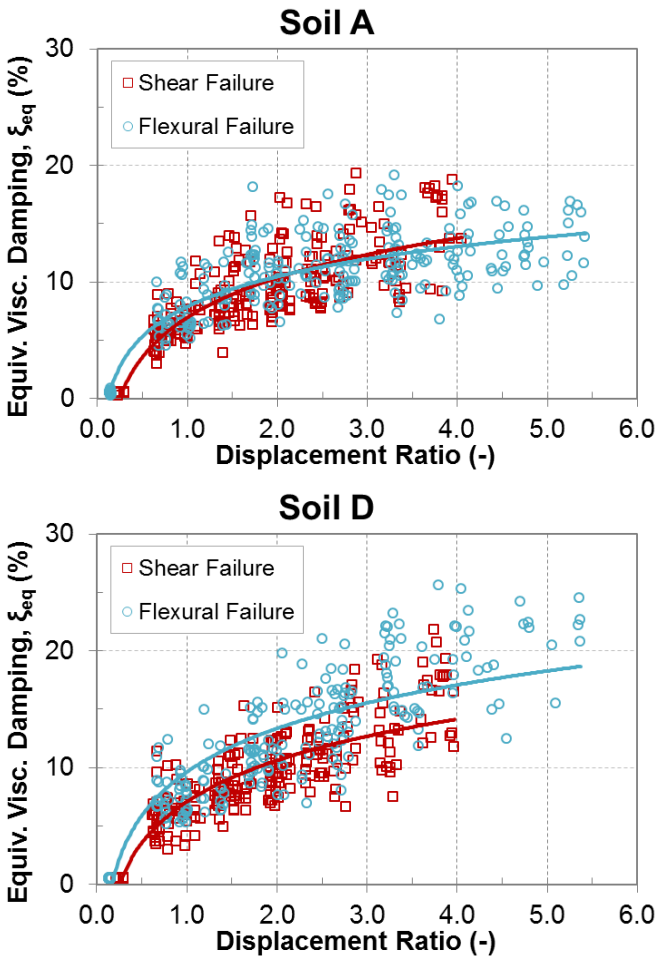

Fig. 6.6 Regression functions, related to displacement ratio, for the two failure modes. Soil type A (above) and type D (below).

Shear – Soil A $\xi_{eq} = 6.969 + 4.894 \cdot ln(DR)$ *(Eq. 6.9)*

Flexural – Soil A $\xi_{eq} = 7.893 + 3.707 \cdot ln(DR)$ *(Eq. 6.10)*

Shear – Soil D $\xi_{eq} = 7.069 + 5.100 \cdot ln(DR)$ *(Eq. 6.11)*

Flexural – Soil D $\xi_{eq} = 9.621 + 5.372 \cdot ln(DR)$ *(Eq. 6.12)*

Considering the first graph in Fig. 6.7, i.e. damping versus drift, it can be noticed that the two shear curves are very close to the flexural one for soil D. The difference between shear curves and the flexural one is in average about 10%. Considering the second graph, i.e. damping versus displacement ratio, it can be easily noted that the two shear curves are closer to the flexural one for soil A. Indeed, despite shear curves are below the flexural one for soil A at low values of DR, for DR greater than 2 they are above. The difference is in average less than 5%, and even smaller considering only the range of DR included between 2 and ultimate shear capacity.

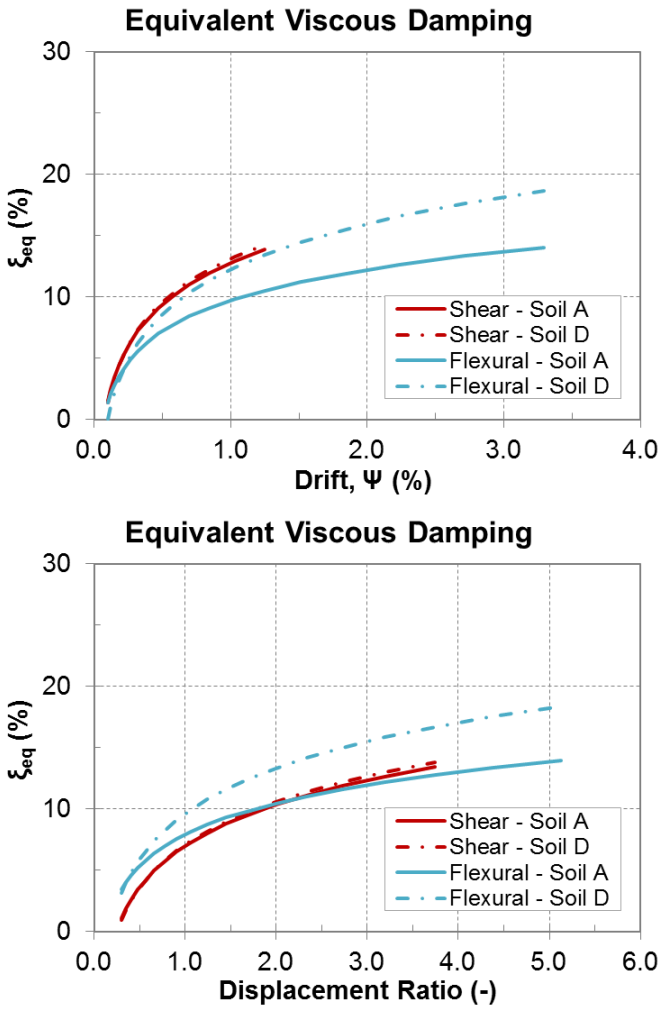

Fig. 6.7 Comparison between regression functions, related to drift (above) and displacement ratio (below).

6.2.2 Relationship Between Elastic and Inelastic Displacement

The relationships between elastic and inelastic displacement for each panel and ground type are shown in §5.4.1.2. It has been pointed out that, for shear behaviour, there are no sensitive differences between two ground types considered. Instead, for some flexural panels, regression curves for different soil types are rather separate. These observation are confirmed by graphs in Fig. 6.9, that show the comparison between curves obtained for different soil type. It has been chosen to represent the curves in function of drift, because the measured height of specimens in not exactly the same. In such a way it is possible to directly compare the specimens to each other. Starting from coefficient related to displacement and reported in Table 5.5, following equations can be used in order to obtain coefficient β and γ related to drift, called β_ψ and γ_ψ.

$$\beta_\Psi = \beta_d \cdot \left({}^{H}/_{100}\right)^{(\gamma_d - 1)} \qquad \textit{(Eq. 6.13)}$$

$$\gamma_\Psi = \gamma_d \qquad \textit{(Eq. 6.14)}$$

Coefficient β_ψ and γ_ψ are showed in Fig. 6.8. In this graph it is easy to notice that coefficients for shear panels (label “a”) are very similar to each other, and specially the same coefficients related to different soils are very similar. The same cannot be said for flexural panels (label “b”), with the exception of panel Sb06. In any case, these observations can be confirmed by performing a regression analysis, distinguishing between failure modes and soil types.

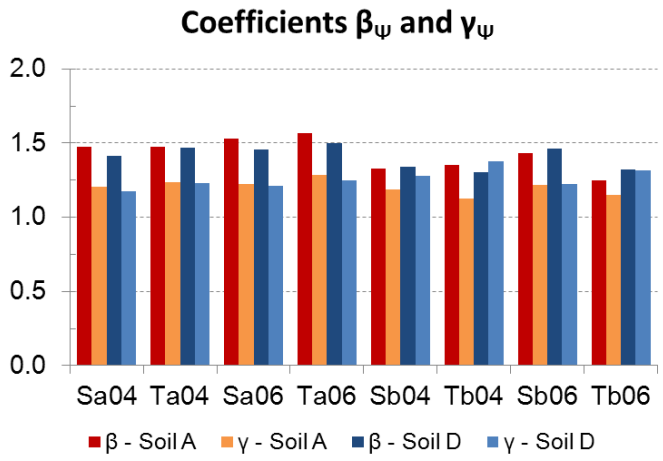

Fig. 6.8 Coefficient β and γ, related to drift, obtained for soil A (red and orange) and for soil D (blue and light blue).

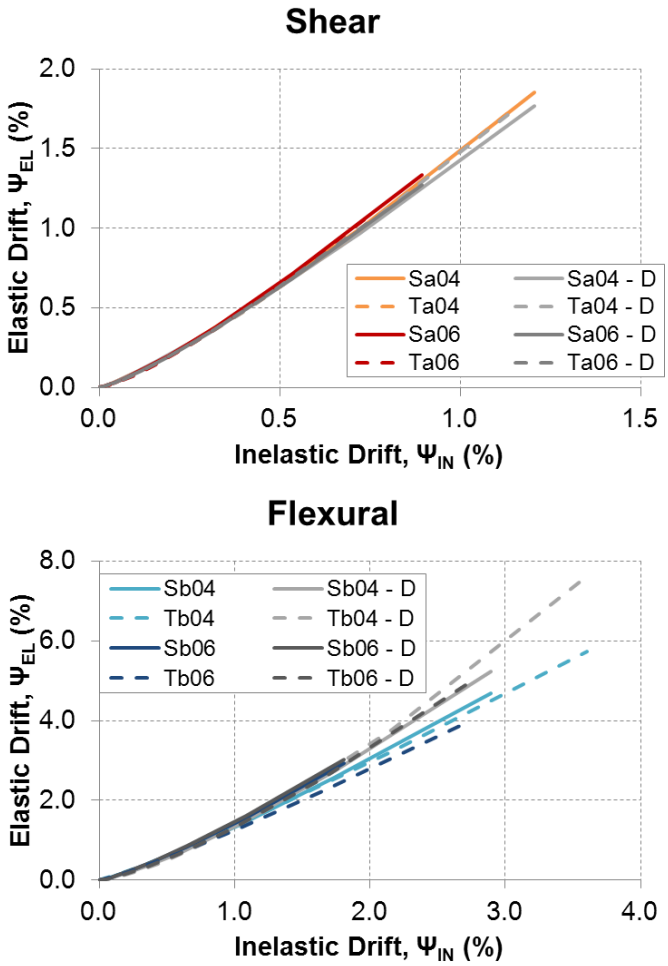

Fig. 6.9 Comparison between regression functions for soil A and D, for shear behaviour (above) and flexural behaviour (below).

Fig. 6.10 shows the points clouds related to two failure modes for both soil types, and the power functions obtained by regression analysis. The functions related to soil A are plotted in continuous line, those for soil D are plotted in dashed line. The coefficients β_ψ and γ_ψ obtained from this analysis are listed in Table 6.3, together with the coefficient R^2. The latter is always greater than 0.97, as for the analyses on each panel. This means that different level of pre-load does not affect the ratio ψ_{EL}/ψ_{IN}.

The regression functions for two soil types and failure modes are plotted in Fig. 6.11. As can be seen, the curves for shear behaviour are almost superimposed. So, for shear behaviour, the ratio ψ_{EL}/ψ_{IN} can be considered independent from soil type. On the contrary, those obtained for flexural behaviour are rather separated, with

curves for soil D above those for soil A. Furthermore, it can be noted that flexural curve for soil D is close to the shear ones.

The fact that, for soil D, ratio ψ_{EL}/ψ_{IN} is higher than for soil A, means that, for this soil type, displacement demand is greater than that for soil A. This is consistent with the displacement spectra shown in Fig. 5.1. The reason why shear behaviour involves a ratio ψ_{EL}/ψ_{IN} independent from soil type is probably linked to low periods of these panels (0.15-0.35 s). Indeed, the ratio between displacement demand of two spectra is quite low at low periods, and it increases until T_C, beyond that this ratio remains constant.

These observations are consistent with the results shown in the previous paragraph. Indeed, since the ratio between inelastic and elastic displacements is commonly expressed in function of damping (§5.4.1.3), the independency of this ratio from both pre-load level and soil type, for shear behaviour, involves that, for the same failure mode, damping is also independent from these factors. Conversely, since the relationship between the ratio ψ_{EL}/ψ_{IN}, taking into account (Eq. 5.3), is increasing with the increase of damping, the fact that, for flexural behaviour, this ratio is greater for soil D compared to soil A, involves that damping curve for soil D is above that for soil A.

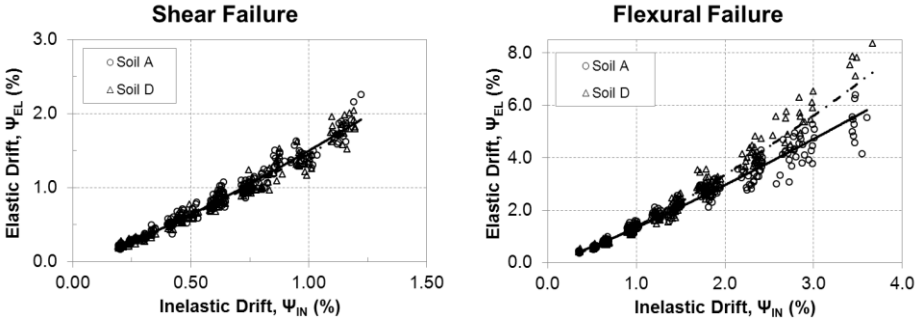

Fig. 6.10 Regression analysis of ratio Ψ_{EL}/Ψ_{IN}. Shear failure (left) and flexural failure (right) on both soil types.

Failure mode	β Soil A	γ Soil A	R^2	β Soil D	γ Soil D	R^2
Shear	1.500	1.233	0.978	1.453	1.215	0.980
Flexural	1.336	1.148	0.977	1.377	1.279	0.981

Table 6.3 Regression functions for ratio between Ψ_{EL} and Ψ_{IN}: β and γ coefficients and coefficient of determination R^2.

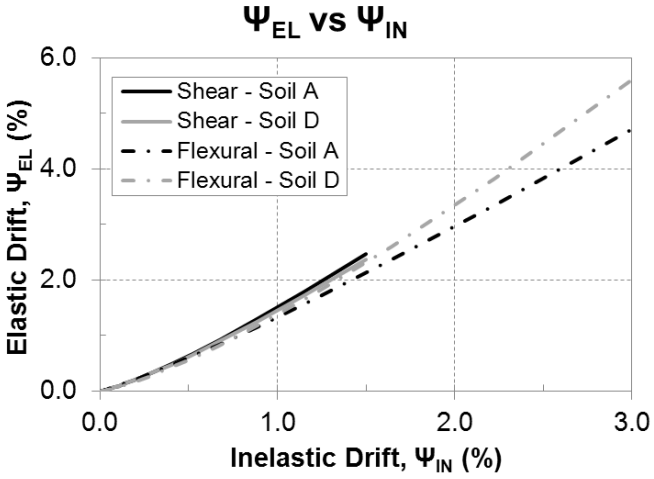

Fig. 6.11 Elastic drift versus Inelastic drift. Comparison between failure modes and soil types.

6.2.3 Damping Correction Factor

In § 5.4.1.3 it has been seen that effective Damping Correction Factor (η) can be correlated to formulation expressed by (Eq. 5.3). Since the quality of approximation is rather poor, utilizing α = 5, a calibration of coefficient α has been performed. This calibration has been performed with the least squares method. The comparison between the points cloud obtained from the analyses (η_eff) and (Eq. 5.3) with α set to 5 (η_code) and to value obtained from fitting (η_fit) is showed in Fig. 6.12 and Fig. 6.13. The code formulation with the calibrated value of coefficient α approximate the numerical data in a satisfactory way. Indeed, the value of coefficient R^2 are generally bigger than 0.8, as can be seen in Table 6.4.

The obtained values of coefficient α, for each panel and both soil types, are shown in Fig. 6.14. As can be seen, they range between 0.5 and 2.5, and in general they are smaller for soil A than for soil D. More precisely, the values of coefficient α obtained for soil D are in average twice than those obtained for soil A, with the exception of panel Tb04, which has given about the same value for both soils. Furthermore, the coefficients related to shear behaviour are in general greater than those related to flexural behaviour.

The considered expression for Factor η is proportional (not directly) to coefficient α, so the greater is α the greater is η. Factor η decreases with the increasing of damping. Hence, the obtained values of coefficient α seem to be in disagreement with the observations which were made at the end of the previous paragraph. Indeed, considering the shear panels, given a displacement level, ξ_{eq} and ratio ψ_{EL}/ψ_{IN}, i.e. 1/η, are the same for both soil types. So it would be reasonable that also coefficient α is the same. Furthermore, for flexural behaviour, given a certain

displacement level, ξ_{eq} is bigger for soil D than for soil A, whereas η of soil D is lower than that of soil A. So, in this case, it would be reasonable that coefficient α is similar for both soils, or lower for soil D compared to that for soil A.

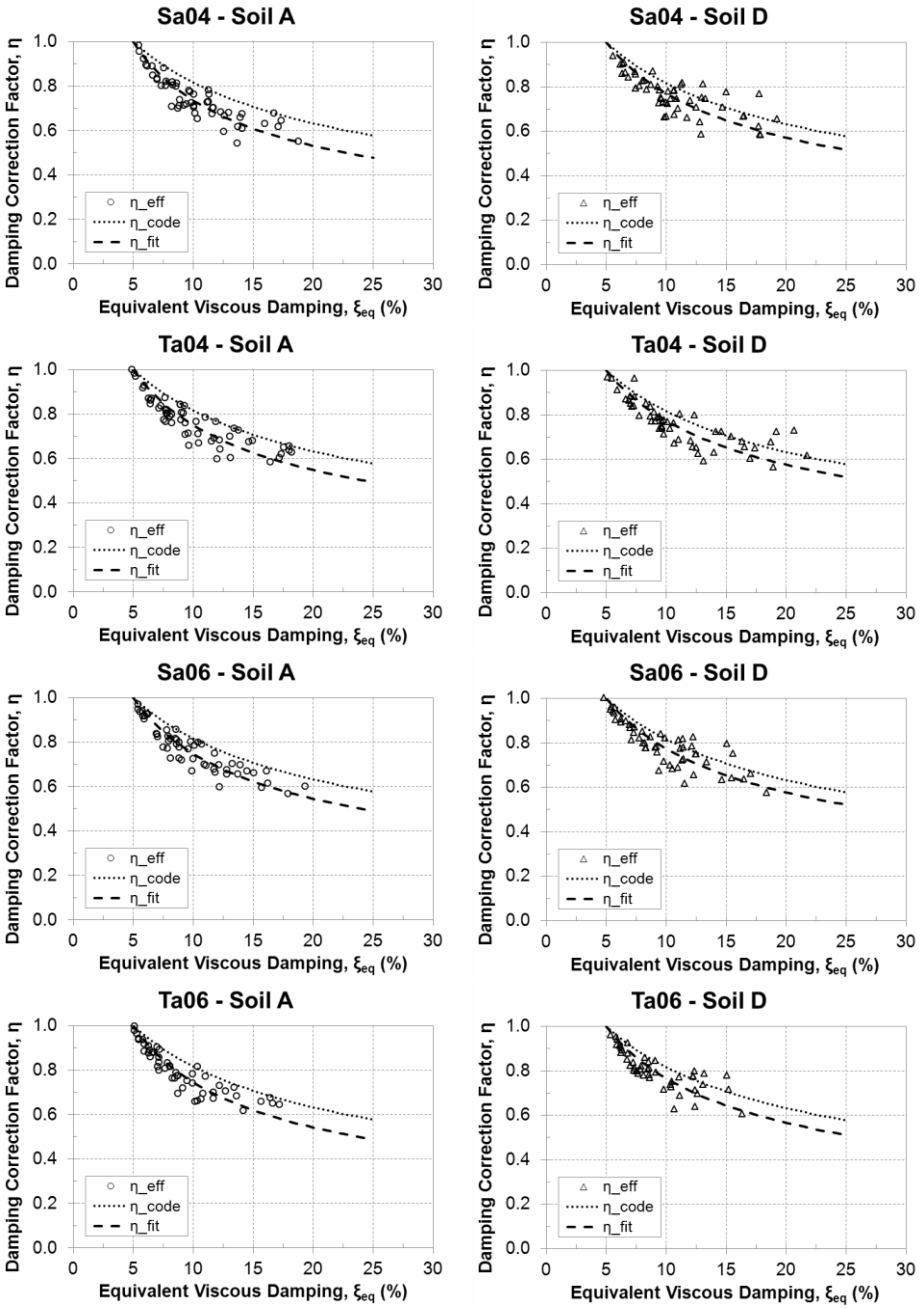

Fig. 6.12 Comparison between η effective and code formulation with α set to 5 and fitting value. Squat specimens under soil type A (on the left) and D (on the right).

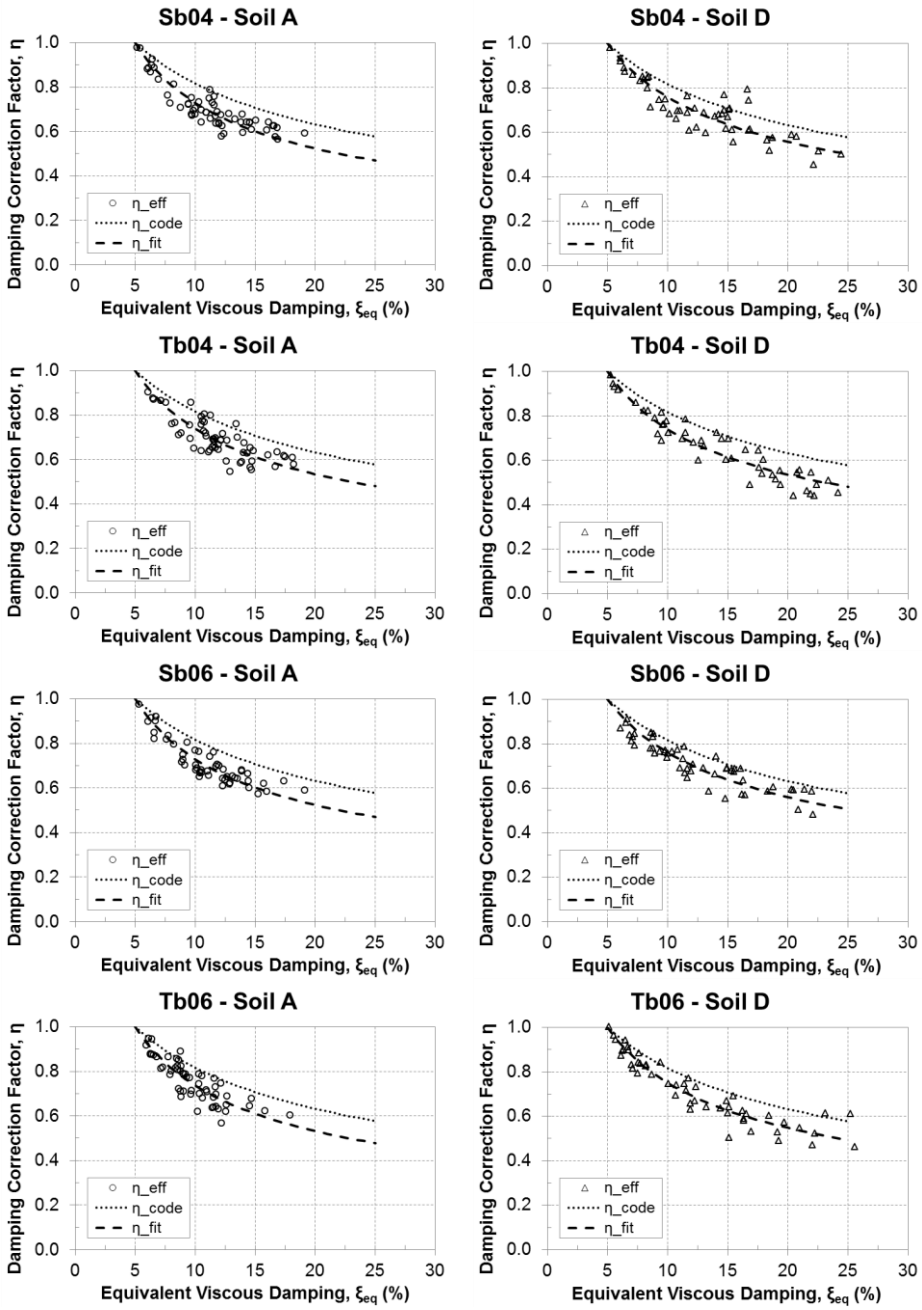

Fig. 6.13 Comparison between η effective and code formulation with α set to 5 and fitting value. Slender specimens under soil type A (on the left) and D (on the right).

Specimen	α_{fit} – Soil A	R^2 – Soil A	α_{fit} – Soil D	R^2 – Soil D
SRSa 0.4	0.9	0.804	2.3	0.649
TRSa 0.4	1.5	0.830	2.4	0.803
SRSa 0.6	1.3	0.882	2.5	0.792
TRSa 0.6	1.2	0.909	2.1	0.844
mean	*1.2*		*2.3*	
SRSb 0.4	0.7	0.820	1.8	0.777
TRSb 0.4	1.0	0.663	1.0	0.900
SRSb 0.6	0.7	0.870	1.9	0.811
TRSb 0.6	0.9	0.793	1.4	0.906
mean	*0.8*		*1.5*	

Table 6.4 Coefficient α calibrated and related R^2 for Damping Correction Factor.

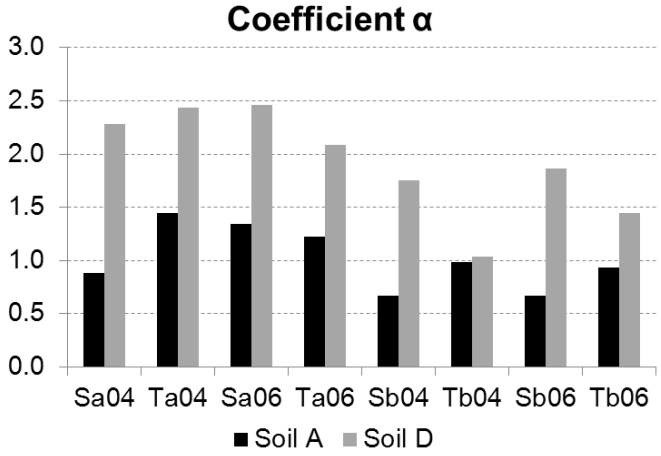

Fig. 6.14 Coefficient α calibrated for all specimens and both types of soils.

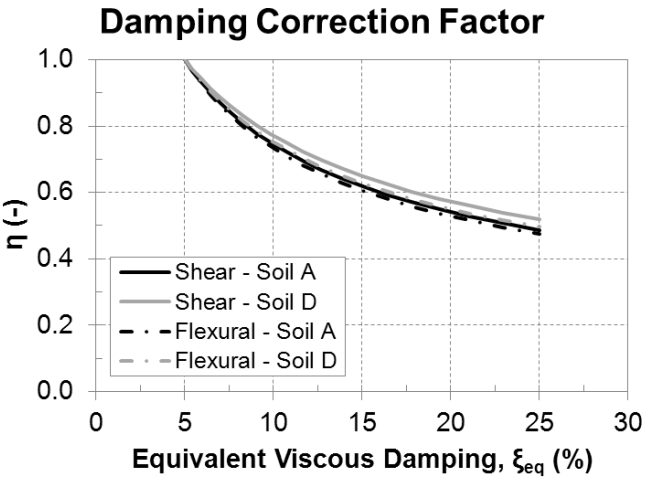

Fig. 6.15 Damping Correction Factor with α calibrated for the two failure modes and soil types.

In order to investigate this inconsistency, a further regression analysis has been performed, distinguishing only between failure modes and soil types. The results of this analysis are reported in Table 6.5. As expected, these values are very similar to the averages calculate in Table 6.4, but they are not the same (indeed the second decimal numbers are different). It can be say that for the same type of soil, the value of α for shear panels is about 50% greater than for flexural behaviour. Furthermore, these analysis confirm that soil D involves double values with respect to soil A.

It has been proven that the range of variability of coefficient α does not have an appreciable effect on the damping correction factor, as showed in Fig. 6.15. Indeed curves for both flexural and shear failure for soil A, that have coefficient α equal to 0.8, 1.5 and 1.2 respectively, are almost superimposed. Only the curve for shear and soil D, that has a coefficient α equal to 2.3, is slightly distinct from the others. More precisely, this curve is above the others, with an average difference of about +4%. On the other hand, it is possible to notice that both the curves for soil D are above those for soil A. Hence, despite the flexural curve for soil D is closer to those for soil A and both failure modes, it is practical to consider coefficient α related only to soil type. The gained values of coefficient α that can be used in (Eq. 5.3), in order to determine the damping correction factor in function of equivalent damping, are 1.0 and 1.9, for soils A and D respectively. These values have been obtained by performing regression analyses on the two points clouds which were obtained distinguishing only between soil type. The value of R^2 is 0.85 in both cases.

Failure mode	α_{fit} – Soil A	R^2 – Soil A	α_{fit} – Soil D	R^2 – Soil D
Shear	1.2	0.871	2.3	0.797
Flexural	0.8	0.807	1.5	0.861

Table 6.5 Coefficient α calibrated and related R^2 for the two failure modes and soil types.

6.3 Injected Stone Masonry

6.3.1 Equivalent Viscous Damping

Fig. 6.16 and Fig. 6.17 show the comparison between proposed procedure (black indicators) and Gulkan and Sozen (gray indicators) values of ξ_{eq}. As for reinforced masonry, the values obtained with the proposed procedure are more scattered than those obtained with G&S procedure. The results of regression analysis is reported in Table 6.6 and Table 6.7. As can be seen, the values of coefficient R^2, for the proposed procedure, range between 0.63 and 0.89, whereas

for G&S it is always higher than 0.9. The range of variability of coefficient R^2, for our procedure, is greater than that obtained for RM, i.e. 0.74 – 0.88 (§6.2.1). This means that the scatter of results for this type of masonry is greater compared to that for RM. This is evident mainly for specimens R2 and R5, on soil D, beyond maximum resistance, i.e. drift of 0.42% and 0.48% respectively.

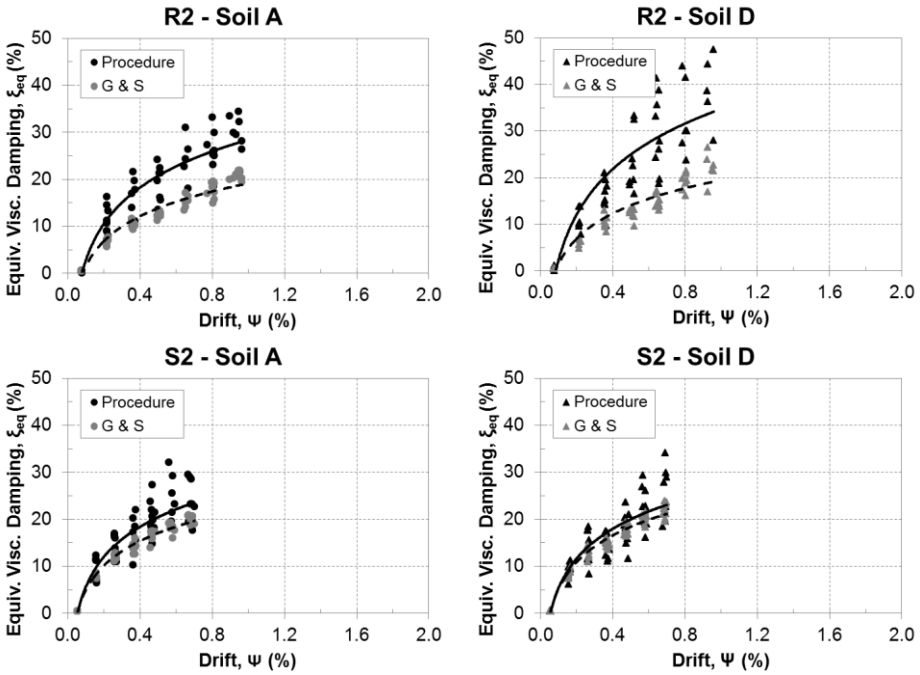

Fig. 6.16 Comparison between proposed procedure and Gulkan and Sozen values of ξ_{eq}. Squat specimens under soil type A (on the left) and D (on the right).

Squat walls	α Soil A	β Soil A	R^2	α Soil D	β Soil D	R^2
R2 1.0	28.412	11.074	0.880	34.749	14.079	0.801
S2 2.0	26.813	9.160	0.843	26.340	9.126	0.819
mean	*27.612*	*10.117*		*30.545*	*11.603*	
Slender walls	β Soil A	γ Soil A	R^2	β Soil D	γ Soil D	R^2
R4 1.0	13.130	5.355	0.634	18.516	9.495	0.868
S4 1.0	13.528	4.747	0.783	18.742	7.676	0.812
R5 2.0	19.882	7.669	0.886	27.955	12.355	0.835
S5 2.0	20.454	7.236	0.766	23.864	9.319	0.847
Mean	*16.749*	*6.252*		*22.269*	*9.711*	

Table 6.6 Regression functions for ξ_{eq} (procedure) vs Ψ: α and β coefficients and coefficient of determination R^2.

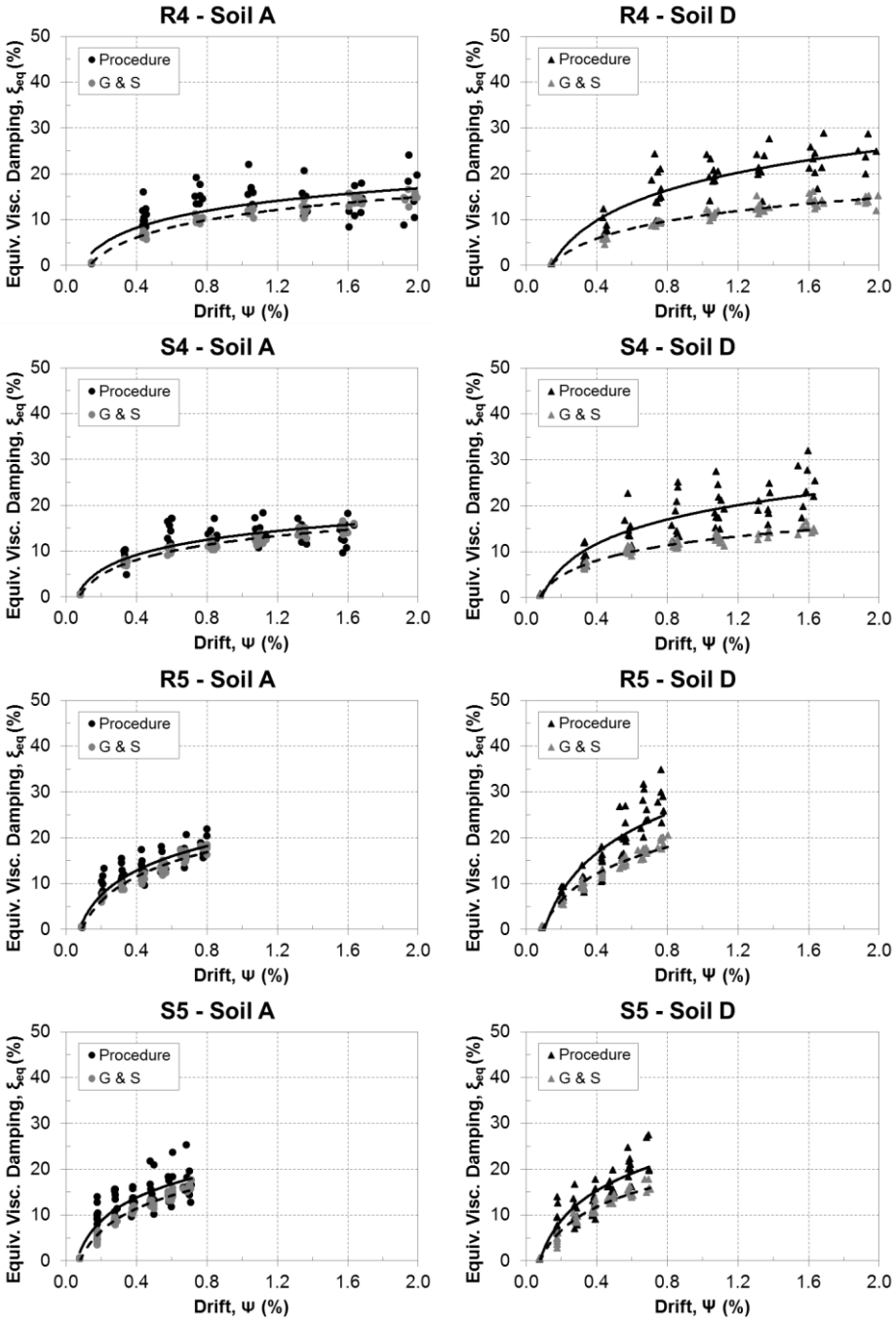

Fig. 6.17 Comparison between proposed procedure and Gulkan and Sozen values of ξ_{eq}. Slender specimens under soil type A (on the left) and D (on the right).

Squat walls	α Soil A	β Soil A	R^2	α Soil D	β Soil D	R^2
R2 1.0	19.114	7.597	0.949	19.473	7.800	0.900
S2 2.0	22.289	7.517	0.981	24.097	8.212	0.972
mean	*20.701*	*7.557*		*21.785*	*8.006*	
Slender walls	β Soil A	γ Soil A	R^2	β Soil D	γ Soil D	R^2
R4 1.0	11.131	5.469	0.972	10.899	5.505	0.966
S4 1.0	12.438	4.741	0.974	12.477	4.790	0.981
R5 2.0	18.575	7.669	0.973	19.799	8.347	0.971
S5 2.0	17.835	6.995	0.975	18.501	7.342	0.964
Mean	*14.995*	*6.219*		*15.419*	*6.496*	

Table 6.7 Regression functions for ξ_{eq} (Gulkan and Sozen) vs Ψ: α and β coefficients and coefficient of determination R^2.

It can be seen that there are sensitive differences between the results obtained with the two methodologies. The values obtained with G&S are always lower than those obtained with proposed procedure. The difference is in average about 17% and 30%, respectively for soil A and soil D, and it changes between a panel and another. Above all, squat specimens exhibit very different behaviour. Panel R2, tested under a pre-load of 1.0 N/mm^2, gives the greater differences between the two methodologies, i.e. about 30% and 40% for the two ground types considered. Conversely, panel S2, tested under a pre-load of 2.0 N/mm^2, gives the smallest differences, greater for soil A than for soil D, i.e. about 16% and 8% respectively.

Regardless these differences, both the approaches lead to values higher than expected. This is mainly due to the high vertical pre-loads at which the panel were tested, that are about 0.15% (panels R2, R4 and S4) and 0.30% (panels S2, R5 and S5) of the compressive strength. These rather high loads were chosen in order to force the shear failure mechanism, as explained in §3.3.2. Vertical load influences not only the failure mode, but also the amount of dissipated energy. Indeed, the ratio between dissipated and input energy (E_{hys}/E_{inp}) ranged between 40% and 60% for slender walls tested under a pre-load of 2.0 N/mm^2 (slender-2.0) and squat walls tested under both pre-loads, and between 30% and 40% for slender walls tested under 1.0 N/mm^2 (slender–1.0). These high values of ratio E_{hys}/E_{inp} involve necessary high values of hysteretic damping. If this may influence the quantitative aspect of the following analysis, on the other hand the interest toward the qualitative aspect remains.

As for RM, G&S approach leads to no sensitive differences between different soil types. Indeed, despite the obtained values for soil D are slightly higher than those for soil A, the average relative difference is less than 3%. The great differences between the curves obtained with the two methodologies, together with the high scattering of our procedure results, lead to consider less reliable the curves

of the proposed procedure. Indeed, despite the observations made in §6.2.1 regarding the reliability of G&S approach, it would be reasonable that the differences between two approaches are not too high, as in this case. Furthermore, it has to be highlighted that, for this masonry type, the hysteretic model has been modified, assuming Z parameter as constant and equal to 1 (§4.4.2). This assumption involves that degradation of stiffness of branch D-A is small, above all if it is compared with that of the next branch A-B. So the loading path is characterized by a point at which a sudden decrease of stiffness happens, which on one hand is unrealistic, and on the other determines an equally sudden change of velocity, which is surely not compatible with G&S hypothesis.

For these reasons, the obtained curves for panels that give large scatter of results and for which the two approaches lead to high differences, especially on soil A, are considered less reliable. These are, above all, R2 panel on both soils and R5 on soil D.

Fig. 6.18 shows the comparison between all the obtained regression functions, expressed in function of drift. It can be noticed that, for soil A, the panels tested under the same conditions give more or less the same values. Indeed, the three couples of specimens, i.e. R2 - S2 (Squat), R4 - S4 and R5 - S5, are characterized by three separated trends. Squat specimens reach the higher values of damping, about 25%, whereas slender specimens are characterized by lower values, about 17%. However, slender-1.0 reach an ultimate drift of about 2.0%, whereas slender slender-2.0 have a maximum displacement capacity similar to squat specimens, i.e. about 0.8%. Hence, damping curves for couple R5 – S5 are between the other two groups of curves.

For soil type D the three couples of panels have not a well distinct behaviour as for soil A. In particular, the squat panels give very different results. Indeed R2 reaches a maximum value of damping which is higher than 30%, whereas S2 reaches about the same maximum value that is reached for soil A, i.e. 25%. Instead, it can be noticed, for slender panels, an increment of about 30% of maximum damping values from soil A to soil D. They reach a maximum value of about 23%. So it can be said that for soil type D, excluding R2 panel, it is possible to distinguish two groups of panels, characterized by the same maximum values of damping, i.e. about 23-25%, but different ultimate drift. The first group is composed by squat panel S2 with the slender-2.0 panels (R5 and S5), the second is represented by slender-1.0 panels (R4 – S4).

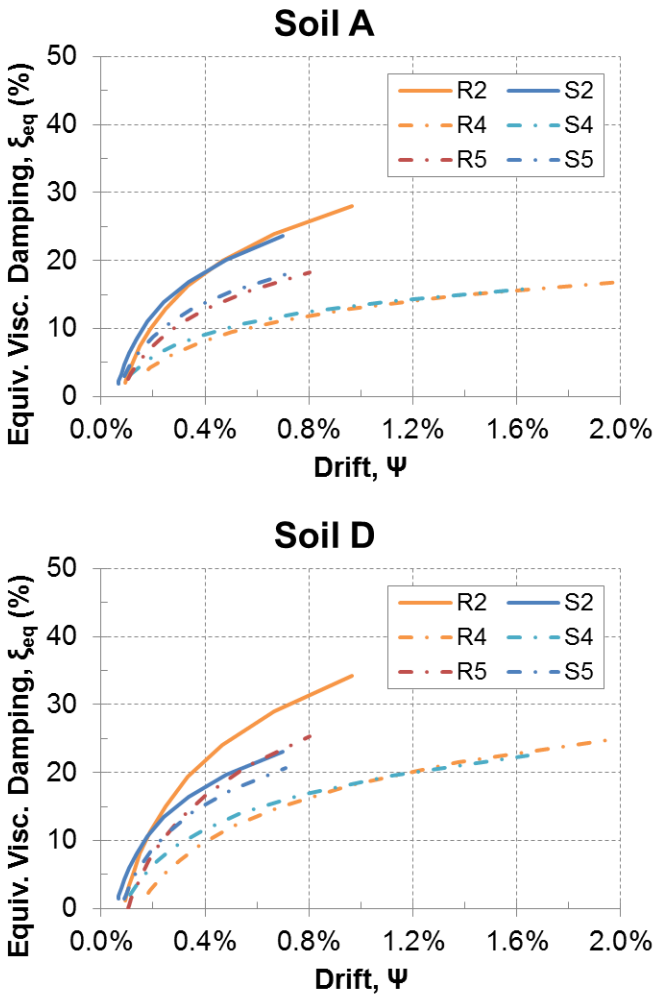

Fig. 6.18 Equivalent Viscous Damping versus Drift curves.
Experimental SM walls under soil type A (above) type D (below).

Fig. 6.19 shows the same curves of Fig. 6.18, but expressed in function of DR. Differently from what observed for RM, damping curves seem not to be well correlated to DR. The above mentioned observations, regarding the reliability of obtained results, lead to give small reliable to R2 on both soils and R5 on soil D. Excluding these curves, it is possible to identify, for soil A, two well separate groups, whereas for soil D the curves are all superimposed to each other. For soil A, one group is composed by slender-1.0 panels and the other by slender-2.0 and S2 panels, i.e. the specimens tented under a pre-load of 2.0 N/mm^2.

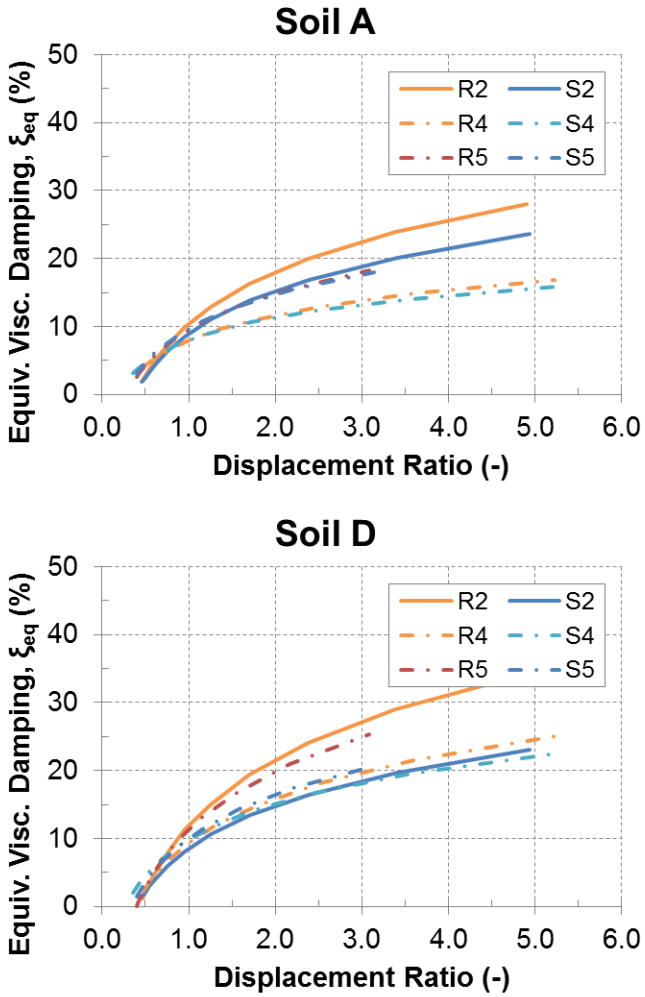

Fig. 6.19 Equivalent Viscous Damping versus DR curves.
Experimental SM walls under soil type A (above) type D (below).

For this type of masonry, tested under the above mentioned high levels of pre-load, it has been shown that, with the exception slender-1.0 panels, it is not possible to distinguish the curves in function of both drift and DR, independently from soil types, as done for RM. In addition, taking into account that rarely real structures built with this typology are subjected to vertical stress higher than 1.0 N/mm^2, and also considering the observations about reliability of obtained results, it can be concluded that only slender-1.0 curves can be considered reliable for practical applications. For this reason, it has been chosen to perform a further regression analysis, considering only the results obtained for slender-1.0 panels.

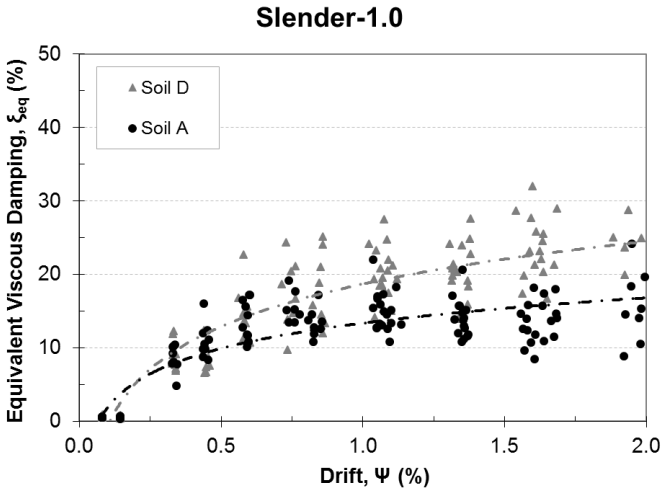

Fig. 6.20 Regression functions, related to drift, for slender-1.0 panels on both soil types.

Slender-1.0 – Soil A $\xi_{eq} = 13.342 + 4.965 \cdot ln(\Psi)$ *(Eq. 6.15)*

Slender-1.0 – Soil D $\xi_{eq} = 18.672 + 8.356 \cdot ln(\Psi)$ *(Eq. 6.16)*

Fig. 6.20 shows the obtained regression functions, which equations are expressed by (Eq. 6.15) and (Eq. 6.16). Black circular indicators are referred to soil A, grey triangular indicators are referred to soil D. The obtained regression functions are plotted in dashed black and grey lines, for soil A and D respectively. It can be noticed that logarithmic function used to approximate the numerical results, tends to underestimates damping values at low drift level on soil A. This is due to period shift, which involves effective periods beyond spectrum plateau for drift level greater than about 0.85%. Hence, beyond this values of drift, on soil A, more or less constant values of damping are obtained, with an average value of 14%. As a consequence, since logarithmic function is increasing with the increasing of drift, the approximated values in the low drift range are underestimate. This is confirmed also by values of obtained coefficient R^2: 0.697 and 0.829 for soil A and D, respectively.

In order to take into account with more accuracy the values obtained for drift lower than 0.85%, it would be proper to consider, in the regression analysis, only those values related to drifts lower than this limit. Observing the graphs in Fig. 6.20, it is easy to notice that in this way only few displacements target (d_t) would be considered, and so the regression analysis would be based on a limited number of values. For this reason, it has been chosen to apply again the procedure described

in §5.2, considering d_t comprised between first limit state and displacement corresponding to 0.85% of drift.

Fig. 6.21 shows the obtained results. It can be easily noticed that, as expected, there are no sensitive differences between soil types. Indeed, for the considered drift levels, effective periods associated to secant stiffness are comprised in spectra plateau for both soils. With a regression on the whole points cloud, without distinguish between soil types, functions expressed by (Eq. 6.17) and (Eq. 6.18) are obtained, related to drift and displacement ratio, respectively. The corresponding values of coefficient R^2 are 0.757 and 0.778.

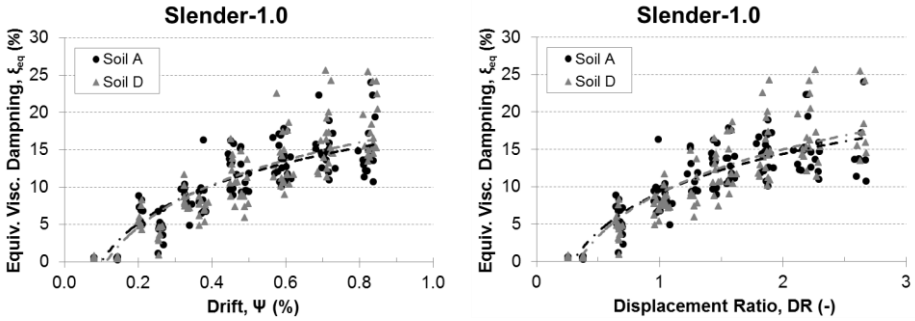

Fig. 6.21 Slender-1.0 specimens: comparison between values of ξ_{eq} obtained for soil type A and D, in relation of drift (left) and displacement ratio (right).

Slender-1.0 - ψ $$\xi_{eq} = 17.40 + 7.77 \cdot ln(\Psi)$$ *(Eq. 6.17)*

Slender-1.0 - DR $$\xi_{eq} = 9.17 + 7.95 \cdot ln(DR)$$ *(Eq. 6.18)*

In conclusion it can be said that there is no soil dependency for drift less than about 0.85%. In this case, (Eq. 6.17) and (Eq. 6.18) can be considered for the evaluation of damping. For drift higher than 0.85%, for soil A, due to period shift, a constant value of damping can be considered, i.e. 14%, whereas for soil D you can refer to (Eq. 6.16).

6.3.2 Relationship Between Elastic and Inelastic Displacement

Fig. 6.22 shows the coefficients reported in Table 5.5, referred to drift. It is possible to notice that panels tested in the same conditions (aspect ratio and pre-load level) have similar coefficients. This observation is confirmed by Fig. 6.24, where the various functions are plotted. Furthermore, in the second graph of this Figure, it can be seen that for soil D the curves for squat and slender-2.0 panels are very close. In Fig. 6.23 all the curves for both soil types are showed and compared. In this graph it can be noticed that the gratest differences between soil types are obtain by slender-1.0 panels.

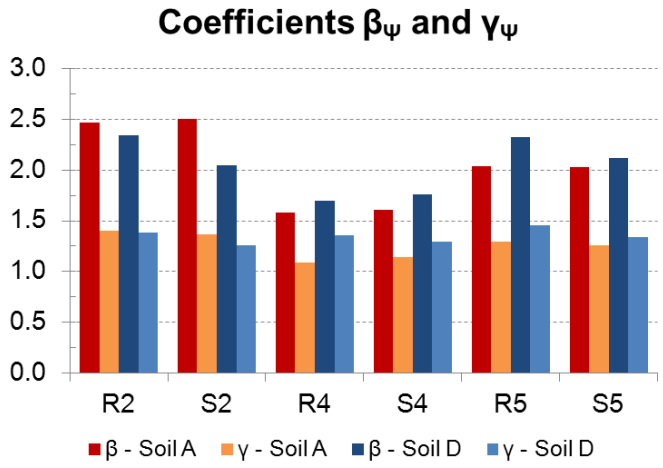

Fig. 6.22 Coefficient β and γ, related to drift, obtained for soil A (red and orange) and for soil D (blue and light blue).

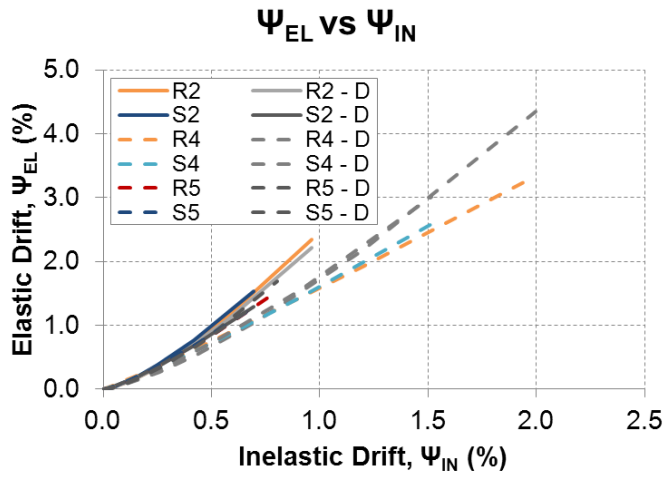

Fig. 6.23 Comparison between regression functions for soil A and D, for shear behaviour (above) and flexural behaviour (below).

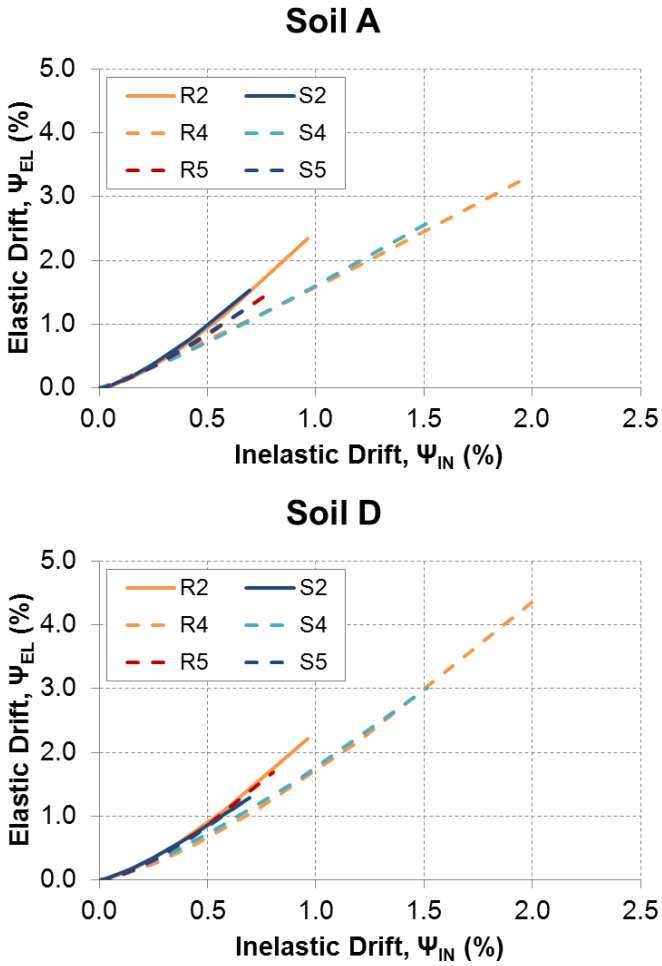

Fig. 6.24 Comparison among regression functions for different aspect ratios and pre-load level, for soil type A (above) and soil type D(below).

A second regression analysis has been performed, distinguishing among the three couples of specimens and between soil types, Fig. 6.25 and Fig. 6.26. The results of this analysis are reported in Table 6.8. The values of coefficient R^2 are all higher than 0.95. So the chosen power function can be considered reliable to approximate the relationship between elastic and inelastic drift. Fig. 6.27 shows the obtained regression functions. As can be seen, each couple of panels gave different results. Squat and slender-1.0 panels are characterized by rather distinct curves for the two soil types, whereas, for slender-2.0 panels, the type of soil does not have a sensitive effect. For squat panels, soil A curve is above that of soil D, whereas for slender-1.0 panels it occurs the contrary. It is interesting to notice that, for RM, in case of shear behaviour there is a certain independency of ratio ψ_{EL}/ψ_{IN}, and also

damping, from soil type, whereas, in case of flexural behaviour, the ratio ψ_{EL}/ψ_{IN}, and also damping, are higher for soil D than that for soil A (§6.2.2). Hence, it is possible to notice a similarity between the RM panels that failed in flexure and SM slender-1.0.

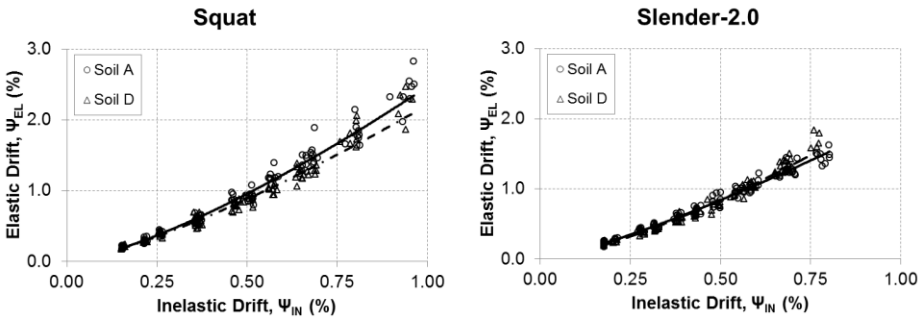

Fig. 6.25 Regression analysis of ratio Ψ_{EL}/Ψ_{IN}. Squat specimens (left) and slender-2.0 specimens (right) on both soil types.

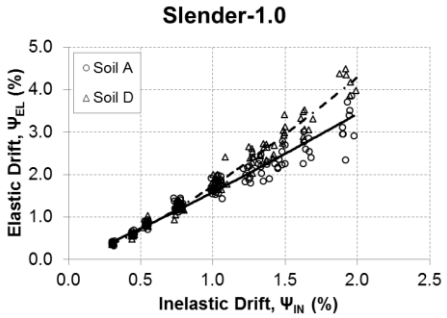

Fig. 6.26 Regression analysis of ratio Ψ_{EL}/Ψ_{IN}. Slender-1.0 specimens on both soil types.

Failure mode	β Soil A	γ Soil A	R^2	β Soil D	γ Soil D	R^2
Squat	2.472	1.369	0.985	2.212	1.326	0.980
Slender 1.0	1.587	1.113	0.966	1.735	1.307	0.986
Slender 2.0	2.027	1.271	0.984	2.209	1.387	0.981

Table 6.8 Regression functions for ratio between Ψ_{EL} and Ψ_{IN}: β and γ coefficients and coefficient of determination R^2.

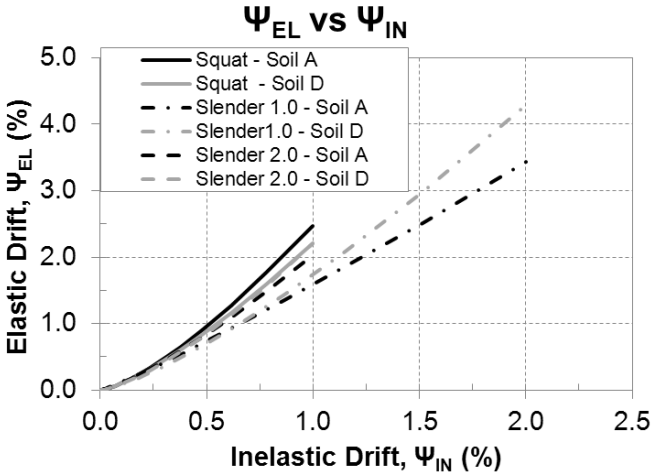

Fig. 6.27 Elastic drift versus Inelastic drift. Comparison between aspect ratio, pre-load level and soil types.

6.3.3 Damping Correction Factor

Fig. 6.28 and Fig. 6.29 show, for each panels and soil type, the comparison among the points cloud obtained from the numerical analyses and the damping correction factor, expressed by (Eq. 5.3), with α set to 5 and the value obtained from the regression analysis. These values are reported, together with coefficients R^2, in Table 6.9. It can be said that the utilized function is generally able to reliably approximate the numerical data. Indeed the values of coefficient R^2 are generally included between 0.70 and 0.83. The only exceptions are represented by panels with lower damping, i.e. slender 1.0 under soil A. Indeed these panels are characterized by little variation of damping values and by rather scattered distribution of effective η. In any case, observing the graphs it can be said that the quality of approximation can be considered acceptable also for these panels.

Fig. 6.30 shows the values of calibrated coefficient α. It can be noticed that all panels gave very low values for soil A, without sensitive differences between different aspect ratios and pre-load levels. For soil type D, instead, squat panels gave values slightly higher than those obtained for slender panels. Instead there are no sensitive differences between pre-load levels. So a further regression analysis has been performed, distinguishing between different aspect ratios and soil types. The results of this analysis are shown in Table 6.10. The obtained values of coefficient α are equal to 0.5 and 2.7 for squat specimens, related to soil A and D respectively, and to 0.6 and 1.6 for slender specimens. The coefficient of determination is included between 0.68 and 0.83 in all the four combinations, so it can be said that the quality of approximation is fair.

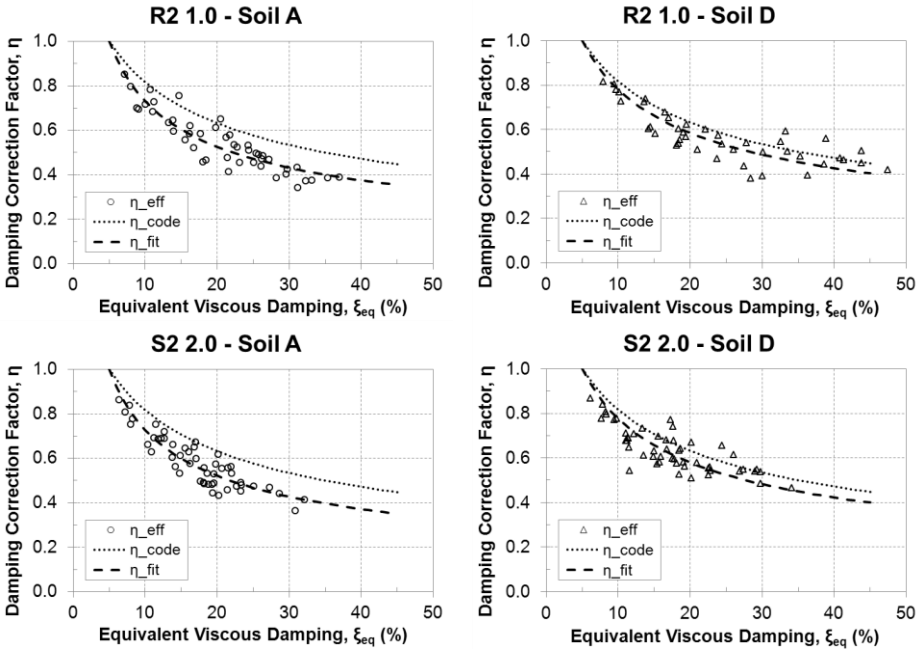

Fig. 6.28 Comparison between η effective and code formulation with α set to 5 and fitting value. Squat specimens under soil type A (on the left) and D (on the right).

The η-functions obtained using the mentioned values of coefficient α are plotted in Fig. 6.31. As can be seen, the curves for soil A are almost perfectly superimposed. Indeed, also the curves for soil D are very close one to each other, which means that the influence of different aspect ratios can be considered negligible. Hence it is reasonable to consider two values of coefficient α: 0.5 for soil A and 2.0 for soil D.

Specimen	α_{fit} – Soil A	R^2 – Soil A	α_{fit} – Soil D	R^2 – Soil D
R2 1.0	0.7	0.825	2.8	0.748
S2 2.0	0.6	0.820	2.6	0.570
mean	*0.7*		*2.7*	
R4 1.0	0.8	0.580	1.5	0.764
S4 1.0	0.5	0.577	1.9	0.713
R5 2.0	0.4	0.705	1.8	0.844
S5 2.0	0.6	0.768	1.9	0.831
Mean	*0.5*		*1.8*	

Table 6.9 Coefficient α calibrated and related R^2 for Damping Correction Factor.

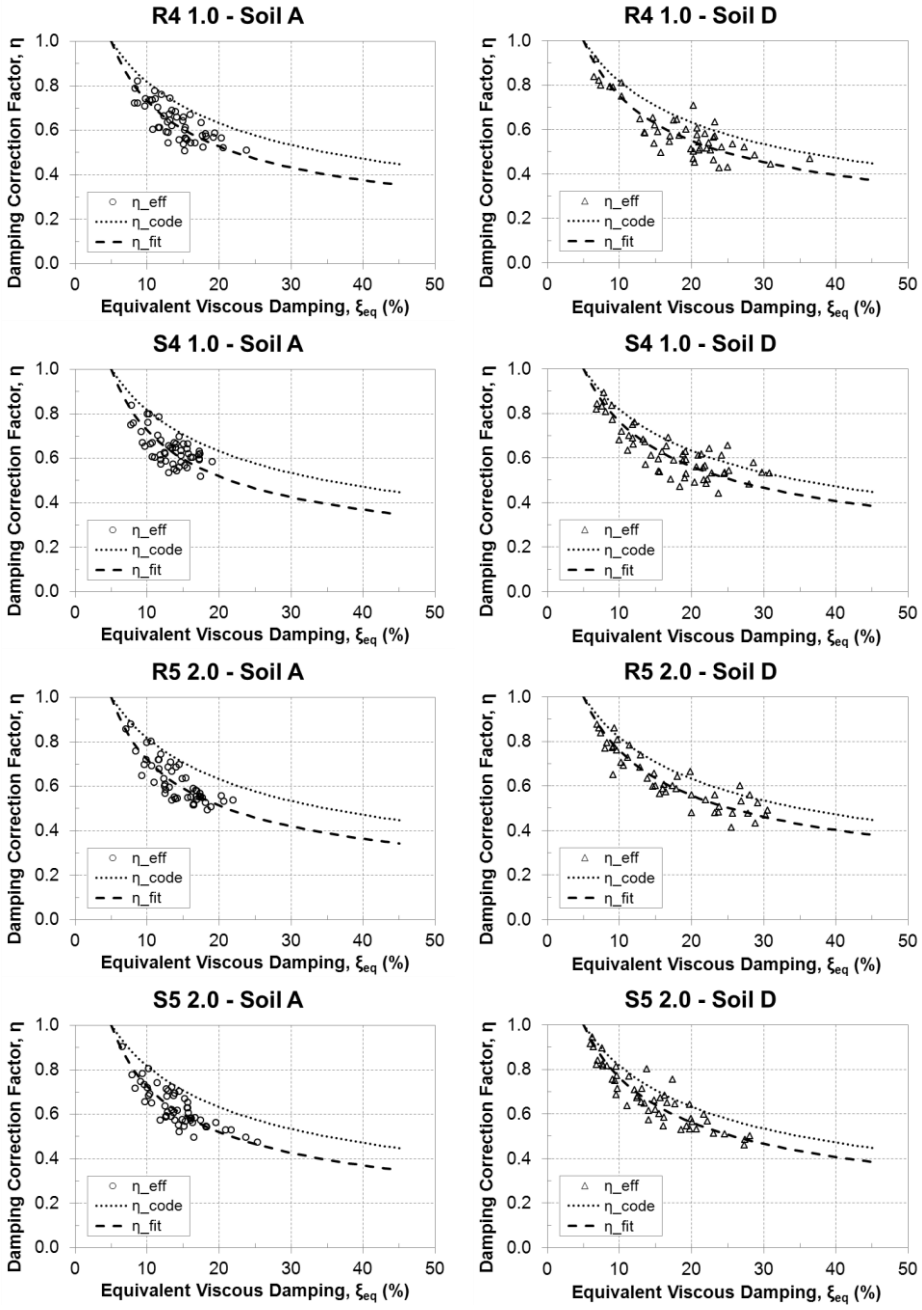

Fig. 6.29 Comparison between η effective and code formulation with α set to 5 and fitting value. Slender specimens under soil type A (on the left) and D (on the right).

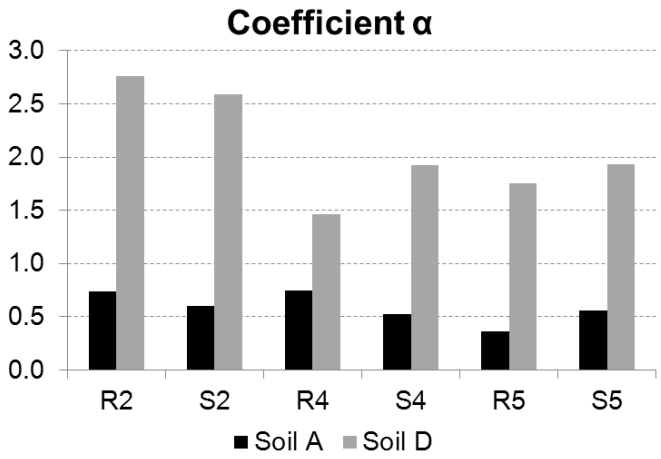

Fig. 6.30 Coefficient α calibrated for all specimens and both types of soils.

Aspect Ratio	α_{fit} – Soil A	R^2 – Soil A	α_{fit} – Soil D	R^2 – Soil D
Squat	0.6	0.828	2.6	0.687
Slender	0.5	0.681	1.7	0.794

Table 6.10 Coefficient α calibrated and related R^2 for the two aspect ratios and soil types.

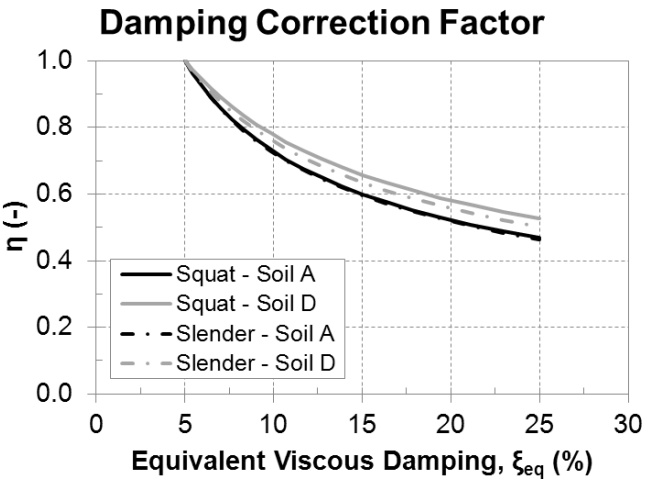

Fig. 6.31 Damping Correction Factor with α calibrated for the two aspect ratios and soil types.

6.4 Conclusive Remarks

The analysis of results obtained in the previous Chapter allowed to gain the following conclusions:

- The values of equivalent viscous damping obtained by proposed procedure, despite the greater scatter, are based on explicit equality of displacements, that is the aim of using equivalent damping, whereas Gulkan & Sozen method is based on equality of dissipated energy, even if the validity of equal velocity assumption has not been proven. On the other hand, the results obtained with our procedure are more scattered than those obtained with G&S method.
- Equivalent viscous damping is increasing for increasing inelastic displacements, when period corresponding to secant stiffness is included in spectrum plateau. Otherwise damping can be considered constant.
- The values of ξ_{eq} can be approximate using a logarithmic function. These functions can be related to drift or displacement ratio, using the logarithmic properties.

For what concern RM:

- Failure mode and type of soil are the most sensitive parameters, for the evaluation of damping. Although the investigated range is quite limited, it has been observed an independency of the pre-load level applied.
- Flexural behaviour is characterized by damping values that are dependent from soil type, whereas shear behaviour is not soil dependent. Flexural behaviour on soil D involves damping values greater of about 30% compared to soil A. These observations are valid both for drift-damping and DR-damping curves. Damping values, at maximum displacement capacity, are about 14% for shear behaviour, and ranging between 15 and 19% for flexural behaviour, according to soil type.
- Relationship between elastic and inelastic displacements confirm both the soil independency linked to shear behaviour and, for flexural behaviour, the higher values of damping on soil D compared to those on soil A.
- The calibration of Damping Correction Factor leads to values of coefficient α independent from failure mode, and slightly dependent from soil type. The obtained values are 1.0 and 1.9 for soil type A and D, respectively. Since the variability of coefficient α does not have an appreciable effect on the damping correction factor, it would be possible to give a unique value for both soil types. This value should be representative also to other soil types, which are not taken into account. So it is conservative to consider the value obtained for

soil D, that basically leads to consider the formulation included in the previous version of EC8, that is also suggested by (Priestley et al., 2007).

For what concern SM:

- For this type of masonry the results given by proposed procedure are more difficult to be interpreted. The reason of this is probably due high level of pre-load applied during the experimental tests, and also to high non-homogeneity of this material, that increases the probability of local phenomena, which influence the global behaviour more than it occurs in modern masonry. These difficulties are highlighted by a greater difference between values obtained with our procedure and G&S method and also by a greater scatter of results compared to those obtained for RM. In order to obtain a more reliable result, the analyses should be based on a wider number of experimental tests.
- For this type of masonry, load and soil type are the most sensitive parameters. Given the same conditions, soil D and high pre-load level involve greater values than, respectively, soil A, and low pre-load level.
- The high level of pre-load has involved high ratio between dissipated and input energy, and so high level of damping. Since in real structures this level of compression is not realistic, only the curves obtained for slender-1.0 can be considered useful for practical use. For these panels, an independency from soil type has been observed for drift less than 0.85% (effective periods comprised in the spectrum plateau). For higher drift levels, a constant value of damping can be considered on soil A, equal to 14%. For soil D, instead, damping values increase until about 23% at ultimate displacement capacity.
- The calibration of Damping Correction Factor leads to values of coefficient α slightly dependent from soil type. The obtained values are 0.5 and 2.0 for soil type A and D, respectively. Hence, as for RM, the formulation included in the previous version of EC8 is more reliable that the one in the current version in order to estimate inelastic displacement for stone masonry.

7 APPLICATION ON MULTI DEGREE OF FREEDOM STRUCTURE

7.1 Introduction

This chapter provides a simple application of proposed procedure on a multi degree of freedom masonry structure, with the aim of validating the obtained results for SDOF. This work is done using a finite element model calibrated on the base of experimental results obtained from shaking table tests on whole structures reported in (Mazzon, 2010).

NLTH analyses are performed on the calibrated model, providing the actual displacement shape of the structure, that is needed for the determination of the characteristics of the equivalent SDOF substitute structure. At this point, it is possible to apply to the equivalent SDOF, the procedure described in chapter 5.

7.2 Description of the Structures

The experimental campaign consisted of shaking table test on two models, having the same geometry, built one in unstrengthen conditions (URM) and the other one strengthened (SM) with natural hydraulic lime grout injections (Mazzon, 2010). Since the URM model was prevented from collapsing, it was possible to repair this structure by injection in order to test it again. The URM model repaired after a series of shaking table tests establishes a third model, called Repaired Masonry (RM) model. For what concern this study, only the strengthened model will be taken into account.

The models were constructed in reduced scale (2:3) with a rectangular floor plan (2.40x2.80 m), with two floors and overall height equal to 3.60 m (1.80 m per floor). The perimeter walls (Fig. 7.2) were constructed with various openings in order to achieve an asymmetric behaviour with torsional effects.

The floors are composed of timber beams with cross section 9.0x12.0 cm, used along with double timber planking with an overall thickness of 4.0 cm, orthogonally wrapped and nailed on the beams. Steel ties were used at both floor levels in order to avoid the out-of-plane behaviour of the walls. Three were used to fix timber beam

heads to the walls and three were placed in the orthogonal direction to link the opposite walls. Timber lintels were used over the openings, Fig. 7.1.

Both structures consisted of three-leaf stone masonry walls with a total thickness of 33.0 cm. The external leaves have a thickness of 12.0 cm and they are built with rough limestone and natural hydraulic lime mortar, while the inner core was built with limestone fragments. Hydraulic lime based grout was used to strengthened the internal core of the considered structure.

The whole masonry structure was built on a RC base of 40.0 cm height, which was doubly fixed on the shaking table. Horizontal movements were inhibited by means of 14 L-shaped steel plates, arranged along the perimeter of the concrete base and fixed to the strong steel base of the shaking table. Pre-stressed steel bars, binding two long HE steel beams passing horizontally through two pairs of holes provided in the concrete base, prevented vertical displacements.

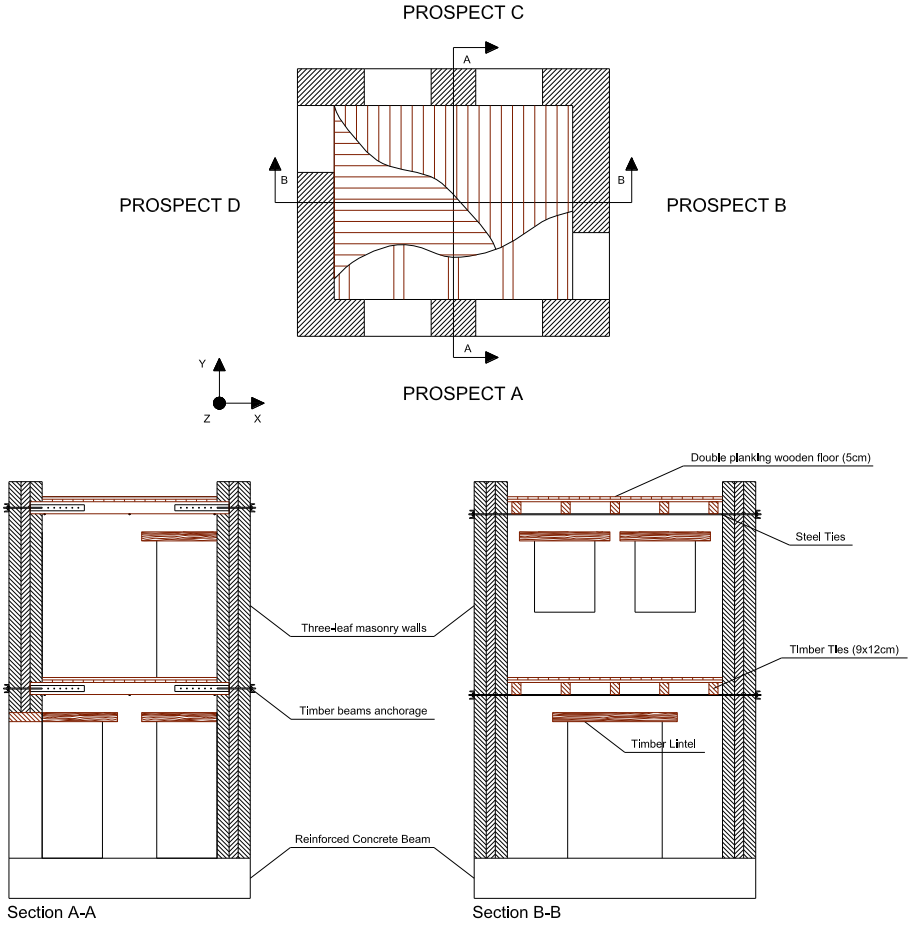

Fig. 7.1 Sections and structural components of the houses.

In order to simulate the effects of the live load in scaled specimens, additional masses have been added to both floors as proposed by (Tomaževič & Velechovsky, 1992). According to this method the ratio of the mass of the floors to the mass of the walls must be the same in the prototype and in the scaled model. In order to achieve this, steel plates, for an overall mass of 500 kg, were added per each floor, fixed using pins.

Fig. 7.2 Different prospect of the houses.

7.3 Finite Element Analysis

7.3.1 Continuum Damage model

The concept of damage can be interpreted as a measure of defects, micro-cracks and micro-cavities of the material associated to an element of internal surface. The non-linearity of the material is interpreted as the results of the evolution of those same defects, (Faria et al., 1998). The adopted methodology consists on a continuum damage model based on the Continuum Damage mechanics, originally developed for the analysis of large dimension concrete structures such as dams, and capable of reproducing the dissimilar degrading phenomena that occurs under tension or compression. This model incorporates two damage variables, one for tension (d^+) and another for compression (d^-) and a plastic deformation tensor for the characterization of the non-linear concrete degradation mechanisms under tensile and compression conditions.

The model constitution is capable of reproducing the material tension/deformation curves, including hardening and softening effects and the mechanisms for recovery of stiffness. In the field of Damage Mechanics, the effects of damage is reflected in the reduction of several of stiffness components, and the damaged material may remain isotropic or became anisotropic.

The damage variables (d^+ and d^-) can only assume values between 0 and 1 (Eq. 7.1), 0 corresponds to the elastic state and it increases with the evolution of the damage until it reaches 1 that corresponds to the collapse state. This evolution is characterized by the decrease of the effective resistant area, i.e. area without defects. The damage variables show three types of laws, depending on whether the analysis of damage is in tensile, in compression or in cyclical conditions. These laws are obtained by experimental observations, being dependent on hardening variables that depend on the deformation of the element.

$$0 \leq (d^+,\ d^-) \leq 1 \qquad \textit{(Eq. 7.1)}$$

A basic entity of such a model is the "effective stress tensor" ($\bar{\sigma}$) which is split into tensile ($\bar{\sigma}^+$) and compressive ($\bar{\sigma}^-$) components in order to clearly distinguish the respective stress contributions. In what concerns the constitutive law, the model leads to the following intuitive format:

$$\sigma = (1 - d^+)\bar{\sigma}^+ + (1 - d^-)\bar{\sigma}^- \qquad \textit{(Eq. 7.2)}$$

In the need to define, with precision, if the element is in "load", "unload" or "reload" the model introduces the concept of equivalent tension associated to a positive scalar value, which is the results of the norm of tensors of effective tensions. The different three-dimensional states of tension can then be compared through a 1D analysis. Following the tensor decomposition adopted by this model, the equivalent tensile and compressive tensions are then considered, being associated with different damage criteria.

As explained by (Faria et al., 1998) the constitutive law, (Eq. 7.2), becomes quite perceptible when applied to tensile or compression 1D tests in which one of the components is always zero, thus reducing the constitutive law to the scalar equations, (Eq. 7.3) and (Eq. 7.4), according to the type of test (tensile or compression) and to the curves in Fig. 7.3.

Uniaxial tensile test: $$\sigma = (1 - d^+)\bar{\sigma}^+ + (1 - d^-)\bar{\sigma}^- \qquad \textit{(Eq. 7.3)}$$

Uniaxial compressive test: $$\sigma = (1 - d^-)\bar{\sigma}^- = (1 - d^-)E(\varepsilon - \varepsilon^p) \qquad \textit{(Eq. 7.4)}$$

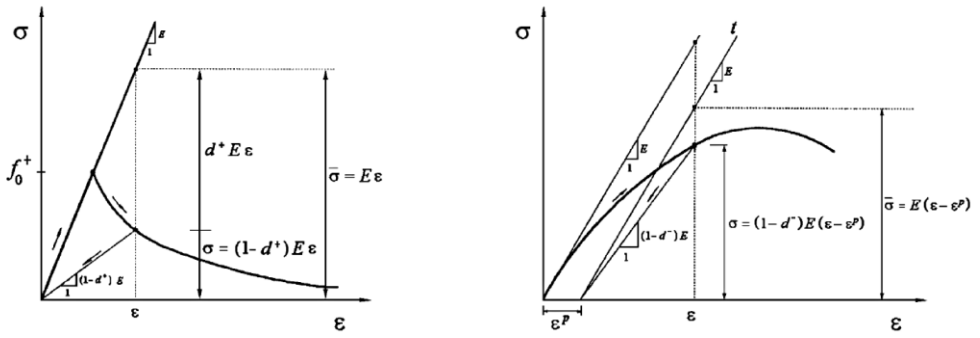

Fig. 7.3 Material behaviour: Uniaxial traction (left) and Uniaxial compression (right) (from Faria, 1994).

As it can be seen in Fig. 7.3 left, in traction the effective elastic tension ($\sigma^+ = E\cdot\varepsilon$) is converted into real tension (σ) directly through the factor ($1-d^+$) and the unloading is made to the origin through a secant modulus $E'=(1-d^+)\cdot E$. In compression, Fig. 7.3 right, the effective tension (σ^-) in a particular point is given by the product of the elastic modulus E by the strain ε on that point affected by the plastic strain $\varepsilon^p\cdot(1-d^-)$. The unloading is not made to the origin, creating plastic strain.

To apply this numerical model on the simulation of a stone masonry structure it is assumed that initially, i.e. before the application of any load or load cycle, the material is isotropic and homogeneous.

The described continuum damage model was implemented in finite element program Cast3M by (Costa, 2004). This software is a powerful code for solving partial differentials equations by the finite element method, developed by the Department of Systems and Structures Modelling (DM2S) of the French Atomic Energy Commissariat (CEA). The software, having an integrated solver with pre- and post-processing, becomes an independent analysis tool. The code is mainly focused on the solving of non-linear mechanical problems including plasticity, buckling, creep, seismic analysis, thermo-plasticity, post-buckling, fracture mechanics etc. Cast3M uses the high level macro-language GIBIANE which gives the user the ability to adapt or extend the GIBIANE code in order to address the needs of his analysis creating involving operators and new objects. Multiple and complex problems in 2D or 3D can be modelled with the use of a comprehensive library of structural finite elements (shell, beam, solid, joint elements etc.) combined with a wide range of constitutive models for engineering materials like masonry, concrete, steel etc.

7.3.2 Finite Element Model

The numerical model was created and calibrated by (Quelhas da Silva, 2012) as a part of another thesis. The main aim of this paragraph is to give a brief description of the calibration phase and about the model used for the analyses in the following sections.

7.3.2.1 Calibration of the Damage Model

The model used in this study was firstly calibrated on the bases of experimental results obtained by monotonic and cyclic compression tests. Nevertheless, the simulation of shear-compression tests show that the model, with those properties, had very high stiffness and brittle behaviour due to which it was experiencing high damage level and unstable behaviour even for low imposed horizontal displacements.

A re-calibration of the model behaviour was needed. This phase was achieved through a phenomenological fitting of the numerical curves to the experimental ones (horizontal force vs. displacement measured at the top of the panels) through a series of uni- and multi-parametric analyses, paying particular attention to the stiffness, strength, ductility and loading/re-loading trajectories. In the case of parameters directly linked to the mechanical properties, it was sought to respect the range of values obtained in the experimental tests, and found in the literature. The obtained parameters are listed in Table 7.1.

Parameters		
YOUN	Elastic modulus	$3.7 \cdot 10^9$ N/m^2
NU	Poisson ratio	0.12
RHO	Density	2500 kg/m^3
GVAL	Tensile fracture energy	50 Nm
FTUL	Tensile stress	$0.15 \cdot 10^6$ N/m^2
REDC	Drop factor for peak tensile stress	0
FC01	Elastic limit compressive stress	$-2.2 \cdot 10^6$ N/m^2
RT45	Equi-biaxial compressive ratio	1
FCU1	Compressive peak stress	$-5.0 \cdot 10^6$ N/m^2
EXTU	Ultimate limit strain	-0.02
EXTP	Reference strain for plastic parameter	-0.0045
STRP	Reference strain for plastic parameter	$-2.2 \cdot 10^6$
EXT1	Fitting point 1 - Strain	-0.0045
STR1	Fitting point 1 – Stress	$-4.0 \cdot 10^6$ N/m^2
EXT2	Fitting point 2 – Strain	-0.023
STR2	Fitting point 2 – Stress	$-4.9 \cdot 10^6$ N/m^2
NCRI	Tensile softening criteria	1

Table 7.1 Parameter values that resulted from calibration process based on shear-compression tests.

A good fit in terms of response envelope was obtained (initial stiffness, maximum resistance and post peak behaviour) and robust convergence of the numerical model under shear-compression cycles was achieved. A comparison between experimental and numerical results is summarized in Table 7.2. Only the dissipated energy is not well simulate by the model. This is mainly due to the inability of this damage model to capture effects like the joints friction, phenomena related to the panels local behaviour.

Specimens	Experimental			Numerical			$H_{max,num}/H_{max,exp}$	$d_{Hmax,num}/d_{Hmax,exp}$	$d_{u,num}/d_{u,exp}$
	H_{max} (kN)	d_{Hmax} (mm)	d_u (mm)	H_{max} (kN)	d_{Hmax} (mm)	d_u (mm)	(-)	(-)	(-)
S2 2.0 N/mm^2	256	5.1	9.6	275	6.0	9.0	1.07	1.20	0.94
S4 1.0 N/mm^2	88	11.3	20.9	89	12.0	22.0	1.01	1.06	1.05
S5 2.0 N/mm^2	121	7.3	9.8	121	7.0	10.0	1.00	0.96	1.02
					average		*1.03*	*1.07*	*1.00*

Table 7.2 Comparison of the numerical and experimental maximum resistance, displacement for maximum resistance and maximum displacement.

7.3.2.2 Numerical Model

The numerical model (Fig. 7.4) was created based on the geometrical data available in the work of (Mazzon, 2010). The geometrical characteristics was treated through a set of steps that involved several auxiliary programs such as AutoCad (Autodesk, 2011) and GiD (CIMNE, 2011), until it was ready to be introduced in the finite element program Cast3M (CEA, 1990).

The masonry was simulated using 8 nodes volumetric elements and the non-linear continuum damage model previously described. The timber elements over the openings were also simulated using 8 nodes volumetric elements but considering linear elastic properties.

The timber floors were simulated using shell elements and considering linear elastic properties. The additional mass of the steel plates on each floor was taken into account on the specific weight of the floors. The steel ties were simulated using 2 node bar elements with a unidirectional linear elastic behaviour (null compression resistance). The timber beams were also simulated with 2 node bar elements. To the timber beams anchored to the walls a linear elastic behaviour was defined, while for the other beams a unidirectional behaviour (working only under compression) was considered.

The reinforced concrete beam was simulated considering linear elastic and isotropic properties. The elastic modulus, E_{RC}, represents the homogenized elastic modulus of both concrete and its reinforcement. The properties of the elements are reported in Table 7.3.

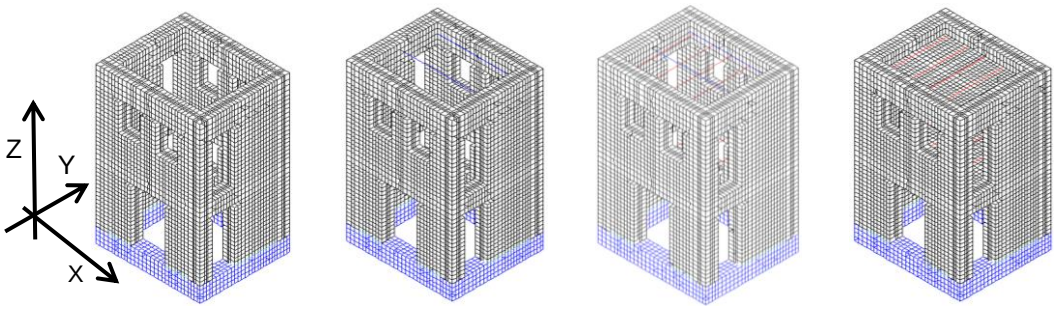

Fig. 7.4 Numerical model of the house. Masonry structure and RC beam (a). Previous model with steel ties in blue (c) or with timber beams in red (c). Complete model (d). (From Quelhas da Silva, 2012)

For the interface between the masonry leaves was considered a linear joint element defined by the transversal (k_t) and normal (k_n) stiffness based on the experimental work of (Costa, 2011), considering the values based on mortar joint (k_t = 1.17E+8 Pa/m, k_n = 1.0E+11 Pa/m).

		ρ (kg/m^3)	S (m^2)	f_t (N/mm^2)	f_c (N/mm^2)	e (m)	E (GPa)	v (-)
RC beam	CUB8	2500	-	-	-	-	30.0	0.20
Timber lintels	CUB8	415	-	-	-	-	10.5	0.37
Timber floors	COQ4	3100	-	-	-	0.05	10.5	0.37
Timber beams - Anchored	SEG2	415	0.108	-	-	-	10.5	0.37
Timber beams – Not Anchored	SEG2	415	0.108	0.0	20.0	-	10.5	0.37
Steel	SEG2	7850	7.9E-5	500.0	0.0	-	210.0	0.30

Table 7.3 Properties of the structural elements of the house.

7.3.3 Modal Analysis

In this section the comparison between numerical modal analysis and dynamic identification on real structure is presented, in order to give an evaluation of the capability of the described model of reproduce the experimentally observed behaviour.

The identification, based on the ambient vibration tests, on the house allowed the verification of the elastic masonry properties for the following boundary conditions: (A) placed outside the shaking table and simply support on the floor, (B) after being placed on the table when this is on the locked position. Afterwards, springs simulating the table effect were also calibrated based on the ambient

vibration tests performed on the house placed on the shaking table, but on unlocked position (C).

During the first dynamic identification test, the structure was placed on the laboratory floor without any further confinement (A). Assuming that the friction of the concrete base with the floor was high enough in order not to have sliding phenomena under ambient vibration, the boundary conditions of the base were considered to be fixed. Hence, in the numerical model, the translational degrees of freedom in the three directions were fixed. No calibration was required as the initial masonry properties, Table 7.1, verified the dynamic characteristics, in particular the frequencies and mode shapes of first three global vibration modes (Fig. 7.5).

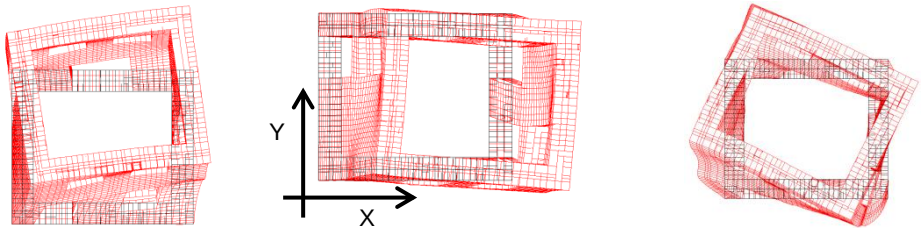

Fig. 7.5 Numerical global mode shapes of the houses. 1st flexural mode - Y direction (left). 2nd flexural mode - X direction (middle). Torsional mode (right). (From Quelhas da Silva, 2012)

After the transportation on the house to the shaking table (B), the measured frequencies for the first global mode shapes decreased. As the table was on the locked position this frequency variation was probably related mostly to damage inflicted to the house during its transportation. And so, the parameters of the behaviour model were re-calibrated based on the dynamic identification results under (B) conditions, but maintaining the resistance and deformability capacity already calibrated for the material.

The fact that from the conditions (B) to (C) the frequencies decreased just by placing the table in the unlocked position, showed the need for taking into account the effect of the shaking table boundary conditions in the model, in order to fit the experimental seismic response of the house, in particular the possibility of the table to rotate along the in-plane orthogonal axis. This was done by considering vertical springs at the base, which stiffness resulted from fitting the numerical frequencies and mode shapes to the first three global mode shapes resulting from ambient vibration experimental tests under (C) conditions. The experimental and fitted numerical frequencies are presented in Table 7.4.

	Frequency (Hz)					
	Experimental			Numerical		
	(A)	(B)	(C)	(A)	(B)	(C)
1st - Flexural Y-Axis	12.1	8.8	7.3	11.6	8.9	7.3
2nd - Flexural X Axis	15.5	11.5	8.6	15.2	11.7	8.6
3rd - Torsional	25.8	19.3	15.6	20.7	15.8	15.2

Table 7.4 Comparison of the experimental and numerical frequencies.

7.3.4 Time histories analyses

The seismic actions (bi-directional) considered in this study were the one measured on the shaking table during the tests, at the base of the house. These results are compared to the experimental ones, namely in terms of damage propagation and patterns.

The tensile damage propagation and crack patterns obtained with the numerical model are compared to the ones observed during the experimental tests, for the different PGA levels, in order to assess if this macro modelling strategy is capable of realistically simulate the behaviour of the house under dynamic loads. The tensile damage propagation and patterns for the different PGA levels are very similar to those observed experimentally. The model was able to capture very realistically the damage distribution and progression on the house during the tests, in particular the:

- Minor cracking for a PGA level of 0.25 g;
- Collapse mechanism that started forming in the pier in Prospect D for a PGA level of 0.30 g, which was aggravated during the following PGA levels and caused the end of the bi-directional load application on the real structure;
- Higher damage at the first floor of the model;
- Damage in the corners of the openings.

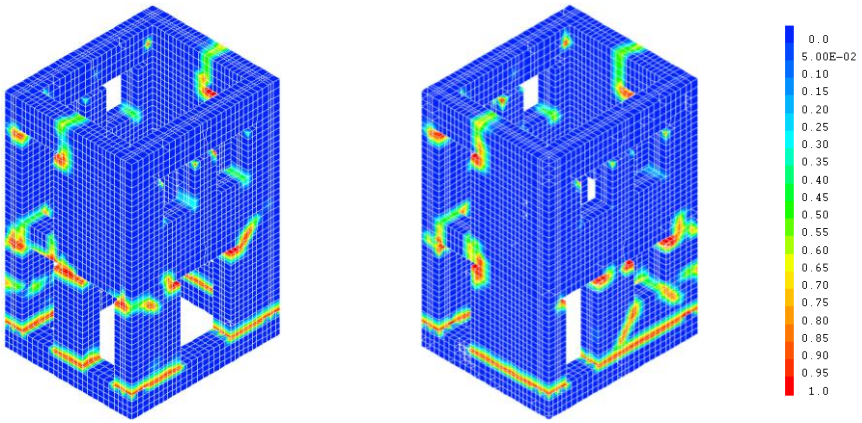

Fig. 7.6 Tensile damage map (d+) at 0.55 g (from Quelhas da Silva, 2012).

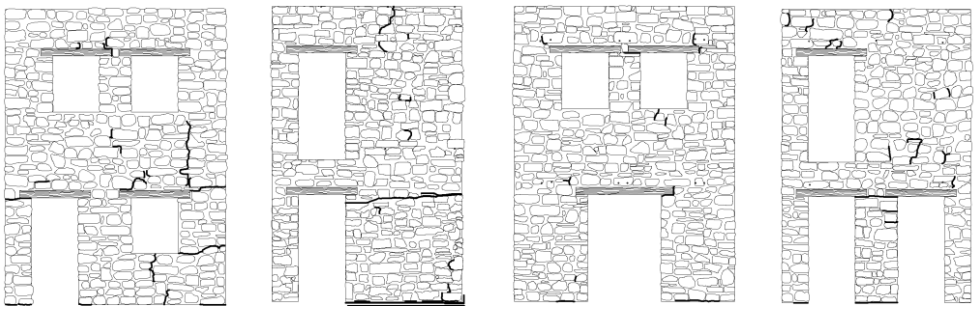

Fig. 7.7 Damage pattern of SM at 0.55 g. (From Mazzon, 2010)

The numerical model was able to simulate until a certain extent the rocking mechanism that affected the overall behaviour of the house, which is clear from the horizontal tensile damage formed at the base of the house, on the interface between the masonry and the RC beam.

The numerically obtained displacements are smaller, i.e. the numerical model appears to be less deformable than the physical one, in particular in the X direction. This can be related to the rocking mechanism that influenced the overall behaviour of the house. Indeed, this type of behaviour allows higher displacements with lower damage levels (Quelhas da Silva, 2012).

7.4 Organization of Work

The procedure for evaluation of equivalent damping, as it was described in Chapter 5, cannot be applied with the above mentioned finite element model, for two reasons. The first is that the non-linear range, i.e. the displacements field between elastic and ultimate limits, is not known. So it is impossible to define a-priori a certain number of target displacements. The second reason regards the unfeasibility to perform dynamic analyses in a iterative way in order to reach a pre-determined level of displacement. This is due to the high computational effort that the model requires for a dynamic analysis.

For these two reasons, the first two steps of the procedure described in Chapter 5 cannot be followed. It was chosen to perform dynamic analyses considering several values of PGA, which were defined a-priori. Furthermore, due to the time needed to perform an analysis, it is not possible to repeat the procedure for all Time Histories (THs) considered in Chapter 5. Indeed, using an Intel Core 2 Duo E8400 processor at 3.00 GHz with 4 GB of RAM DDR2 at 332 MHz, the analyses take in average 4 days to run, considering a time history of 10 s.

7.4.1 Selection of Time Histories and PGA Levels

Ten THs for both soil A and soil D were previously considered. For each soil type, the minimum number that is reasonable to be considered is three, in a way that each one is representative of the average, the maximum or the minimum of the expected response. The chosen parameter for the selection of the THs was the Arias Intensity (Arias, 1970), as it is representative of both frequency content and amplitude of seismic motion.

Arias Intensity (I_A) is defined by (Eq. 7.5), whereas Fig. 7.8 shows the normalized Arias Intensities for time histories on both soil A and D.

$$I_A = \frac{\pi}{2g}\int_0^{\infty} a(t)^2 dt \qquad \textit{(Eq. 7.5)}$$

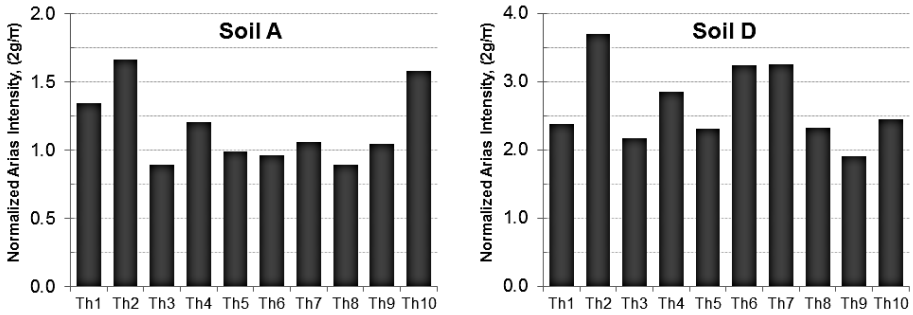

Fig. 7.8 Normalized Arias Intensity for soil A (left) and soil D (right) time histories.

Since the extreme values may lead to strongly under- or overestimated evaluations, it was chose to not consider the THs related to the effective maximum and minimum value of I_A. So the selection was limited to the other 8 THs, considering those related to maximum, minimum and average value of I_A. In this way, time histories number 3, 4 and 10 were chosen for soil A, and time histories 3, 4 and 7 were chosen for soil D. Fig. 7.9 shows the elastic displacement spectra of chosen THs, using the colour light blue, orange and red for the spectra of TH related to, respectively, the minimum, average and maximum value of Arias Intensity (excluding the extreme values). The code recommended spectra are plotted in blue continuous line, whereas the spectra of the other THs are plotted using dashed grey lines.

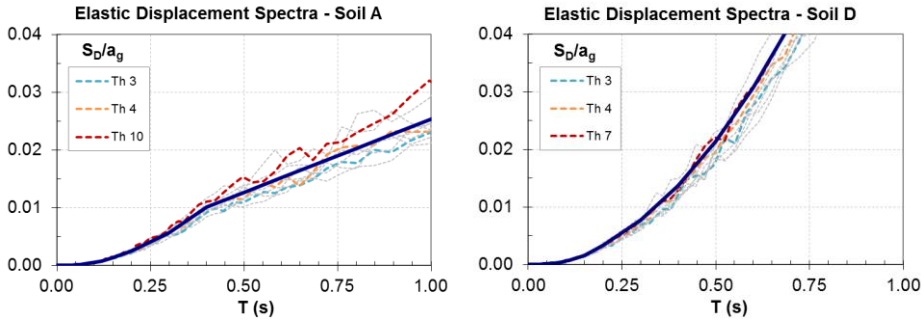

Fig. 7.9 Elastic Displacement Spectra of chosen Time Histories for soil A (left) and soil D (right).

For what concerns the choice of PGA levels, the results obtained from the tests on shaking table were taken into account. The experimental tests were carried out using a record of the earthquake that happened in Montenegro in 15/4/1979, considering the two main directions X and Y, with increasing levels of nominal PGA (each 0.05 g) by simply scaling the initial input accelerations to the desired step level. On the PGA levels for dynamic analyses, the PGA measured by the accelerometers placed in the X and Y directions attached to the RC base of the houses were considered.

The results are summarized in Table 7.5 in terms of PGA, nominal and measured, and corresponding maximum top displacement. Assuming that the ideal elastic limit is related to a drift limit equal to 0.1% (top displacement equal to 3.6 mm), it is obtained a PGA level of about 0.20 g.

PGA (nominal)	PGA (measured)		Top displacement	
	X	Y	X	Y
(g)	(g)	(g)	(mm)	(mm)
0.10	0.078	0.101	2.02	1.73
0.20	0.120	0.156	2.58	3.07
0.25	0.182	0.199	3.25	3.55
0.30	0.164	0.268	7.14	7.59
0.35	0.180	0.315	5.05	5.26
0.40	0.195	0.424	5.86	5.73
0.45	0.206	0.400	8.35	9.11
0.50	0.251	0.417	11.77	18.78
0.55	0.280	0.447	14.47	21.31
0.60x	0.299	0.199	15.35	
0.65x	0.317	0.277	17.95	
0.70x	0.546	0.304	28.18	
0.70x(2)	0.594	0.348	36.08	

Table 7.5 SM model: experimental PGA and maximum top displacement.

Each time history was applied, separately, in both principal directions, X and Y. Since the aim of this study is to evaluate the equivalent damping for the whole structure beyond the elastic phase, it was initially considered the PGA levels starting from 0.30 until 0.75 g, each 0.15 g. During the analyses, it was found that drift levels, related to the same PGA, are sensitively lower for soil A than for soil D and lower for analyses in X direction than those in Y direction.

In order to obtain drift values comprised between 0.1 % and 1.0 % the PGA levels listed in Table 7.6 were used. The total number of performed analyses is 45, 27 in X direction and 18 in Y direction.

Direction	PGA - Soil A (g) (g)	PGA - Soil D (g) (g)
X	0.30, 0.45, 0.60, 0.75, 0.90	0.30, 0.45, 0.60, 0.75
Y	0.45, 0.60, 0.75	0.30, 0.45, 0.60

Table 7.6 PGA levels considered for the analyses.

7.5 Methodology

For each TH and each PGA level considered, a dynamic analyses with the described model was performed. The considered material properties were those listed in Table 7.1 for masonry and in Table 7.3 for the other materials. As boundary conditions, the house was considered as fixed at the base. The next step is the estimation of properties of equivalent SDOF system. Then, the procedure described in §5.2 can be applied starting from step 4.

7.5.1 Determination of Equivalent SDOF System

The results of the analyses allow the determination of the displacement shape, that is evaluated checking the displacements in the considered direction of the geometric barycentre of floors, at the attainment of the maximum top displacement. The whole structure can be schematized as a n-DOF oscillator, considering the mass lumped at each intermediate node. At this point, (Eq. 2.22), (Eq. 2.23) and (Eq. 2.24) can be used to computed the characteristics of the equivalent SDOF system, i.e. target displacement (Δ_d), effective height (H_e) and mass (m_e), respectively. The effective period of equivalent SDOF system is computed by inverting (Eq. 2.20), that is reported here for simplicity:

$$T_e = 2\pi \cdot \sqrt{\frac{m_e}{K_e}} = 2\pi \cdot \sqrt{\frac{m_e \Delta_d}{V_b}} \qquad \textit{(Eq. 7.6)}$$

where V_b is the base shear corresponding to maximum top displacement.

Since the structure has two storey, it could be consider 2 DOF, one for each floor. The tributary mass for each DOF can be computed by sum of floor mass with the half of masses of the walls masonry of both upper and lower storeys. Naturally, for the top DOF, only the lower storey, i.e. the second, has to be considered. This approach is commonly followed with frame buildings, for which the majority of total mass is due to floors. For what concern masonry buildings, instead, the majority of total mass is due to masonry walls, hence such an approach, for a two-storey building, leads to neglect about ¼ of the actual mass.

In order to evaluate the limits of this strong approximation, it was also considered a second method, based on that proposed by (Adhikari et al., 2008) for massive tall piers of long span bridges. More precisely, the whole structure was schematized as 4 DOF, considering 2 DOF placed at middle inter-storey level in addition to the 2 DOF at floors level. In such a way, for a two-storey building, only about 1/8 of the actual mass is neglected. In the following, the first method will be indicated with 2DOF, the second with 4DOF.

7.6 Results of the Analyses

7.6.1 Displacement Shape

The main aim of this section is to describe the displacements shapes found by dynamic analyses. It is important to point out that, as reported in §2.5, in absence of specific indication a linear displacement shape is normally assumed, i.e. displacement proportional to height. Since displacements obtained from numerical analyses are closer to the experimental results in Y direction, § 7.3.4, in this section the results obtained for the analyses in Y direction are presented. However, the results obtained from the analyses in X direction do not sensitively differ.

Fig. 7.10 shows the obtained displacement shapes, normalized to maximum displacement in order to be compared at different levels of PGA. It can be noticed that they are non-linear with height, with a shear-type deformed shape. Furthermore, the middle-storey DOFs showed displacements that can be consider

linear with those at storey levels. For this reason, in the following, the displacement shape will be identified by normalized displacement at first floor (Δ_{FF}/Δ_{top}).

Given a level of PGA, top displacements (Δ_{top}) are not the same between two soil types. More precisely, at the same level of PGA, Δ_{top} is greater for soil D than for soil A. It has been found that for a PGA of 0.30 g on soil D, the corresponding total drift ($\Psi_{tot} = \Delta_{top}/H_{tot}$) is about 0.25%. The same level of deformation is reached by analyses on soil A with a PGA of about 0.45 g (Fig. 7.11, left). Furthermore, the same levels of PGA, for both soils, are related to first interstorey drift (Ψ_{FF}) of about 0.30% (Fig. 7.11, right).

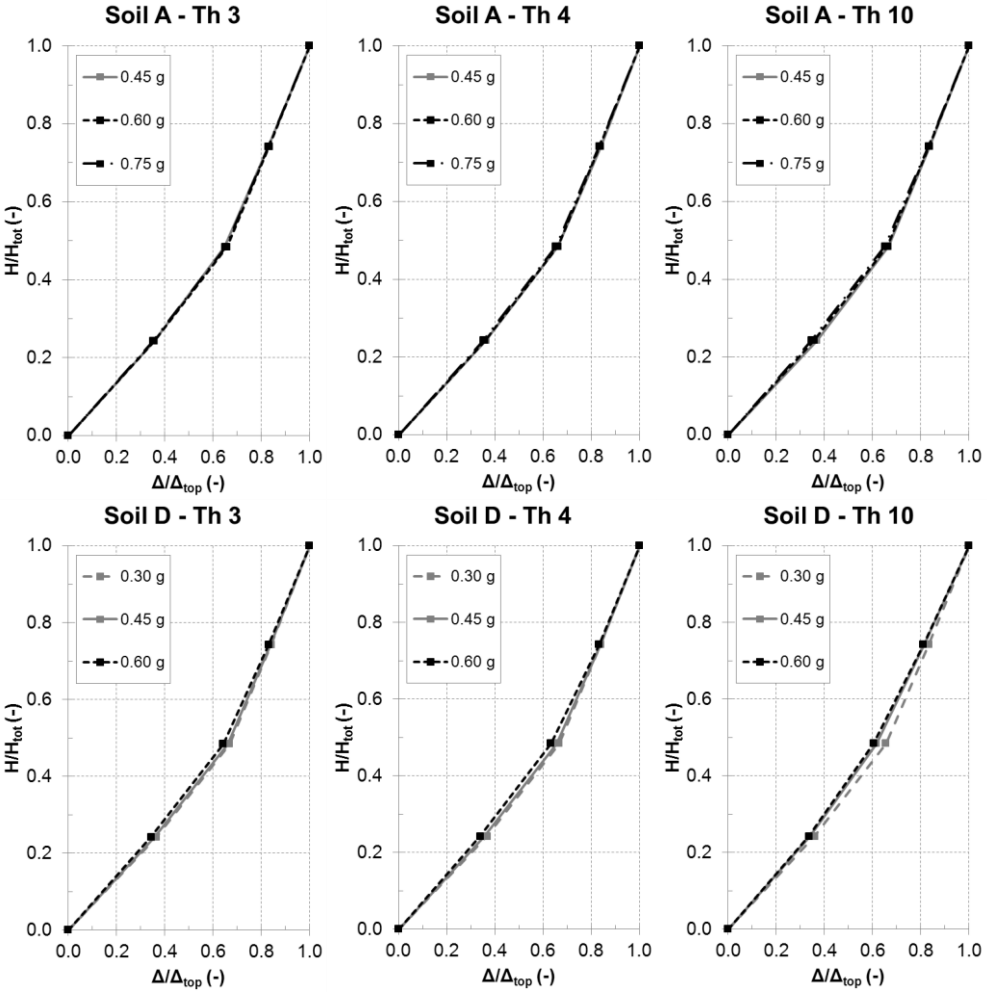

Fig. 7.10 Normalized displacement shapes at several level of PGA for soil A (above) and soil D (below).

Displacement shape is identified by Δ_{FF}/Δ_{top} equal to about 0.65÷0.70, independently from PGA level. This means that displacement shape remains constant for different levels of damage. This fact appears to be not consistent with experience, according to which Δ_{FF}/Δ_{top} should increase with the increasing of damage. Probably the model is not able to reproduce, with enough accuracy, the actual response when too large inelastic deformations are required. However, this limit does not influence the following observations. In addition, the interstorey drift can be considered as the meaningful parameter in order to describe the evolution of damage, so in the following sections each parameters will be referred to Ψ_{FF}.

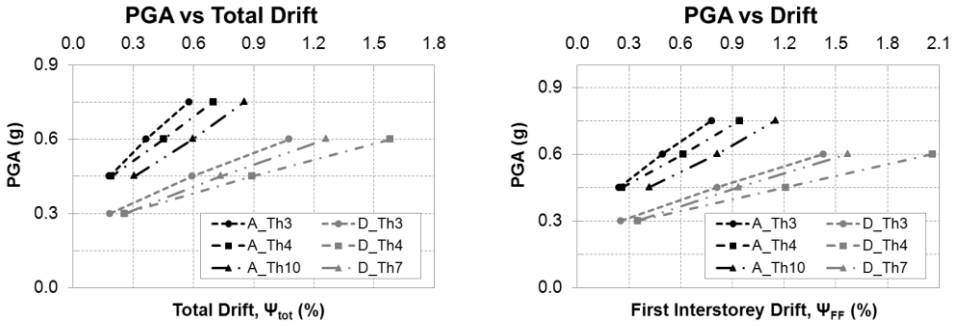

Fig. 7.11 PGA versus Total (left) and First Interstorey (right) Drift.

7.6.2 Equivalent SDOF system

The evaluation of effective displacement shape allows the definition of equivalent SDOF system. According to the number of DOFs chosen in the schematization, the characteristics of equivalent SDOF system can be different.

The first quantity that can be calculated is target displacement Δ_d, which represent the displacement of equivalent SDOF that corresponds to Δ_{top}. Fig. 7.12 shows the comparison between normalized target displacement ($\Delta_d^* = \Delta_d/\Delta_{top}$) plotted against Ψ_{FF}, obtained by two methods (2DOF and 4DOF) on both soil types. The 2DOF method leads values of Δ_d^* that are higher than those of 4DOF, and the type of soil seems not have an influence on this parameter. In addition, giving the same method, values of Δ_d^* are constant with the increase of Ψ_{FF}. The average values are 0.82 and 0.77 for 2DOF and 4DOF, respectively.

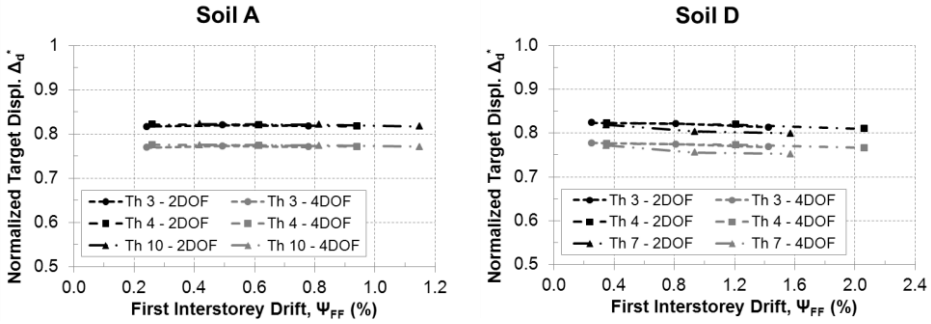

Fig. 7.12 Normalized Target Displacement vs First Interstorey Drift for soil A (left) and D (right).

Fig. 7.13 shows the comparison between normalized effective heights, H_e^*, plotted against Ψ_{FF}, obtained by two methods (2DOF and 4DOF) on both soil types. It is easy to notice that 2DOF method leads to higher values of H_e^* than those of 4DOF, and furthermore that the type of soil seems not to have an influence on this parameter. Both methods give a constant values of H_e^* with the increase of Ψ_{FF} so it is reasonable to consider H_e^* independent of interstorey drift - and so from damage level - and from soil type. The obtained mean values are 0.73 and 0.68 for 2DOF and 4DOF, respectively.

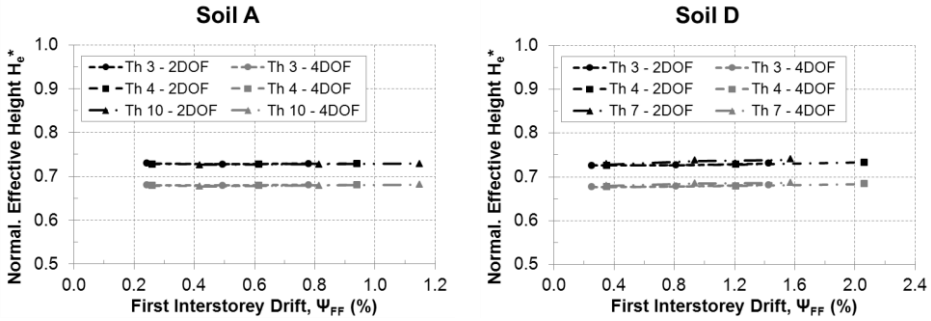

Fig. 7.13 Normalized Effective Height vs First Interstorey Drift for soil A (left) and D (right).

Regarding the effective mass, it is important to point out that neither 2DOF nor 4DOF methods take into account the total mass of the house. Indeed, the former neglects half of the masonry wall mass of ground floor, the latter a quarter. This means that, despite the total mass is 21905 kg, the masses taken into account by 2DOF and 4DOF methods are 17406 and 19660 kg, respectively.

Fig. 7.14 shows the comparison between normalized effective mass, $m_e^* = m_e/m_{tot}$, plotted against Ψ_{FF}, obtained by the two methods on both soil types. The 2DOF method gives lower values than those obtained with 4DOF method,

whereas soil type has not an influence on this parameter. The obtained mean values are 0.76 and 0.81 for 2DOF and 4DOF, respectively.

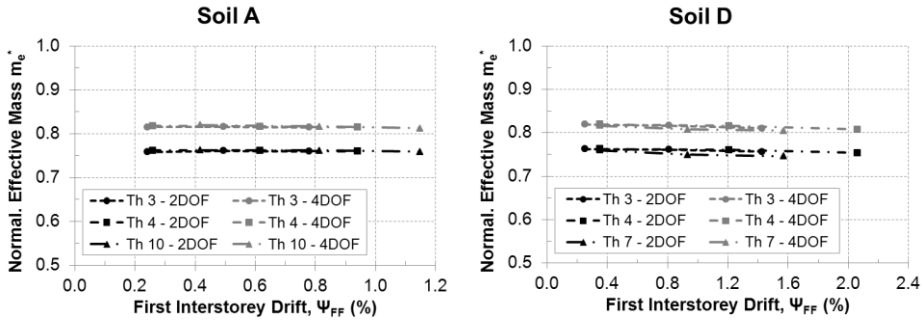

Fig. 7.14 Normalized Effective Mass vs First Interstorey Drift for soil A (left) and D (right).

The characteristics of equivalent SDOF system are independent of Ψ_{FF} because the displacement profile is constant with the evolution of damage, as showed in the previous paragraph. The differences of SDOF characteristics obtained by two method are mainly due to different amount of total mass that is taken into account. Indeed, the displacement shapes can be considered the same, since displacements at middle-storey DOFs can be considered linear with those at storey level, as observed in the previous paragraph. This is confirmed by the equivalent periods obtained by two methods, which are showed in Fig. 7.15. It can be noticed that the curves related to different methods are almost perfectly superimposed, and so it can be concluded that, for this structure, schematization with 2DOF is enough accurate.

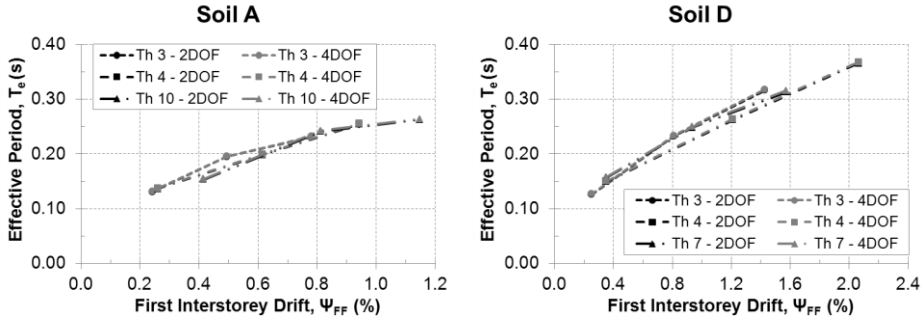

Fig. 7.15 Effective Periods at several level of PGA for soil A (left) and D (right).

7.6.3 Equivalent Viscous Damping

In the previous paragraph it has been proven that T_e is independent from number of DOF considered in the schematization of this real structure. However, other characteristics of equivalent SDOF are dependent of such a choice, above all Δ_d. This means that, in order to obtain the same effective period, the values of equivalent viscous damping, obtained with the two methods, have to be different. More precisely, since Δ_d for 2DOF is greater than the one for 4DOF, the values of ξ_{eq} obtained with 2DOF will be lesser than those with 4DOF.

Fig. 7.16 shows the comparison between obtained values of ξ_{eq}, according to 2DOF and 4DOF, and damping curves for SDOF described in §6.3.1. Black indicators are referred to 2DOF schematization, the grey indicators to 4DOF, whereas circular indicators are referred to analyses in X direction and triangular indicators are referred to analyses in Y direction. As expected, damping values for 4DOF are greater than those for 2DOF. The difference is more or less constant, with an average of about 20%. On the contrary there is no difference between results obtained from analyses in different directions, since the two point clouds are almost superimposed.

The limited total number of analyses (24 on soil A and 21 on soil D) does not allow to identify in a reliable way the curves of MDOF using statistical method. For this reason, in the following, only the comparison between the obtained values and SDOF curves will be described.

It can be noticed that for drift less than 0.1%, the obtained values are very small, generally smaller than 2%. Beyond this limit, damping values show a sudden increase. For soil type A, it can be said that the majority of values are comprised between squat curves and slender-2.0 curves. For soil D, instead, it can be noticed that some values, about the half, are almost superimposed to slender-1.0 curves, a couple (2DOF and 4DOF for the same analysis) is below and the others are above these curves. The couples that are above are closer to slender-2.0 and S2 curves, or in any case they are comprised between these and slender-1.0 curves.

Furthermore, it seems that MDOF damping values are higher on soil A compared to those on soil D. In any case, due to already mentioned limited number of analyses, neither it is possible to investigate more in detail this issue, nor make further remarks. On the other hand, this comparison allows to confirm the validity of curves described in §6.3.1, since the great majority of damping values are comprised between higher and lower curve.

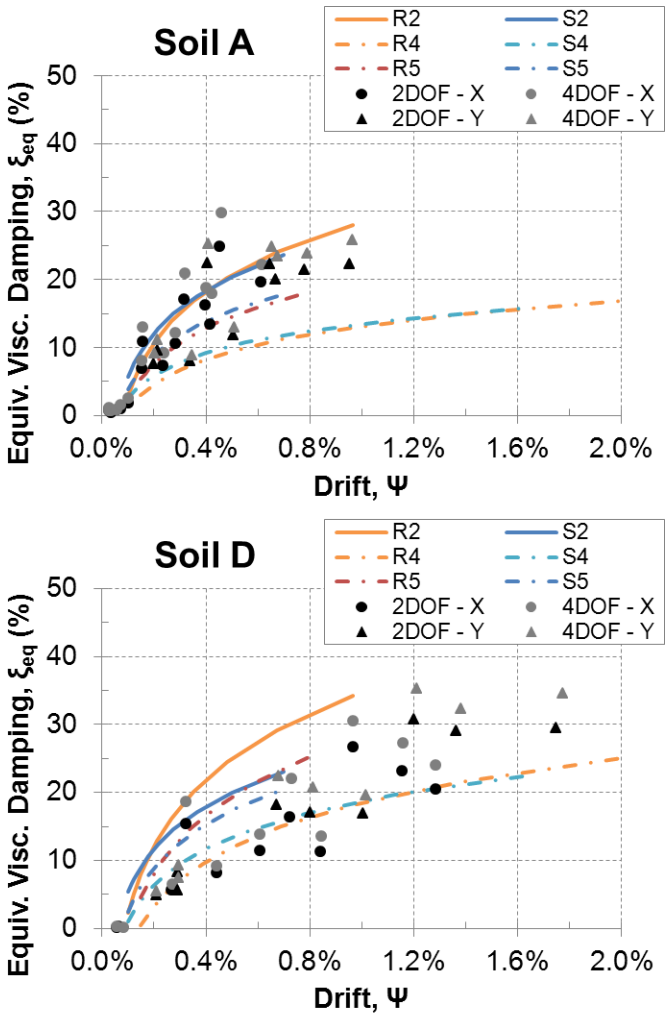

Fig. 7.16 Comparison between damping curves for SDOF, related to drift, and damping for MDOF on soil A (above) and soil D (below).

7.6.4 Damping Correction Factor

Fig. 7.17 shows the comparison between effective ratio d_{IN}/d_{EL}, η _eff, and damping corrector factors obtained in §0. In these graph curve related to coefficient α recommended by code (5) is called η_code, whereas the one related to coefficient α obtained by regression analysis is called η_fit. The used values of coefficient α are those proposed in §6.3.3, i.e. 0.5 and 2.0 for soil type A and D, respectively.

It can be noticed that effective η obtained by 2DOF and 4DOF have the same trend, that confirm the equivalence of two schematizations for this structure. Furthermore, this trend seems to be well correlated with the function adopted to

describe η factor in function of equivalent damping. This confirms the validity of the function expressed by (Eq. 5.3) in order to evaluate η factor. In addition, very similar results were obtained by analyses in different directions, as previously noted for damping values.

For what concern the capability of η factor, using α recommended by code or obtained by fitting, it can be noticed that the analyses on two soil types have given slightly different results. For soil type A, η_fit approximates η_eff in a satisfactory way. η_code, instead, overestimates the effective values in all the range of damping variability. The values of coefficient R^2 are 0.91 and 0.35 for η_fit and η_code, respectively.

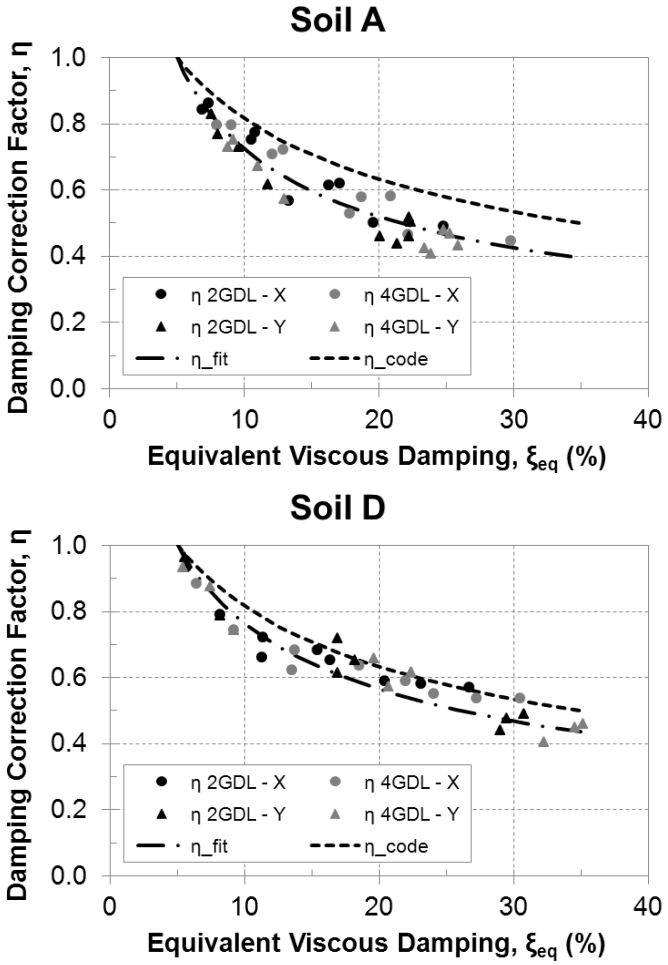

Fig. 7.17 Comparison between effective damping correction factor and curves provided by code and obtained for SDOF. Results on soil A (above) and soil D (below).

For soil type D, instead, η_fit approximates η_eff in a satisfactory way for damping lesser than 15% and higher than 25%, whereas slightly underestimates effective values for intermediate damping values. On the contrary, η_code overestimates the values of η_eff related to damping lesser than 15% or higher than 25% and approximates in a better way the other values. The values of coefficient R^2 are 0.91 and 0.86 for η_fit and η_code, respectively.

7.7 Summary and Conclusions

An application of the proposed procedure, for determination of equivalent viscous damping on MDOF system has been presented. The real structure has been modelled by finite element model with a damage model that has been calibrated on the bases of experimental results of shear-compression tests. With this model, several time-history analyses have been performed, with the aim of determine the peak displacement response. Equivalent SDOF has been determined with two methods, i.e. taking into account a schematization with 2 or 4 DOF. Then the procedure presented in Chapter 5 has been applied, and the obtained results have been compared with those related to single walls presented in Chapter 6.

The main results gained in this phase of work are:

- For such a simple structure, displacement shape can be considered independent from the number of DOF considered in the schematization of MDOF, since inter-storey displacements are linear with those at storey levels. This is confirmed by the fact that effective periods obtained considering a different number of DOF are the same.
- Displacement shape can be identified by normalized displacement at first floor, Δ_{FF}*. This parameter seems to be independent of increasing damage level, which is identified by first inter-storey drift (Ψ_{FF}). It can be considered constant and equal to about 0.65÷0.70.
- Since displacement shape can be considered constant at several damage levels, i.e. interstorey drift, the equivalent SDOF system is identified by an effective height of about 0.7 times the total height and an effective mass around 0.8 times the total mass.
- The obtained values of equivalent damping are very small, less than 2%, for drift less than 0.1%, then they sudden increase. For soil type A they are all comprised between the obtained curves for squat and those for slender-0.2 panels. For soil type D, instead, they are comprised between the obtained curves for slender-2.0 and slender-1.0 panels. It can be concluded that this

application confirm in general the results gained in Chapter 6, although it is not yet possible to identify the most reliable curve.

- The values of effective factor η are in good agreement with the function used in the codes. These values have been compared with η-function, using the values of α proposed by codes and those obtained by regression. The obtained values of α coefficient lead to estimate in a satisfactory way the effective η, for soil type A, whereas, for soil type D, it involve a slightly underestimation of effective η for damping comprised between 15% and 25%. However, it can be said that proposed values of coefficient α give more reliable estimation of effective η, since the obtained values of coefficient R^2 are higher than those obtained with the value of α proposed by codes.
- The observed limits are mainly due to limited number of performed analyses. There is the need to carry out further analyses, considering a wider number of time histories and structural configurations. However, the obtained results allow to gather these firsts considerations.

8 CONCLUSIONS

8.1 Introduction

In the present chapter, some general remarks about the research carried out and the main conclusions obtained by the analyses are presented.

The main aim of this study was that of contributing to the knowledge of parameters typical of non-linear cyclic behaviour of masonry systems subjected to in-plane seismic actions. Two masonry types were taken into account: modern reinforced masonry and historical stone masonry strengthened by hydraulic lime-based grout injections.

A new hysteretic model, starting from the one proposed by (Tomaževič & Lutman, 1996) and based on results of shear-compression tests was developed. This model was used within a procedure for the determination of equivalent viscous damping. The results of this procedure were analysed and discussed, obtaining information not only about damping factor, but also on the ratio between inelastic and elastic displacements. In addition, the procedure was also applied to a MDOF structure, obtaining information on the determination of equivalent SDOF system, and partially confirming the results obtained on single walls.

8.2 Analysis and Modelling of Cyclic Behaviour

The analysis of results obtained by cyclic shear-compression tests allowed to identify the attainment of four limit states, for both masonry types. The second LS is related to the failure mode, and it is called critical limit state. For RM, it can be related to a flexural failure or a shear failure. In the former case, critical LS is identified by yielding of vertical bars (ψ = 0.50-0.70%), in the latter by the opening of first diagonal crack (ψ = 0.30%). For SM, critical limit is identified by opening of first diagonal crack for squat and slender-2.0 specimens (ψ = 0.20%), whereas for slender-1.0 specimens it is related to rocking mechanism (ψ = 0.35%).

The ultimate LS, that can be identified by maximum displacement capacity, is characterized by a wide variability. Given the importance of this LS on the safety evaluation, it is reasonable to consider a conservative value. Assuming this value

as the lower limit of variability range, it can be said that the studied RM system is characterized by ultimate drift of 0.8% and 2.0% for shear and flexural behaviour, respectively.

For what concern SM, it has been noted that ultimate capacity for squat specimens is similar to that of slender-2.0, i.e. about 0.7-0.9%, whereas slender-1.0 are characterized by about a twice in amount displacement capacity. The collapse was associated to shear mechanism for all the specimens, even if initial damage pattern was due, in some cases, to other mechanisms (i.e. rocking). Since the considerable displacement capacity obtained by slender-1.0 specimens is influenced by rocking mechanism, and considering that also for these panels the failure was due to shear, it is reasonable to consider the ultimate capacity limit as 0.7% independently from aspect ratio and vertical stress.

The model proposed by (Tomaževič & Lutman, 1996) was used for modelling of experimental tests. Starting from shortcomings of this model, when applied to the masonry types studied in this work, a new hysteretic model was developed. The input parameters of the model are four limit states, which define the idealized envelope curve, and two coefficients, which are calibrated by imposing the equality of both the input and dissipated energies between experimental and modelled loops. The unloading rules were defined on the basis of experimental observations, in order to reproduce the actual shape of hysteresis loops. Reloading rules were established in order to ensure the degradation of stiffness with the increasing of maximum displacement.

The model is capable of reproducing the actual behaviour for both failure modes of RM and, with a little variation, also for SM. In particular, the model was enough accurate in modelling of dissipated energy by hysteresis, since, for each specimen of both masonry types, the relative error between modelled and experimental dissipated energy is in average lower than 10%. Hence, the model was implemented in Matlab environment, in order to carry out dynamic analyses. For what concern the integration of equation of motion, it was used the Newmark constant average acceleration scheme.

The model was then tested, performing a large number of analyses using several time histories, in order to highlight and debug eventual instability. Lastly, the model has proven to be robust and capable of performing non-linear analyses with very low computational effort, and it was used within an iterative procedure for the determination of equivalent damping.

8.3 Results of the Analyses

The results of the analyses showed that equivalent viscous damping increase for increasing inelastic displacements, when period corresponding to secant stiffness is included in spectrum plateau. Otherwise damping can be considered constant.

For reinforced masonry, failure mode is the most sensitive parameter for the evaluation of damping. Conversely, although the investigated range is quite limited, it has been observed an independency of the pre-load level applied. In addition, shear curves, due to low period shifts, are independent from soil type. Flexural curves, instead, have period shift greater than those of shear, and for this reason they are dependent from soil type. For this failure mode, at the same drift level, soil D involves damping value higher by about 30% compared to soil A. Since spectra of soils A and D can be considered as the limits of responses for several types of soil, the values of damping found for these soil types represents a reliable range of variability of damping.

Assuming that critical LS can be reasonably considered as damage LS, shear behaviour is characterized by a damping value of 7%, independently from soil type. Flexural behaviour involves values that range between 8 and 10%. Since this difference is quite low, it can be concluded that, in the case of damage limit state, equivalent damping can be considered independent from soil type also for flexural behaviour. For practical use, it would be reasonable to use a conservative value of 8%, that is very close to the value proposed for shear behaviour. Hence, for damage limit state, it is reasonable to use the unique value of 7%, independently from soil type and failure mode. For what concern ultimate LS, assuming the limits mentioned so far, shear behaviour is characterized by a damping value of 12%, whereas flexural behaviour involves values ranging between 12 and 16%, according to soil type. The former is related to soil of type A, the latter to soil of type D. In the case of other types of soil, intermediate values could be used.

For what concern the strengthened stone masonry considered in this study, several difficulties arose in the interpretation of results. These were due, on one hand, by the high level of pre-load applied during the experimental tests, and on the other by the high non-homogeneity of this material, that increases the probability of local phenomena, which influence the global behaviour more than it occurs in modern masonry. In order to obtain more reliable results, the analyses should be based on a wider number of experimental tests.

However, the obtained results for slender-1.0 panels can be considered as a first indication for practical use. For these panels, at lower drift levels, an independency from type of soil was observed. Since the suggested ultimate displacement capacity, i.e. drift of 0.7%, is included in this range, the same values of damping,

independently from soil type, can be considered. Assuming, as for RM, that critical LS can be reasonably considered as damage LS, the suggested values of damping are 9% and 14% for damage and ultimate LS, respectively.

Relationship between elastic and inelastic displacement is more than proportional. A good approximation of numerical results can be obtained using a power function. For what concern RM, the obtained relationships are in good agreement with results gained for damping. Indeed, they confirm, for both failure modes, the independency from vertical stress level, and also, in the case of shear behaviour, from soil type. Furthermore, these functions, for low values of displacement, are very close to each other, confirming that at damage limit state the equivalent damping can be considered independent from type of soil for both failure modes. For SM, instead, this phase of work highlighted the limits due to the great variability of experimental results, linked to limited number of experimental tests on which the analyses were based.

Values of effective ratio between inelastic and elastic displacement, i.e. Damping Correction Factor, are well correlated with formulation proposed by several codes, among which (EN 1998-1, 2004) and (DM 14/01/2008, 2008). Calibration of the coefficient α used in this formulation led to values independent from failure mode and level of vertical stress for both masonry types, and slightly different according to soil type. For RM, the values of 1.0 and 1.9 were obtained, respectively for soil A and D. For SM, similar values were obtained, that are 0.5 and 2.0 for soil type A and D, respectively. Since the variability of coefficient α does not have an appreciable effect on the damping correction factor, it would be possible to give a unique value for both soil types. In addition, since the range of variability of this coefficient is similar for both the studied masonry types, it is reasonable to consider the same value for both the masonry types. This value should be representative also of other soil types, which were not taken into account in this study. So it is conservative to consider the value obtained for soil D, that basically leads to consider the formulation included in the previous version of EC8, that is also suggested by (Priestley et al., 2007).

8.4 Multi-Degree of Freedom

The structure on which DDBD method was applied, is historical stone masonry building, strengthened by grout injections. It is obvious that, for this type of masonry, the method is used as an assessment of the expected performance, rather than an actual design method. The studied structure is a simple two-storey

building. For this kind of structures, a schematization with two degree of freedom can be considered enough accurate.

Displacement shape is identified by normalized displacement at first floor, Δ_{FF}*, equal to 0.65÷0.70. According to this assumption, the effective height and mass can be considered constant, the former around 0.7 times the total height, the latter around 0.8 times the total mass. These results show that simplified determination of equivalent SDOF system, as described in §2.5, cannot be considered reliable. This is due to non-linearity of displacement shape.

The obtained values of equivalent viscous damping are comprised in the variability range of those found by single walls, with some differences according to type of soil. Hence, even if this phase of work does not allow to gain reliable information for practical use, it has to be observed that it confirms the general validity of results obtained for single walls. The limits are mainly due, on one hand, to the limited number of analyses performed on MDOF system, i.e. three time histories for two soil types and one structural configuration, and on the other, on the limited number of experimental configurations on which analyses on SDOF systems are based. Notwithstanding, the validity of proposed value of coefficient α is confirmed for MDOF structures.

8.5 Future Work and Developments

Further developments of the research carried out on reinforced masonry system could be aimed to investigate the evaluation of equivalent damping related to different systems, in order to confirm the soil independency of shear type of behaviour and determine formulations related to flexural behaviour for several soil types, if necessary. In addition, there is the need to take into account a wider range of pre-load levels, in order to further investigate the independency of equivalent damping from pre-load. Another development is represented by the application of our method to MDOF systems, with the aim to validate the results obtained for single walls. In addition, such an application would be aimed also to the determination of equivalent SDOF system for this masonry type, considering several aspects, such as structural configuration, number of storey etc…

For what concern stone masonry, since the variability of experimental results, a first important development could be that of taking into account a wider experimental data-base, in order to properly consider the variability, due to local phenomena, of this masonry type, and also more realistic vertical stress levels.

A general issue for both masonry types is represented by the use of recorded earthquake ground motions, in order to take into account, in addition to soil type, also the magnitude and distance from epicentre on the evaluation of damping.

Finally, the calibrated damage model can be used to perform parametric analyses, in order to investigate the influence of several aspects, such as structural configuration, geometry, floor stiffness etc…, on the displacement shape and on the other parameters. In addition, a wider number of time histories could be used, in order to allow a significant averaging of results.

9 BIBLIOGRAPHY

Abrams D. P. (2001) "*Performance-based engineering concepts for unreinforced masonry building structures*". Progress in Structural Engineering and Materials. 3(1): 48-56pp.

Adhikari G., Petrini L. and Calvi G. M. (2008) "*Is Direct Displacement Based Design Valid For Long Span Bridges?*". Proceedings of the 14th World Conference on Earthquake Engineering, International Association for Earthquake Engineering. Beijing, China, October 12-17, 2008. DVD Edition.

Ahmad N., Crowley H., Pinho R. and Ali Q. (2010) "*Simplified formulae for the displacement capacity, energy dissipation, and characteristic vibration period of brick masonry buildings*". Proceedings of the 8IMC-International Masonry Conference. Dresden, Germany, 4-7 July 2010. 11(2), pp. 1385-1394.

Arias A. (1970). A measure of earthquake intensity. Seismic Design for Nuclear Power Plants. Hansen R. J., MIT Press: 438-483pp.

Aschheim M. A. and Black E. F. (2000) "*Yield Point Spectra for Seismic Design and Rehabilitation*". Earthquake Spectra. 16(2): 317-336pp.

Autodesk. (2011). Available at: http://usa.autodesk.com.

Benedetti D. and Tomaževič M. (1984) "*Sulla verifica sismica di costruzioni in muratura*". Ingegneria Sismica. 1(0): 9-16pp.

Bernardini A., Giuffrè A. and Modena C. (1984) "*Reinforced hollow clay brick masonry shear walls under seismic action*". Proceedings of the 8th World Conference on Earthquake Engineering. San Francisco, USA.

Bernardini A., Modena C., Lazzaro G. and Valluzzi M. R. (1997) "*Cyclic behaviour and modelling of reinforced masonry panels*". Proceedings of the 11th International Brick/Block Masonry Conference. Shangai, China, October 14-16, 1997.

Blandon C. A. and Priestley M. J. N. (2005) "*Equivalent Viscous Damping Equations For Direct Displacement Based Design*". Journal of Earthquake Engineering. 9(sup2): 257-278pp.

Bommer J. J. and Elnashai A. S. (1999) "*Displacement Spectra For Seismic Design*". Journal of Earthquake Engineering. 3(1): 1-32pp.

Bommer J. J., Elnashai A. S. and Weir A. G. (2000) "*Compatible acceleration and displacement spectra for seismic design codes*". Proceedings of the 12th World Conference on Earthquake Engneering.

Bommer J. J. and Mendis R. (2005) "*Scaling of spectral displacement ordinates with damping ratios*". Earthquake Engineering & Structural Dynamics. 34(2): 145-165pp.

Bommer J. J. and Pinho R. (2006) "*Adapting earthquake actions in Eurocode 8 for performance-based seismic design*". Earthquake Engineering & Structural Dynamics. 35(1): 39-55pp.

Borzi B., Calvi G. M. et al. (2001) "*Inelastic spectra for displacement-based seismic design*". Soil Dynamics and Earthquake Engineering. 21(1): 47-61pp.

Bosiljkov V., Page A., Bokan-Bosiljkov V. and Žarnić R. (2003) "*Performance Based Studies of In-plane Loaded Unreinforced Masonry Walls*". Masonry International. 16(2): 39-82pp.

Bosiljkov V., Tomaževič M. and Lutman M. (2004) "*Optimization of shape of masonry units and technology of construction for earthquake resistant masonry buildings*". Tech. Rep., Slovenian National Building and Civil Engineering Institute, Ljubljana.

Calderini C. and Lagomarsino S. (2008) "*Continuum Model for In-Plane Anisotropic Inelastic Behavior of Masonry*". ASCE (Journal of Structural Engineering). 134(2)pp.

Calvi G. M. and Kingsley G. R. (1996) "*Displacement-based seismic design of multi-degree-of-freedom bridge structures*". International Journal of Rock Mechanics and Mining Sciences & Geomechanics Abstracts. 33(1): 38A-38App.

Calvi G. M. and Sullivan T. J. (2009a) "*Development of a Model Code for Direct Displacement Based Seismic Design*". Tech. Rep., Atti di Linea IV, progetto RELUIS, Napoli, Italy.

Calvi G. M. and Sullivan T. J. (2009b) "*A Model Code for the Displacement-Based Seismic Design of Structures*". IUSS Press: Pavia, Italy.

CEA. (1990) "*Visual Cast3M - Guide d' utilisation*". pp, France.

Chaimoon K. and Attard M. M. (2007) "*Modeling of unreinforced masonry walls under shear and compression*". Engineering Structures. 29(9): 2056-2068pp.

Chopra A. K. and Goel R. K. (2001) "*Direct Displacement-Based Design: Use of Inelastic Design Spectra Versus Elastic Design Spectra*". Earthquake Spectra. 17(1): 47-65pp.

CIMNE. (2011). Available at: http://gid.cimne.upc.es/index.html.

Circolare 2/02/2009 n. 617 C.S.LL.PP. (2009) "*Instrucions for Application of DM 14/01/2008 - Technical Standards for Constructions*". Infrastructure Ministry, Official Gazette of the Italian Republic, February, 2 2009.

Costa C. (2004) "*Implementation of the damage model in tension and compression with plasticity in Cast3m*". Laboratório ELSA, JRC.

Costa C. (2011) "*Análise numérica e experimental do comportamento estrutural de pontes em arco de alvenaria de pedra*". PhD Thesis. Faculdade de Engenharia da Universidade do Porto. Porto. In Portuguese.

da Porto F., Garbin E., Modena C. and Valluzzi M. R. (2005) "*Failure modes for in plane loaded masonry walls made with thin layer mortar*". Proceedings of the 10th Canadian Masonry Symposium. Banff, Alberta, June 8 - 12, 2005. Vol. CD-Rom.

da Porto F., Grendene M. and Modena C. (2009) "*Estimation of load reduction factors for clay masonry walls*". Earthquake Engineering & Structural Dynamics. 38(10): 1155-1174pp.

da Porto F., Grendene M., Mosele F. and Modena C. (2008) "*In-plane cyclic testing and dynamic modelling of reinforced masonry walls*". Proceedings of the 14th World Conference on Earthquake Engineering, International Association for Earthquake Engineering. Beijing, China, October 12-17, 2008. DVD Edition.

da Porto F., Guidi G., Garbin E. and Modena C. (2010a) "*In-Plane Behavior of Clay Masonry Walls: Experimental Testing and Finite-Element Modeling*". Journal of Structural Engineering. 136(11): 1379-1392pp.

da Porto F., Mosele F. and Modena C. (2010b) "*Compressive behaviour of a new reinforced masonry system*". Materials and Structures: 1-17pp.

da Porto F., Mosele F. and Modena C. (2011) "*In-plane cyclic behaviour of a new reinforced masonry system: Experimental results*". Engineering Structures. 33(9): 2584-2596pp.

de Borst R. (2002) "*Fracture in quasi-brittle materials: a review of continuum damage-based approaches*". Engineering Fracture Mechanics. 69(2): 95-112pp.

DISWall. European Community, 2005-2007, COOP-CT-2005-18120. (2008) "*Developing innovative systems for reinforced masonry walls*". Scientific coordinator: C. Modena. University of Padova, http://diswall.dic.unipd.it/.

DM 14/01/2008. (2008) "*Technical Standards for Constructions*". Infrastructure Ministry, Official Gazette of the Italian Republic, February, 4 2008.

Drysdale R. G. and Hamid A. A. (2008) "*Masonry Structures Behavior and Design - 3rd edition*". The Masonry Society: Boulder, Colorado.

Dwairi H. M., Kowalsky M. J. and Nau J. M. (2007) "*Equivalent Damping in Support of Direct Displacement-Based Design*". Journal of Earthquake Engineering. 11(4): 512 - 530pp.

EN 1996-1-1. (2005) "*Eurocode 6: Design of masonry structures - Part 1-1: General rules for reinforced and unreinforced masonry structures*". European Committee for Standardization, Brussels, Belgium.

EN 1998-1. (2004) "*Eurocode 8: Design of Structures for Earthquake Resistance, Part 1: General Rules, Seismic Actions and Rules for Buildings*". European Committee for Standardization, Brussels, Belgium.

Faccioli E., Paolucci R. and Rey J. (2004) "*Displacement Spectra for Long Periods*". Earthquake Spectra. 20(2): 347-376pp.

Fajfar P. (2000) "*A Nonlinear Analysis Method for Performance Based Seismic Design*". Earthquake Spectra. 16(3): 573-592pp.

Faria R., Oliver J. and Cervera M. (1998) "*A strain-based plastic viscous-damage model for massive concrete structures*". International Journal of Solids and Structures. 35(14): 1533-1558pp.

Freeman S. A. (1998) "*The Capacity Spectrum Method as a Tool for Seismic Design*". Proceedings of the 11th European Conference on Earthquake Engineering. Paris, Sept. 6-11.

Gambarotta L. and Lagomarsino S. (1997a) "*Damage model for the seismic response of brick masonry shear walls. Part I: the mortar joint model and its applications*". Earthquake Engineering & Structural Dynamics. 26(4): 423-439pp.

Gambarotta L. and Lagomarsino S. (1997b) "*Damage model for the seismic response of brick masonry shear walls. Part II: the continuum model and its applications*". Earthquake Engineering & Structural Dynamics. 26(4): 441-462pp.

Ganz H. and Thürlimann B. (1984) "*Test on masonry walls under normal and shear loading*". Tech. Rep., Report No. 7502-4, Inst. Of Struct. Engrg., ETH Zurich, Zurich, Switzerland.

Giambanco G., Rizzo S. and Spallino R. (2001) "*Numerical analysis of masonry structures via interface models*". Computer Methods in Applied Mechanics and Engineering. 190(49-50): 6493-6511pp.

Guidi G. (2011) "*Displacement Capacity of Load-Bearing Masonry as a Basis for Seismic Design*". Ph. D. Thesis. University of Trento. Trento, April, 2011. English.

Guidi G. and da Porto F. (2011) "*Development of a fiber model for load-bearing masonry walls*". Proceedings of the ANIDIS 2011 - XIV Convegno di Ingegneria Sismica, Organized by: ANIDIS “Associazione Nazionale di Ingegneria Sismica” and Politecnico di Bari. Bari, Italy, 18-22 September 2011. Vol CD-Rom. 10pp.

Gulkan P. and Sozen M. A. (1974) "*Inelastic response of reinforced concrete structures to earthquake motions*". ACI Journal. Vol. 71(No.12): 604-610pp.

Hamid A. A. and Drysdale R. G. (1980) "*Concrete Masonry Under Combined Shear and Compression Along the Mortar Joints*". ACI Journal. 77(5): 314-320pp.

Hamid A. A. and Drysdale R. G. (1981) "*Proposed Failure Criteria for Concrete Block Masonry under Biaxial Stresses*". Journal of the Structural Division, ASCE. 107(8): 1675-1687pp.

Hegermeir G. A., Nunn R. O. and Arya S. K. (1978) "*Behaviour of concrete masonry under biaxial stresses*". Proceedings of the North American Masonry Conference, University of Colorado. Boulder, USA. 1.1-1.28.

Iwan W. D. and Gates N. C. (1979) "*The effective period and damping of a class of hysteretic structures*". Earthquake Engineering & Structural Dynamics. 7(3): 199-211pp.

Jacobsen L. S. (1930) "*Steady forced vibrations as influenced by damping* ". ASME Transactione. 52(1): 169-181pp.

Kamil Tanrikulu A., Mengi Y. and McNiven H. D. (1992) "*The non-linear response of unreinforced masonry buildings to earthquake excitations*". Earthquake Engineering & Structural Dynamics. 21(11): 965-985pp.

Kowalsky M. J., Priestley M. J. N. and MacRae G. A. (1995) "*Displacement-based design of RC bridge columns in seismic regions*". Earthquake Engineering & Structural Dynamics. 24(12): 1623-1643pp.

Kwan W. and Billington S. (2003) "*Influence of Hysteretic Behavior on Equivalent Period and Damping of Structural Systems*". J. Struct. Eng. 129(5): 576pp.

Lotfi H. R. and Shing P. B. (1994) "*Interface Model Applied to Fracture of Masonry Structures*". ASCE (Journal of Structural Engineering). 120(1): 63pp.

Lourenço P. B. B. (1996) "*Computational strategies for masonry structures*". PhD-Thesis. Delft University of Technology. Delft, 1996. English.

Lourenço P. B. B., De Borst R. and Rots J. G. (1997) "*A plane stress softening plasticity model for orthotropic materials*". International Journal for Numerical Methods in Engineering. 40(21): 4033-4057pp.

Lourenço P. B. B., Milani G., Tralli A. and Zucchini A. (2007) "*Analysis of masonry structures: review of and recent trends in homogenization techniques*". Canadian Journal of Civil Engineering. 34(11): 1443-1457(15)pp.

Lourenço P. B. B. and Rots J. G. (1997) "*Multisurface Interface Model for Analysis of Masonry Structures*". Journal of Engineering Mechanics. 123(7): 660-668pp.

Magenes G. (2006) "*Masonry building design in seismic areas: Recent experiences and prospects from a European standpoint - Keynote 9*". Proceedings of the First European Conference on Earthquake Engineering and Seismology. Geneva, Switzerland, 3-8 September 2006. CD-Rom.

Magenes G. (2010) "*Earthquake resistant design of masonry structures: rules, backgrounds, latest findings*". Proceedings of the 8th International Masonry

Conference, Organized by: International Masonry Society and Technische Universitat Dresden. Dresden, Germany, 4-7 July 2010. Vol. CD-Rom. 29-45.

Magenes G., Baietta S. and Calvi G. M. (1997) "*Una ricerca numerico-sperimentale sulla risposta sismica di edifici in muratura armata*". Proceedings of the ANIDIS 1997 - VIII Convegno Nazionale di Ingegneria Sismica Taormina.

Magenes G., Calvi G. and Gaia F. (1996) "*Shear tests on Reinforced Masonry Walls.*". Tech. Rep. Report RS-03/96, Report RS-03/96. Department of Structural Engineering, University of Pavia, Pavia.

Magenes G. and Calvi G. M. (1997) "*In-plane seismic response of brick masonry walls*". Earthquake Engineering & Structural Dynamics. 26(11): 1091-1112pp.

Mazzon N. (2010) "*Infuence of Grout Injection on the Dynamic Behaviour of Stone Masonry Buildings*". PhD Thesis. University of Padova.

Medhekar M. S. and Kennedy D. J. L. (2000) "*Displacement-based seismic design of buildings-theory*". Engineering Structures. 22(3): 201-209pp.

Miranda E. and Ruiz-García J. (2002) "*Evaluation of approximate methods to estimate maximum inelastic displacement demands*". Earthquake Engineering & Structural Dynamics. 31(3): 539-560pp.

Modena C. (1982) "*On the evaluation of seismic design actions for loadbearing masonry buidings*". Proceedings of the 6th International Brick Masonry Conference ANDIL. Rome.

Modena C. (1992) "*Seismic Behaviour of Masonry Structures: Experimentally Based Modelling*". Masonry International. 6(2): 57 - 68pp.

Modena C. and Barel S. (1987) "*Studies on the Seismic Response of Masonry Wall Construction*". Proceedings of the Pacific Conference on Earthquake Engineering. New Zealand, 5-8 August. 2.

Moehle J. P. (1992) "*Displacement-based design of RC structures subjected to earthquakes*". Earthquake Spectra. 8(3): 403-428pp.

Mosele F. (2009) "*In-Plane And Out-Of-Plane Cyclic Behaviour of Reinforced Masonry Walls*". PhD Thesis. University of Trento, March, 2009. English.

Mosele F., da Porto F., dalla Benetta M. and Modena C. (2008) "*Experimental behaviour of newly developed systems for load bearing reinforced masonry walls*". Proceedings of the 14th IBMaC. Sydney, Australia, February 17-20, 2008. Vol. CD-Rom.

Nicolini L. (2008) "*Sperimentazione e modellazione del comportamento ciclico nel piano di muratura armata per la definizione di fattori di riduzione delle forze*". Graduation Thesis. Dept of Structural and Trasportation Engineering, Padova, April 2008.

Page A. W. (1978) "*Finite element model for masonry*". J. Struct. Eng. 104(8): 1267-1285pp.

Page A. W. (1980) "*A biaxial failure criterion for brick masonry in the tension-tension range*". Int. J. Masonry Constr. 1(1): 20-29pp.

Page A. W. (1981) "*The biaxial compressive strength of brick masonry*". Proc. Inst. Civ. Eng. Pt. 2 71,(Sept), 893, 1981pp.

Page A. W. (1982) "*An experimental investigation of the biaxial strength of brick masonry*". Proceedings of the 6th IBMAC. Rome, Italy. 3-15.

Page A. W. (1983) "*The strength of brick masonry under biaxial compression-tension*". Int. J. Masonry Constr. 3(1): 26-31pp.

Panagiotakos T. B. and Fardis M. N. (2001) "*A displacement-based seismic design procedure for RC buildings and comparison with EC8*". Earthquake Engineering & Structural Dynamics. 30(10): 1439-1462pp.

Paolucci R., Rovelli A. et al. (2008) "*On the reliability of long-period response spectral ordinates from digital accelerograms*". Earthquake Engineering & Structural Dynamics. 37(5): 697-710pp.

Park Y. J., Reinhorn A. M. and Kunnath S. K. (1987) "*IDARC: inelastic damage analysis of reinforced concrete frame - shear-wall structures*". Tech. Rep. NCEER-87-0008, Res. N. C. f. E. E., Buffalo, N.Y.

Paulay T. and Priestley M. J. N. (1992) "*Seismic Design of Reinforced Concrete and Masonry Buildings*". John Wiley & Sons, Inc.

Pegon P. and Anthoine A. (1997) "*Numerical strategies for solving continuum damage problems with softening: Application to the homogenization of Masonry*". Computers & Structures. 64(1-4): 623-642pp.

Priestley M. J. N. (1993) "*Myths and Fallacies in Earthquake Engineering – Conflicts Between Design and Reality*". Tech. Rep., Bulletin of NZ National Society for Earthquake Engineering, New Zealand.

Priestley M. J. N. (2000) "*Performance Based Seismic Design*". Proceedings of the 12th WCEE. Auckland, New Zealand, January, 2000.

Priestley M. J. N., Calvi G. M. and Kowalsky M. J. (2007) "*Displacement Based Seismic Design of Structures*": Pavia, Italy.

Priestley M. J. N. and Grant D. N. (2005) "*Viscous Damping in Seismic Design and Analysis*". Journal of Earthquake Engineering. 9(sup2): 229-255pp.

Priestley M. J. N. and Kowalsky M. J. (2000) "*Direct Displacement-Based Design of Concrete Buildings*". Bullettin of the New Zealand National Society for Earthquake Engineering. 33(4): 421-444pp.

Quelhas da Silva B. L. (2012) "*Diagnosis and Strengthening of Historical Masonry Structures: Numerical and Experimental Analysis*". PhD Thesis. University of Brescia, (under evaluation).

Rosenblueth E. and Herrera I. (1964) "*On a Kind of Hysteretic Damping*". ASCE Journal of Engineering Mechanics. 90(4): 37-48pp.

Rots J. G. (1997) "*Structural masonry an experimental/numerical basis for practical design rules*". Balkema: Rotterdam, The Netherlands.

Samarasinghe W. and Hendry A. W. (1980) "*The strength of brickwork under biaxial tensile and compressive stress*". Proceedings of the International Symposium on Load-Bearing Brickwork. London, UK. 129-139.

Shibata A. and Sozen M. A. (1976) "*Substitute Structure Method for Seismic Design in Reinforced Concrete*". Journal of the Structural Division, ASCE. Vol. 102(No. ST1)pp.

Shing P. B., Schuller M. and Hoskered V. S. (1990) "*Strength and ductility of reinforced masonry shear walls*". ASCE (Journal of Structural Engineering). 116(3): 619-640pp.

Sullivan T. J., Calvi G. M., Priestley M. J. N. and Kowalsky M. J. (2003) "*The limitations and performances of different displacement based design methods*". Journal of Earthquake Engineering. 7(2003): 201pp.

Tassios T. P. (1988) "*Meccanica delle murature*". Liguori Editore: Napoli.

Tomaževič M. (1978) "*The computer program POR*". Tech. Rep., Report of ZRMK., Ljiubliana, Slovenia.

Tomaževič M. (1999) "*Earthquake-resistant design of masonry buildings*". Imperial college press London.

Tomaževič M. (2000) "*Some aspects of experimental testing of seismic behavior of masonry walls and models of masonry buildings*". ISET, Journal of Earthquake Technology. 37(4): 101-117pp.

Tomaževič M. and Apih V. (1993) "*The strengthening of stone-masonry walls by injecting the masonry-friendly grouts*". European Earthquake Engineering. 6(1): 10-20pp.

Tomaževič M. and Lutman M. (1996) "*Seismic Behavior of Masonry Walls: Modeling of Hysteretic Rules*". Journal of Structural Engineering. 122(9): 1048-1054pp.

Tomaževič M., Lutman M. and Bosiljkov V. (2006) "*Robustness of hollow clay masonry units and seismic behaviour of masonry walls*". Construction and Building Materials. 20(10): 1028-1039pp.

Tomaževič M., Lutman M. and Petcovič L. (1996) "*Seismic Behavior of Masonry Walls: Experimental Simulation*". ASCE (Journal of Structural Engineering). vol. 122(n.9): 1040-1047pp.

Tomaževič M. and Velechovsky T. (1992) "*Some aspects of testing small-scale masonry building models on simple earthquake simulators*". Earthquake Engineering & Structural Dynamics. 21(11): 945-963pp.

Toumbakari E. E. and van Gemert D. (1997) "*Lime pozzolana cement injection grouts for the repair and strengthening of three leaf masonry structures*". Proceedings of the 4th International conference on the conservation of monuments in the Mediterranean Basin. Rodhes, Greece. 385–394.

Turnšek V. and Čačovič F. (1971) "*Some experimental results on the strength of brick masonry walls*". Proceedings of the 2nd International Brick Masonry Conference, Stoke on Trent, British Ceramic Research Association. London, UK. pp.149-156.

Valluzzi M., da Porto F. and Modena C. (2004) "*Behavior and modeling of strengthened three-leaf stone masonry walls*". Materials and Structures. 37(3): 184-192pp.

van Zijl G. P. A. G. (2004) "*Modeling Masonry Shear-Compression: Role of Dilatancy Highlighted*". Journal of Engineering Mechanics. 130(11): 1289-1296pp.

Vintzileou E. and Miltiadou-Fezans A. (2008) "*Mechanical properties of three-leaf stone masonry grouted with ternary or hydraulic lime-based grouts*". Engineering Structures. 30(8): 2265-2276pp.

Wakabayashi M. and Nakamura T. (1984) "*Reinforcing principle and seismic resistance of brick masonry walls*". Proceedings of the 8th World Conference on Earthquake Engineering (WCEE). San Francisco, US, 21-28 July 1984. pp. 661–668.